

**UNIVERSITÄT
BAYREUTH**

Lehrstuhl für Kristallographie

Superstructures of magnetic materials

Von der Universität Bayreuth
zur Erlangung des akademischen Grades eines
Doktors der Naturwissenschaften (Dr. rer. nat.)
genehmigte Abhandlung

vorgelegt von
Alexander Wölfel
aus Bayreuth

1. Gutachter: Prof. dr. Sander van Smaalen
2. Gutachter: Prof. Dr. Hans Braun

Tag der Einreichung: 31. Januar 2013
Tag des Kolloquiums: 21. Oktober 2013

Für Veronika

Danksagung

Ich bedanke mich ganz herzlich bei allen derzeitigen und einstigen Mitarbeitern des Lehrstuhls für Kristallographie für die freundliche Unterstützung und das angenehme und freundschaftliche Arbeitsklima.

Mein besonderer Dank gilt Herrn Prof. dr. Sander van Smaalen für die Möglichkeit, am Lehrstuhl für Kristallographie an dieser Dissertation gearbeitet und an anderen spannenden Projekten mitgewirkt haben zu dürfen. Sein Ideenreichtum und seine fortwährende Begleitung haben diese Arbeit entscheidend geprägt.

Weiterhin möchte ich Prof. Dr. Hans Braun dafür danken, dass er sich als Zweitgutachter dieser Arbeit zur Verfügung gestellt hat.

Besonders bedanken möchte ich mich bei meiner Familie, die mich während der Zeit meiner Promotion stetig motivierte und geduldig unterstützte. Insbesondere bedanke ich mich bei meiner Mutter, der ich eine sorgenfreie Studienzeit zu verdanken habe und die mich auf unzählbar viele Weisen gefördert hat und bei Veronika, ohne die mein Leben so viel ärmer wäre. Ihr Verständnis ermöglichte es mir meine Promotion erfolgreich abzuschließen.

Vielen Dank!

Contents

1	Introduction	1
2	Rare earth intermetallic Carbides RTC_2	5
2.1	Structural properties	5
2.2	Magnetic properties and modulated structures	7
3	Diffraction experiments with point detectors	13
3.1	Measurements with synchrotron radiation	13
3.1.1	Advantages of synchrotron radiation	13
3.1.2	Low temperature requirements	15
3.1.3	Attenuation factors of X-ray filters	18
3.1.4	On the way to low temperatures	20
3.1.5	Techniques for ω - 2θ maps	23
3.1.6	Data collection of a modulated structure	24
3.2	Experiments on a Mach3 diffractometer	25
3.2.1	Examination of the crystal quality	25
3.2.2	Crystal shape optimization by ψ scans	26
3.2.3	Structure determination at room temperature	27
4	Layered perovskite-related compounds $\text{A}_n\text{B}_n\text{O}_{3n+2}$	31
4.1	Crystal chemical and physical properties	31
4.1.1	Layered construction principle	31
4.1.2	Low dimensional properties	32
4.2	Overlooked superstructure reflections	35
5	Diffraction experiments with area detectors	37
5.1	Experiments on a Mar345dtb diffractometer	37
5.2	Integration with EVAL15	40

5.3	Unit cell determination	43
6	Commensurate charge-density wave with frustrated interchain coupling in SmNiC₂	47
6.1	Introduction	47
6.2	Experimental	49
6.3	Discussion	52
6.4	Conclusions	56
7	Anisotropic thermal expansion of La_n(Ti,Fe)_nO_{3n+2} (<i>n</i> = 5 and 6)	57
7.1	Introduction	57
7.2	Experimental	59
7.2.1	Synthesis	59
7.2.2	Single-crystal X-ray diffraction	60
7.2.3	Structure refinements in (3+1)-dimensional superspace	65
7.3	Results and discussion	65
7.3.1	Crystal structures	65
7.3.2	Thermal expansion	70
7.3.3	Octahedral tiltings	72
7.4	Conclusions	76
8	Two-dimensional magnetic clusters in La_n(Ti_{1-x}Fe_x)_nO_{3n+2} (<i>n</i> = 5 with <i>x</i> = 0.2 and <i>n</i> = 6 with <i>x</i> = 0.33)	77
8.1	Introduction	77
8.2	Experimental	78
8.3	Structural features	79
8.4	Discussion	83
8.5	Conclusions	86
9	Summary	87
10	Zusammenfassung	91
A	Appendix SmNiC₂	97
A.1	Step scans to determine the modulation vector	98
A.2	Intensities of main and satellite reflections	99
A.3	Determination of the detector collimator's incidence limit	100

B Appendix $\text{La}_n(\text{Ti}_{1-x}\text{Fe}_x)_n\text{O}_{3n+2}$ $n = 5$ and 6	101
B.1 Structural details of $\text{La}_n(\text{Ti}_{1-x}\text{Fe}_x)_n\text{O}_{3n+2}$ $n = 5$ and 6	102
B.2 Site occupancies of Fe^{3+}	111
B.3 Distortion of $(\text{Ti,Fe})\text{O}_6$ octahedra	115
B.4 Variation of the $(\text{Ti,Fe})\text{-O}$ distances	119
B.5 Bond valence sums	123
Bibliography	127
Publications	137
List of Figures	141
List of Tables	143
Erklärung	145

Chapter 1

Introduction

This thesis reports the solution and analysis of crystalline superstructures of selected magnetic materials and effects of their temperature-dependent changes are presented. The analysis is concentrated on compounds containing a rare earth metal and a transition metal, the latter is responsible for the magnetic properties. The compounds either belong to the group of ternary carbides or they are perovskite-related layered compounds. The investigated solid state materials have been studied by use of single-crystal X-ray diffraction experiments.

Magnetic superstructures can be formed if the compound contains atoms with a magnetic moment. The order and the correlation between the magnetic moments characterize the macroscopic magnetic properties of the compounds. The periodicity of the arrangement of the magnetic moments may differ from the crystallographic periodicity. Many ferromagnetic and antiferromagnetic compounds undergo a phase transition at temperatures well below room temperature from a state without ordered magnetic moments to a state with an ordered arrangement (Blundell, 2001). In these low temperature structures the periodicity of the superstructure can be commensurate or incommensurate with the periodicity of the underlying substructures.

An aim of this thesis was to find explanations for varying magnetic properties, which appear in systems lacking a complete order of the magnetic moments, but show magnetic correlations different from pure paramagnetism and phase-transitions with varying magnetic interactions. Indeed X-ray diffraction experiments cannot detect directly the magnetic moments. But structure refinements based on data from X-ray diffraction experiments are more sensitive than those based on neutron diffraction for small structural distortions accompanying magnetic transitions

(Lovesey and Collins, 1996). Single-crystal X-ray diffraction is a powerful tool to refine the atomic coordinates and site occupancies of all atoms in the crystal structure. From the knowledge of precise atomic coordinates bond lengths and bond angles between the magnetic atoms and their environment are calculated, which are used to identify the path of the magnetic interaction between the magnetic moments. Site occupancies inform about (partial) ordering of magnetic atoms. Temperature-dependent changes in these parameters might be used for understanding the reasons for varying magnetic properties of the compounds. On the other hand a lack of clear temperature-dependent changes of parameters allows an exclusion of those regarding the mechanism of varying magnetic properties.

Many quasi-low-dimensional compounds with magnetic order also show other interesting collective phenomena, as for example a charge-density wave state. Charge-density wave states can appear in compounds with co-planar boundaries of Fermi surfaces, which allow a nesting by a modulation wave vector and result in a lowering of the energy of the electrons. Within the charge-density wave state, the electrical conductivity above the threshold value of the electrical field is non-linear due to an extra contribution to the conduction from a sliding charge-density wave. The superstructure manifests itself through weak additional spots in the diffraction pattern, which are usually incommensurate with respect to the periodic lattice of the basic structure. X-ray diffraction experiments allow the identification of the atoms, that carry the valence band responsible for the charge-density wave (Gruener, 1994).

In chapter 2 a short description is given of the crystal-chemical and structural properties of ternary carbides containing a rare earth metal and a transition metal. The focus of the chapter is on those compounds having a CeNiC_2 -type structure. Many of these compounds show a magnetic ordering at low temperatures and some show in addition a charge-density wave state. Indeed in this thesis only the charge density wave state of SmNiC_2 is examined, but a parallel is drawn between the occurrence of ferromagnetic and antiferromagnetic order in these compounds and the competition of the charge-density wave state with the ferromagnetic ordering in SmNiC_2 at low temperatures. Modifications in the electronic band structure have been suggested to be responsible for the phase transitions and the realized type of magnetic order (Laverock et al., 2009).

Chapter 3 reports on the methodical concepts of the single-crystal X-ray diffraction experiments of SmNiC_2 . The advantages of synchrotron radiation over conventionally generated X-rays as well as the requirements for low-temperature measurements are described. The use of a point-detector requires special treatments

like the determination of attenuation factors of X-ray filters. On the other hand a four-circle diffractometer with a point detector combined with highly monochromatized synchrotron radiation provides the unique possibility for special experimental techniques like ω - 2θ maps for the analysis of peak splittings. Conditions and successful performances are discussed. Moreover, the crystal shape determination as well as the structure solution by use of data from a single-crystal X-ray diffraction experiment, are described.

In chapter 4 a crystal-chemical description of structural properties of the series of perovskite-related layered compounds $A_nB_nO_{3n+2}$ is given. The low dimensional properties, which have been already observed for many compounds of this series, are explained from the layered building principle with slabs of the perovskite-type structure separated from each other by gaps. The diffraction pattern of these compounds consists of weak superlattice reflections next to strong reflections, which describe the periodicities of the underlying undistorted structure (Levin and Bendersky, 1999).

Chapter 5 reports on a series of single-crystal X-ray diffraction experiments of $La_5(Ti_{0.80}Fe_{0.20})_5O_{17}$ and $La_6(Ti_{0.67}Fe_{0.33})_6O_{20}$ on a Mar345dtb image-plate diffractometer and a Huber four-circle-diffractometer in the temperature range 90 - 370 K. The experimental procedures as well as the data integration with the program EVAL15 are described.

Chapter 6 describes the properties of the incommensurately modulated crystal structure of $SmNiC_2$ in the charge-density-wave state at $T = 60$ K above the phase transition to the ferromagnetically ordered state. Temperature-dependent X-ray diffraction was used to establish the orthorhombic lattice symmetry down to 9 K in the ferromagnetic state. Structure refinements indicate that the charge-density wave should be considered as a commensurate charge-density wave centered on chains of Ni atoms, which is rendered incommensurate by frustrated interchain coupling.

Chapter 7 reports about the temperature-dependent structural analysis carried out for the two perovskite-related layered compounds $La_5(Ti_{0.80}Fe_{0.20})_5O_{17}$ and $La_6(Ti_{0.67}Fe_{0.33})_6O_{20}$. Analysis of the B cation valences, partial order of Ti/Fe and of the octahedral distortions, which all were found being almost temperature independent, revealed general dependencies in $A_nB_nO_{3n+2}$ compounds. The thermal expansions of both compounds were determined in the temperature range 90 - 370 K. The thermal expansion is found being anisotropic with the largest expansion perpendicular to the stacking direction. The temperature dependent behavior of the lattice parameters, and the widths of slabs and interslab regions along the stacking direction is discussed in comparison with the effects of hydrostatic pressure to a

perovskite-related compound, which are known from literature (Loa et al., 2004).

In chapter 8 differences in the magnetic properties between the $n = 5$ and 6 compounds of $\text{La}_n(\text{Ti}_{1-x}\text{Fe}_x)_n\text{O}_{3n+2}$ are explained by the formation of two-dimensional, ferromagnetically organized magnetic clusters in the $n = 6$ compound. For the $n = 5$ compound the formation of clusters is prevented by a lower concentration of iron. The crossover of the magnetic behavior of the $n = 6$ compound at about room temperature is a consequence of the parallel arrangement of the magnetic moments in the clusters at temperatures above room temperature and anti-parallel arrangement of the magnetic moments of neighboring clusters below.

Chapter 2

Rare earth intermetallic Carbides RTC_2

2.1 Structural properties

The ternary carbides RTC_2 , with a rare earth metal (R) and a transition metal (T), are known since the synthesis of the first compounds in the 1980s. While several of these compounds have been prepared (compare Table 2 in Jeitschko and Gerss (1986)), crystal structure refinements have been published only for a few compounds (Bodak and Marusin, 1979; Bodak et al., 1980; Jeitschko and Gerss, 1986). Isostructurality of other compounds has been assumed on the basis of a consideration of measured lattice parameters (Semenenko et al., 1983; Jeitschko and Gerss, 1986). Most of these compounds are assumed to crystallize in the orthorhombic $CeNiC_2$ -type structure (Bodak and Marusin, 1979). Some others, mainly those containing cobalt as transition metal, are associated to the related monoclinic lattice of the $CeCoC_2$ -type structure (Jeitschko and Gerss, 1986).

The spacegroup of the $CeNiC_2$ -type structure is $Amm2$ (No. 38, $Z=2$) (Bodak and Marusin, 1979) and these structures can be understood as a stacking along c of layers of R and T atoms, having almost the same z coordinate. Between these layers carbon atoms are arranged as C_2 pairs (Fig. 2.1 (a)). The interatomic C–C distances are $\approx 1.37 \text{ \AA}$ and therefore similar to the distances in graphite (Jeitschko and Gerss, 1986; Semenenko et al., 1983). Fig. 2.1 (b) shows an alternative description of the structure, it consists of trigonal prisms, formed by R atoms and filled alternately by T atoms and C_2 pairs. The absence of inversion symmetry in these compounds is obvious in this description (Subedi and Singh, 2009). The lattice parameters of the

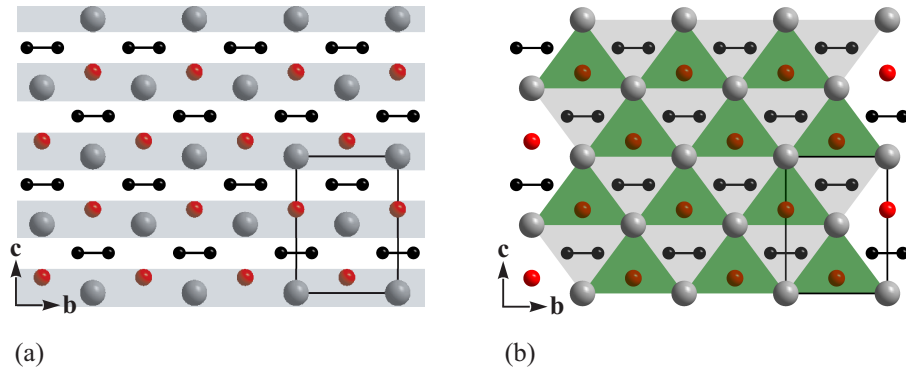


Figure 2.1: Two equivalent descriptions of the $CeNiC_2$ -type crystal structures, R and T atoms are indicated as gray and red spheres, while C_2 groups are drawn as black atom pairs. The unit cell is shown in both representations. (a) Stacked model along c with the layers of R and Ni indicated as gray areas and the C_2 pairs in between. (b) Trigonal prisms of R atoms, indicated as alternating green and gray triangles, and filled with Ni atoms and C_2 pairs, respectively.

$CeNiC_2$ -type compounds are very similar for various compounds (Semenenko et al., 1983; Jeitschko and Gerss, 1986). For $DyNiC_2$ the fractional coordinates and the anisotropic atomic displacement parameters (ADP) are reproduced from Jeitschko and Gerss (1986) as an example in Table 2.1.

Table 2.1: Relative atomic coordinates and atomic displacement parameters of the atoms in $DyNiC_2$ as published by Jeitschko and Gerss (1986). The lattice parameters are $a = 3.5707(6)$, $b = 4.5075(6)$ and $c = 6.0410(9)$ Å. Standard deviations in the least significant digits are given in parentheses. Because of the symmetry of this structure, the values U_{12} and U_{13} are equal to zero for all atomic positions. Equivalent isotropic thermal parameters are computed from the anisotropic values.

Atom	Dy	Ni	C
x	0	0.5	0.5
y	0	0	0.1523(10)
z	0	0.6116(1)	0.3016(6)
U_{11} (Å ²)	0.0024(1)	0.0069(2)	0.0074(12)
U_{22} (Å ²)	0.0062(1)	0.0049(2)	0.0072(12)
U_{33} (Å ²)	0.0040(1)	0.0029(2)	0.0046(9)
U_{23} (Å ²)	0	0	0.0002(9)
U_{iso}^{eq} (Å ²)	0.0042(1)	0.0049(2)	0.0063(11)

The monoclinic CeCoC_2 -type structure may be understood as a distorted version of the closely related orthorhombic CeNiC_2 -type structure. The main difference follows from a tilting of the C_2 pairs in the CeCoC_2 -type structure, which are parallel to \mathbf{b} in the CeNiC_2 -type structure. The arrangement of the atoms in layers is similar to the $R\text{NiC}_2$ compounds. Nevertheless, the differences between both structures are large enough to permit a crossover from one structure type to the other driven by temperature or pressure. All compounds are either monoclinic or orthorhombic, independent of combination of pressure and temperature during crystallization or of the synthesis technique. Within the limits of pressure $10^{-2} - 8 \times 10^9$ Pa and of temperature 1300 – 1900 K a broad variation of the synthesis parameters is possible, without affecting the crystal structures. Therefore, the range of the thermodynamic stability of the RTC_2 compounds is very wide. Only the compound SmCoC_2 is an exception, which crystallizes in monoclinic symmetry in low-temperature synthesis, but it is orthorhombic after annealing at high temperatures (Semenenko et al., 1983). A phase-transition of the high-temperature modification of SmCoC_2 to the low-temperature modification, however, has not been observed in the low-temperature range. Thus the high-temperature modifications of this compound is stable also in the low-temperature range and the same is true for the low-temperature modification vice versa.

2.2 Magnetic properties and modulated structures

At low temperatures several RTC_2 compounds exhibit magnetic order and some of them additionally show a transition to a charge-density wave (CDW) state. In both cases the structures in these states are described either as modulated structures or as superstructures. Best understood are the properties of those compounds containing nickel. In the $R\text{NiC}_2$ compounds magnetic interactions arise from the 4f-electrons of the rare earth metals without any considerable contribution of nickel. This finding results from the analysis of the magnetic properties of YNiC_2 , which has no 4f-electrons and is a Pauli-paramagnet with a very weak temperature-dependence of the magnetic susceptibility (Yakinthos et al., 1990; Onodera et al., 1998). Also LaNiC_2 lacks magnetic order, as a consequence of the missing 4f-electrons. Instead it is a superconductor below $T_C = 2.7$ K (Subedi and Singh, 2009). Studies of the magnetic properties show that the $R\text{NiC}_2$ compounds reveal different kinds of magnetic ordering for various R (Onodera et al., 1998; Kotsanidis et al., 1989). The

realized magnetic properties of the compounds are discussed in the literature as the result of a different magnitude of the changes of the crystalline electric field with varying R and structural transformations (Koshikawa et al., 1997; Onodera et al., 1998).

Most $RNiC_2$ compounds exhibit antiferromagnetic (AFM) order with Neel temperatures (T_N) below 30 K (Koshikawa et al., 1997; Onodera et al., 1998). The orientation of the magnetic moments varies with the increasing number of the 4f-electrons in the period. Some compounds, e.g. with $R = Er, Tm$ or Nd , show an alignment parallel to \mathbf{a} . Resulting magnetic lattices are identical to the nuclear lattices (Yakinthos et al., 1990; 1991) or, for example in the case of Nd , fourfold magnetic superstructures, having doubled a and b axes, occur (Yakinthos et al., 1990). Others have more complex non-collinear arrangements of the magnetic moments of the \mathbf{R} atoms. In these cases propagation vectors are commensurate or incommensurate with the crystal lattices. $HoNiC_2$, as an example, undergoes on cooling an order-order transition at $T_t = 2.9$ K from an incommensurate and sinusoidal moment modulated structure with $\mathbf{q}_{incom} = (0.5, 0.33, 0.86)$ to a structure with commensurate modulation and a propagation vector $\mathbf{q}_{com} = (0, 0, 1)$ (Koshikawa et al., 1997). A magnetic non-ordered exception is $PrNiC_2$, which properties differ from those of its neighbors in the periodic table of elements. No phase-transition down to 2 K has been observed and therefore it is interpreted as a van-Vleck paramagnet.

$SmNiC_2$ is of particular interest, because it is the only known $RNiC_2$ compound, which shows ferromagnetic (FM) order at low temperature and a CDW state. In $SmNiC_2$ the magnetic moments of the Sm atoms are aligned parallel to the crystallographic \mathbf{a} axis. Onodera et al. (1998) explained it in the strong uniaxial anisotropy of the magnetic properties, which forces this alignment of the magnetic moments. They also showed that the temperature dependence of the magnetic susceptibility indicates a first order phase transition at T_C , that seems to be closely correlated with the ferromagnetic order and is in difference to all other $RNiC_2$ compounds. An overview of the magnetic properties of the known $RNiC_2$ compounds is given in Table 2.2.

An ordered low energy CDW state arises from electron-lattice interactions in (quasi-)low-dimensional systems (Grüner, 1988). In consequence of the interplay between the electron-lattice and the magnetic interaction of the 4f-electrons of the rare earth metals some interesting physical phenomena can arise. One example is the large magnetoresistance (Shimomura et al., 2009). An essential property of a CDW is a periodic distortion of the lattice, because the energetic advantage of the

Table 2.2: Magnetic properties and properties of measured or theoretically proposed CDW states of of $R\text{NiC}_2$ compounds. Compounds with R different from those listed here are not yet synthesized or the magnetic and CDW properties are not analyzed. T_C , T_N , T_t and T_{CDW} denote the Curie, Neel, order-order and CDW transition temperatures, respectively.

R	magnetic properties	reference
Y	non-magnetic	Hase and Yanagisawa (2009)
La	non-magnetic, but superconducting, $T_C = 2.7$ K	Subedi and Singh (2009)
Ce	AFM, magnetic moments parallel \mathbf{a} , $T_N = 20$ K, $\mathbf{q}_m = (0.5, 0.5, 0)$	Onodera et al. (1998)
Pr	van-Vleck paramagnet, no transition down to 2 K	Onodera et al. (1998)
Nd	AFM, magnetic moments parallel \mathbf{a} , $T_N = 7$ K, $\mathbf{q}_m = (0.5, 0.5, 0)$, theo. CDW, $\mathbf{q}_{CDW} = (0.5, 0.55, 0)$	Onodera et al. (1998), Laverock et al. (2009)
Sm	FM, magnetic moments parallel \mathbf{a} , $T_C = 17.5$ K, CDW, $\mathbf{q}_{CDW} = (0.5, 0.516, 0)$, $T_{CDW} = 148$ K,	Onodera et al. (1998), Shimomura et al. (2009)
Gd	AFM, mag. moments non-collinear, $T_N = 20$ K, $\mathbf{q}_m = (0.5, 0.5, 0)$, theo. CDW, $\mathbf{q}_{CDW} = (0.5, 0.57, 0)$	Matsuo et al. (1996), Laverock et al. (2009)
Tb	AFM, mag. moments non-collinear, $T_N = 27$ K, $\mathbf{q}_m = (0.5, 0.5, 0)$	Onodera et al. (1994)
Dy	AFM, mag. moments non-collinear, $T_N = 10$ K, $\mathbf{q}_1 = (0, 0, 1)$ below $T_t = 4.2$ K, $\mathbf{q}_2 = (0.47, 0.36, 0.935)$ above T_t	Yakinthos et al. (1994)
Ho	AFM, mag. moments non-collinear, $T_N = 4$ K, $\mathbf{q}_1 = (0, 0, 1)$ below $T_t = 2.9$ K, $\mathbf{q}_2 = (0.5, 0.33, 0.86)$ above T_t	Koshikawa et al. (1997)
Er	AFM, magnetic moments parallel \mathbf{a} , $T_N = 8.5$ K, $\mathbf{q}_m = (0, 0, 1)$	Koshikawa et al. (1997)
Tm	AFM, magnetic moments parallel \mathbf{a} , $T_N = 5.5$ K , $\mathbf{q}_m = (0, 0, 1)$	Koshikawa et al. (1997)
Th	non-magnetic	Hase and Yanagisawa (2009)

valence electrons is realized through the modulation of the positions of the atoms, which are participating in the low-dimensional-valence band. This modulation in the density of the electronic charge can be commensurate or incommensurate with the periodicity of the atomic positions.

Murase et al. (2004) explained anomalous temperature dependence of the electrical resistivity and lattice parameters of some $RNiC_2$ compounds in a CDW transition. For some of the $RNiC_2$ compounds a CDW state either has been experimentally proven (Shimomura et al., 2009) or is assumed on basis of theoretical band structure calculations (Laverock et al., 2009). In the case of $SmNiC_2$ the formation of the CDW state at $T_{CDW}=148$ K and its destruction at $T_C=17.5$ K have been reported by Shimomura et al. (2009) on the basis of data from X-ray scattering and electrical resistivity measurement. The CDW state is verified by the existence of satellite reflections at incommensurate positions in X-ray diffraction experiments as well as by X-ray diffuse scattering experiments (Shimomura et al., 2009). The modulation wave vector is given by $\mathbf{q}_{CDW} = (0.5, \sigma_2, 0)$ and the value of $\sigma_2 = 0.516$ was determined at $T = 60$ K by so-called \mathbf{q} -scans along \mathbf{b}^* (Appendix A). At the same temperature a successful structure refinement applied superspace group $Amm2(\frac{1}{2} \sigma_2 0)000$ with lattice parameters $a = 3.6965$ (5), $b = 4.5293$ (7) and $c = 6.0955$ (8) Å (Chapter 6). In $SmNiC_2$ nickel atoms, which are dimerized along \mathbf{a} in the CDW state, carry the quasi-one-dimensional (1D) valence band, responsible for the CDW. Therefore, the direction of the CDW is also along \mathbf{a} . As a consequence of a geometrical frustration between neighboring layers of Ni atoms the modulation is incommensurate with the lattice periodicity and described by the modulation vector $\mathbf{q} = (0.5, 0.516, 0)$ (Chapter 6).

The first order phase transition to the FM ordered state is accompanied with the destruction of the CDW state. This is indicated by the sudden disappearance of the satellite reflections and a sharp decrease of the resistivity (Shimomura et al., 2009; Murase et al., 2004). The FM character is revealed by a sharp increase of the magnetic susceptibility χ_{mag} from about 5×10^{-5} to about 7×10^{-3} emu g $^{-1}$ (Onodera et al., 1998). A phase transition from the CDW to the FM state has not been observed in any other compound and gives therefore the unique opportunity to study the reasons for the crossover and the structural changes, which maybe provides the mechanism for it. Furthermore, differences to other $RNiC_2$ compounds can be studied, which do not show ferromagnetic order or a CDW state. The arising of the FM ordering in $SmNiC_2$ at T_C and the accompanied lattice distortions lead to a modification of the electronic band structure, which affects the nesting conditions

of the Fermi surface, and thus destroys the CDW state in SmNiC_2 (Laverock et al., 2009). It is explained, that other CDW compounds show a similar deformation of the Fermi surfaces at the transition temperature to the AFM state, thereby destroying the CDW (Laverock et al., 2009).

For the compounds with $R = \text{Nd, Gd and Tb}$ the phase transitions to an AFM state is indicated by a distinct change in the temperature dependence of the resistivity (Onodera et al., 1998; Matsuo et al., 1996; Onodera et al., 1994). Theoretical band structure calculations using the scalar relativistic linear muffin-tin orbital method by Laverock et al. (2009) demonstrate the possibility of a CDW state in the Sm, Nd and Gd compounds and reveal the conditions for the existence of a CDW state. Differences in the contours of the Fermi surfaces and therefore different nesting conditions with varying R atoms are the reason for the existence of CDW states in only a few $R\text{NiC}_2$ compounds. An overview of known or proposed CDW compounds is included in Table 2.2.

Chapter 3

Diffraction experiments with point detectors

3.1 Measurements with synchrotron radiation

3.1.1 Advantages of synchrotron radiation

Synchrotron light sources (synchrotrons) are important instruments for structure analysis experiments. They are used next to conventional sealed tube or rotating-anodes X-ray radiation sources. Synchrotrons are a special type of particle accelerator storage rings, in which charged particles circulate at relativistic velocities. They are combined with photon experiment beamlines, utilizing the synchrotron radiation. The spectral range of synchrotron radiation goes from infrared to hard X-ray radiation. The radiation is emitted in forward direction tangential to the orbital trajectory of the charge carriers with a narrow divergence in the perpendicular direction (Mills, 2002).

The main advantages of synchrotron radiation over conventional X-rays for single-crystal X-ray diffraction experiments follow from their properties. Synchrotrons produce highly parallel and very narrow beams of highly intense X-rays (Willmott, 2011). Moreover, the use of monochromator crystals, allows an adjustment of the wavelength to the experimental requirements. This freedom allows to satisfy two requirements of a successful structure determination. The first one is the demand of a low X-ray absorption of the crystal. The linear absorption coefficients of the components of the compound under investigation individually define the strength and the wavelength dependence of the absorption. But for all compounds a short

wavelength reduces the absorption. Therefore, this fact suggests the use of a wavelength as short as possible. On the other hand a short wavelength reduces the spatial resolution between individual reflections. As it follows from the Bragg equation, the difference in the scattering angles of two neighboring reflections is inversely proportional to the wavelength. Especially for those modulated structures, having satellite reflections close to main reflections, a small wavelength enhances the risk of an overlap between reflections. This renders the successful determination of intensities of weak satellite reflections difficult. The tunability allows for the selection of a wavelength small enough to avoid strong absorption, but large enough to separate all reflections. Such an adjustment is not attainable by conventional X-ray sources.

Flux, brilliance and emittance of the beam are the most important measures for the quality of synchrotron radiation. While the first one is defined as the number of photons per second per unit bandwidth going through a defined area, the brilliance defines how the flux is distributed over the source area and in the angular range. The brilliance of modern synchrotrons is about 10^{21} photons/(s mrad² mm² 0.1% bandwidth) and thus of the order of about ten magnitudes larger than of a conventional X-ray radiation source (Mills, 2002). The intensities of strong satellite reflections, are in general less than a few thousandths of the intensities of main reflections¹ (van Smaalen, 2007). It is in principle possible to increase the intensity ratio of reflection to background by the rise of the exposure time, a common procedure for conventional X-ray sources, but in practice mostly not possible, because the maximum time for experiments is limited. Hence only a X-ray source of high brilliance allows the determination of both main and satellite reflections within a reasonable time. Successful studies of modulated compounds are therefore limited to synchrotron light sources.

The brilliance is inversely proportional both to the angular range, which is defined by the divergence of the beam and the source size (Willmott, 2011). The product of the divergence and the source size is called emittance and therefore it is the aim to obtain as low an emittance as possible. In current synchrotrons very low values are reached, with emittances $\epsilon_x < 3$ pm rad and $\epsilon_y < 7$ pm rad perpendicular to the beam (Willmott, 2011). For the low divergence of synchrotron radiation the full width at half maximum (FWHM) of Bragg reflections of a single crystal of good quality is a few hundredths of a degree, while it is about one tenth for X-rays from conventional sources (Wendschuh-Josties and Wulf, 1989).

¹An example is given for one pair of main and satellite reflections in Appendix A.

3.1.2 Low temperature requirements

For measurements far below room temperature, e.g. in the CDW and FM state of SmNiC_2 , a cooling system for the crystalline sample is needed, which provides a constant temperature. Crystal temperatures below ≈ 80 K can only be reached by use of helium cryostats. In general two different functional principles can be distinguished, open-flow and closed-cycle cryostats.

In the first technique a helium gas stream blows permanently over the crystal and controls its temperature. The gas is generated by the evaporation of liquid helium from a storage vessel. The lowest stable temperature, which can be reached is about 14 K for commercial available cryostats (e.g. Oxford Diffraction, Helijet; Cryo Industries of America, Cryocool-G2-LT). It is limited by the boiling point of helium, which is $T = 4.22$ K at ambient pressure and the increase of the crystal temperature by contact with the environment. Higher temperatures are realized by electrical heating of the gas. The highest possible temperature for this kind of cryostat is about 500 K. The biggest disadvantage of this kind of cryostat is the continuous loss of helium and the high costs of the cryogen.

For the measurements of SmNiC_2 a helium closed-cycle cryostat DE-202 G (APD Cryogenics Inc.) was used (Fig. 3.1 (a)). It works pneumatically driven in accordance with the Gifford-McMahon process (Ekin, 2006). The Gifford-McMahon refrigeration cycle starts with the opening of the high pressure path, allowing the high pressure helium gas to pass from the compressor into the expansion chamber. Second, the pressure differential drives the displacer "up" allowing the gas at the bottom of the chamber to expand. Third the low pressure path to the compressor is opened, allowing the gas to flow back and removing the heat from the system. Finally, the pressure differential returns the displacer to its original position completing the cycle. The name closed cycle follows from the fact, that the same helium gas is used again and the whole procedure can be repeated for theoretically an infinite number of cycles. The DE-202 G cryostat uses two stages to reach low temperatures of ≈ 4.5 K (Fig. 3.1 (b)).

The application of this method requires a mounting of the crystal in a way, which ensures a good thermal conduction between the crystal and the displacer. For that purpose carbon fibers (diameter of each fiber about 0.01 mm) are pasted together to a bundle of diameter of about 0.1 mm applying a glue, which is stable at low temperatures. The bundle is glued with conductive silver to a small pin, made of oxygen-free copper, and cut under an oblique angle to a needle shape of about 3 mm

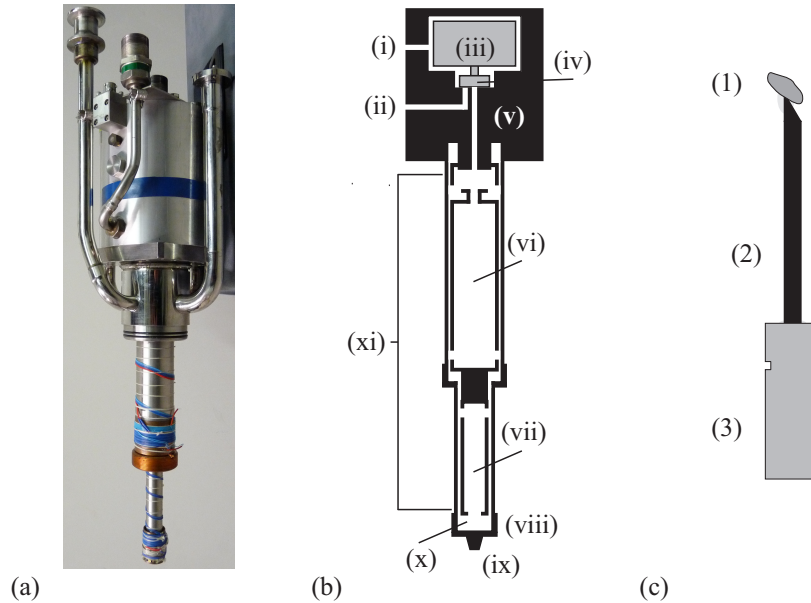


Figure 3.1: (a) Closed-cycle cryostat DE-202 G (APD Cryogenics Inc.) without beryllium domes and schematic drawing of (b) the helium closed-cycle cryostat and (c) the crystal preparation. Parts of the cryostat: (i) high pressure gas inlet, (ii) low pressure gas outlet, (iii) valve motor, (iv) rotating valve, (v) body of the cryostat, (vi) first stage refrigerator, (vii) second stage refrigerator, (viii) electrical heater, (ix) adapter for crystal mounting, (x) cold chamber and (xi) displacer. The crystal (1) is glued to the bundle of carbon fibers (2), which is mounted in the copper pin (3). The pin is fixed with conductive silver to the adapter.

length above the pin. On the sharp top of the needle the crystal is mounted by use of a small amount of two-component glue (Fig. 3.1 (c)).

The pin is screwed by use of an adapter to the bottom of the second stage. This connection path is made of oxygen-free copper and has a high thermal conductivity. Therefore, the crystal is almost at the same low temperature as the cold chamber of the second stage. Higher temperatures are reached by use of an electrical heating, which is attached near the crystal. Thus it is possible to adjust the sample temperature up to 325 K. Contacts with ambient air would heat the sample and lead to the formation of ice around the crystal. Therefore, two beryllium domes are used to generate a vacuum shield, preventing the contact with air. The inner

dome is in thermal contact with the first stage and therefore at low temperature of $\approx 80\text{ K}$, to reduce the heating of the crystal by thermal radiation. The outer dome is at room temperature and thermally isolated from the cold parts. The evacuated area between the domes ensures the thermal isolation. In addition the area within the inner dome is evacuated, preventing thermal contact between the comparative warmer inner dome and the crystal.

Some disadvantages arise from the use of a closed-cycle cryostat with beryllium domes. During the lowering of the temperature the crystal moves out of the center of the primary beam, caused by the shrinking of mostly the copper rod on the second stage, but also of the adapter, pin and carbon bundle. The domes prevent the visual observation of the crystal. Therefore, it is not possible to recenter the crystal optically at low temperatures. Only a combination of the calculation of the necessary height correction and knowledge from previous experiments, combined with incremental optimizations of the crystal position, inspection by the help of the primary beam camera and intensity measurements of the reflections allows to readjust the position of the sample.

As another hindrance the beryllium domes create powder diffraction rings. At positions, where these rings coincide with Bragg-reflections of the sample, the measured intensities are falsified. This disturbance of the beryllium domes can be reduced by the application of a detector collimator. It is a pipe of about 30 cm length, which can be mounted in front of the detector to prevent the detection of X-rays diffracted at positions other than the crystal position. It works for scattering angles 2θ larger than $\approx 13^\circ$ (Appendix A). Using the detector collimator requires an exact alignment, pointing from the detector in the direction of the intersecting point of the diffractometer axes. Otherwise no intensities would be measured, although a reflection fulfill the diffraction condition. The best position to inspect and correct the adjustment is the detector positioned at $2\theta = 0^\circ$, then the detector collimator has to lay in one line with the primary beam collimator. This coincidence can be optically inspected and small deviations can be corrected.

The largest restriction of the application of this cryostat arises from the limitations in the movement of the diffractometer axes. It is caused by the body of the cryostat, which is about 30 cm in height, the electric cables connecting it with the controller and the helium hoses connecting it with the compressor. The first limits the freedom of rotation of the crystal about the ω - and the χ -axes in combination with the movement of the detector about the 2θ -axis. Restricting limits have to be set, to avoid collisions between the body of the cryostat and the detector or other

parts of the diffractometer. The latter restrictions limit the freedom of rotation of the diffractometer about the ϕ -axis to 180° in both directions from the zero position. Larger rotations would twist the cables and hoses. As a result the helium stream from or to the compressor would be reduced or stopped and the cable and hoses could be damaged. Even in the best case, nothing would be damaged, but the temperature would not be stable anymore. For the measurement of SmNiC_2 all limitations of the movements together reduced the reachable reflections to those, laying in not much more than one octant of the reciprocal space. This limitation reduces the redundancy of the measured data and may hampers the solution of more complicated crystal structures.

3.1.3 Attenuation factors of X-ray filters

The first steps of a measurement with the helium closed-cycle cryostat and the NaI(Tl)-scintillation counter at beamline D3 of HASYLAB at DESY (Hamburg) are the adapting of variable parameters, like wavelength, beamsize and filters, to the experiment. For the measurement of SmNiC_2 the wavelength was set to 0.5600 \AA . This wavelength is near the K_α wavelength of conventional silver X-ray radiation and therefore the tabulated structure factors for this wavelength could be used in the structure refinement. For SmNiC_2 the beam was chosen to a size of $0.5 \times 0.5 \text{ mm}^2$ and shaped as a square. This quite large beamsize reduces the risk, that the crystal moves out of the beam, when it is not visible anymore within the beryllium domes. Moreover, the weighty cryostat body is attached in the seating at the Euler cradle by a screw thread and only partially balanced by a counterweight. Therefore, the forces during the sudden start and stop of the movements of the diffractometer lead to displacements of the crystal by a few hundredths of a millimeter. Thus a relatively large beamsize also ensures, that the crystal moves not (partially) out of the beam as a consequence of these displacements.

The dynamic range of the detector limits the maximum counting rate, that can be measured without computational corrections for accurate reflection intensities. During the measurement of SmNiC_2 a point-detector was used with an upper limit of about 30000 cps in the linear range. At a higher rate the deadtime of the scintillation counter, which is the minimum time interval of a possible detection of two separate photons, leads to a non-linear relationship between the observed counting rate and the true X-ray photon rate. At much higher rates the detector has an extended deadtime and an increase in the X-ray photon rate causes a decrease of the counting

rate (Jenkins et al., 1995). In ω scans of strong reflections the saturation range is visible in drops of the counting rates near the maximum (Fig. 3.2 (a)).

Corrections for the deadtime easily result in wrong intensities. Instead it is better to avoid deadtime losses by use of beam filters, which weaken the primary X-ray beam after the monochromator. As a result of a properly chosen filter a reflection profile shows no drop anymore (Fig. 3.2 (b)). At D3 three different filters are implemented in the filter box. Combinations of them can be inserted into the X-ray beam. The real photon rates can be calculated from the counting rates and the attenuation factors of the filters. As a consequence of the wide range of useable wavelengths and the broad range of performed experiments, different filter materials and thicknesses of filter foils are available at the beamline. Because of the wavelength dependence of the absorption and small differences in the adjustment of the filters, the determination of the current values of the attenuation factors is recommended at the begin of each measurement cycle. The attenuation factors give the ratio of unfiltered and filtered intensities.

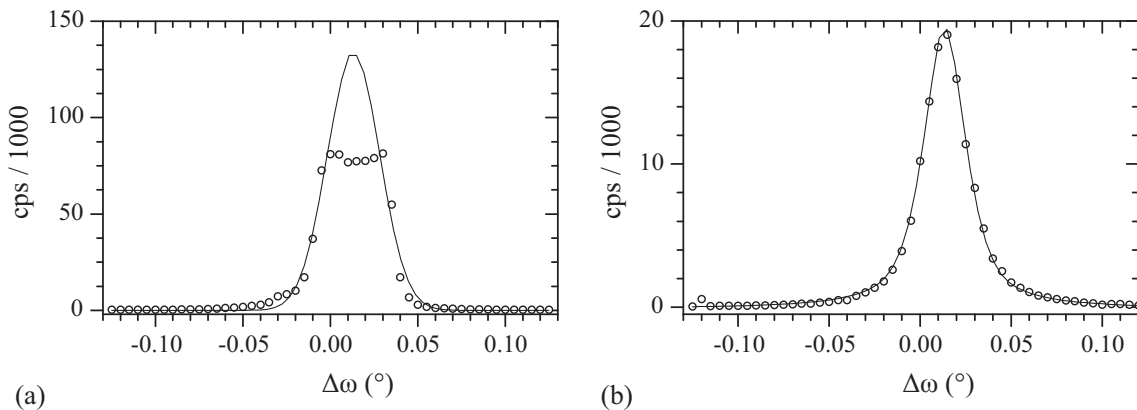


Figure 3.2: Effects of deadtime losses in ω scans of a reflection. Measured without a filter (a) and with a combination of filters F_1 and F_2 (resulting attenuation factor $f_{12} = 7.952$) (b). Visible is the drop of the counting rate near the maximum, where an increasing photon rates leads to a decreasing counting rate, and the correction for this effect by use of primary beam filters. The lines are fits of Pseudo-Voigt functions to the data as guidelines for the eyes.

The attenuation factors are determined from a series of measurements of the observed counting rates without and with filters. A test crystal or a sample crystal of high quality can be used and a strong reflection (preferable about 100000 cps) needs to be centered. The counting rate is repeatedly measured (about five to ten

times) without any filter (F_0) and with each of the three filters (F_i , $i = 1, 2, 3$). From the ratios of the average values \bar{F}_0 and \bar{F}_i the attenuation factors f_i can be calculated as $f_i = \frac{\bar{F}_0}{\bar{F}_i}$. An example for SmNiC_2 is given in Table 3.1.

In addition the control software of the diffractometer allows an automatic determination of the attenuation factors of the three filters and as a by-product the deadtime of the scintillation counter. For this purpose the rocking curve of a centered reflection is walked down in steps of $\Delta\omega = 0.001^\circ$. Between the steps the intensity is slightly decreasing and at each step the counting rates are measured five times for one second, first without filters, then with each of the three filters at a time. From the mean values the attenuation factors are calculated in a extrapolation towards zero intensity. The deadtime is obtained from the slope of the least square line of the measured points. At the end of the procedure the values can be transferred into the parameter file of the diffractometer software. An example for this procedure is given in Table 3.2 for SmNiC_2 .

3.1.4 On the way to low temperatures

The actual measurement of a compound at low temperature starts already at room temperature. A sample crystal of very high quality has to be selected. The quality of a crystal can be determined from the FWHM of the reflection profiles in so-called ω scans. At the synchrotron the FWHM is almost entirely defined by the mosaicity of the single-crystal, while the FWHM by use of conventional X-ray sources is additionally broadened by the divergence of the beam. Therefore a crystal seems to be good, with a FWHM equal to the instrumental limit of $\approx 0.1^\circ$, measured at laboratory. But it is maybe not a perfect crystal at the synchrotron and shows splitted reflection profiles or much broader FWHM than the possible $\approx 0.02^\circ$ of an optimal crystal.

Also the crystal preparation decides, whether a crystal can be used for the experiment or not. If the crystal preparation prevent the reach of sufficiently many reflections, even a crystal of highest quality is not suitable. It is similar in case that a series of reflections, which is required for a special measurement, can not be reached. An example are the reflections of the $\omega - 2\theta$ -maps of SmNiC_2 (Chapter 6).

With a centered almost perfect crystal the beryllium domes can be mounted carefully on the cryostat. After several hours of evacuating, the sample can be cooled to low temperature. The cooling rate should not be too large to avoid damage to the crystal. The orientation of the crystal at low temperature can be either restored

Table 3.1: Counting rates measured for ten seconds for SmNiC₂, without (F_0) and with the three different filters (F_i). Because the relative variation in the counting rates increases with the increasing attenuation of the filters, the rates for F_1 , F_2 and F_3 were more often measured than F_0 . The result of this measurement are attenuation factors $f_1 = 1.999$, $f_2 = 3.978$ and $f_3 = 16.165$.

No.	Counting rate for filters			
	F_0	F_1	F_2	F_3
1:	76634	38344	19343	4719
2:	77334	38325	19308	4637
3:	76189	38560	19355	4751
4:	-	38223	19203	4890
5:	-	38354	19066	4794
6:	-	38413	19316	4809
7:	-	-	19241	4765
8:	-	-	19441	4766
9:	-	-	19281	4770
10:	-	-	-	4781
11:	-	-	-	4678
12:	-	-	-	4759
13:	-	-	-	4740
14:	-	-	-	4744
15:	-	-	-	4715
16:	-	-	-	4668
17:	-	-	-	4725
18:	-	-	-	4794
19:	-	-	-	4744
20:	-	-	-	4709
21:	-	-	-	4719
22:	-	-	-	4768
23:	-	-	-	4713
average	76719	38370	19284	4746

Table 3.2: Automatic procedure for the determination of the attenuation factors. Counting rates at 17 steps on the rocking curve are measured for five times one second for SmNiC_2 , without (F_0) and with the three different filters (F_i). The extrapolated factors are $f_1 = 2.034$, $f_2 = 4.114$ and $f_3 = 16.502$ and an average deadtime of 2.787 μs .

No.	Average counting rate for filters				Attenuation factors		
	\bar{F}_0	\bar{F}_1	\bar{F}_2	\bar{F}_3	f_1	f_2	f_3
1:	64764	34804	18312	4656	1.861	3.537	13.909
2:	83896	46707	24979	6435	1.796	3.359	13.037
3:	104483	60500	32841	8540	1.727	3.182	12.234
4:	115351	68756	37692	9886	1.678	3.060	11.669
5:	117527	70073	38207	9995	1.677	3.076	11.759
6:	109735	64265	34842	9192	1.708	3.149	11.938
7:	94292	53717	28574	7390	1.755	3.300	12.760
8:	80992	44957	23716	6156	1.802	3.415	13.157
9:	71435	39224	20491	5265	1.821	3.486	13.569
10:	63202	34220	17664	4549	1.847	3.578	13.894
11:	56244	29990	15614	3976	1.875	3.602	14.147
12:	52185	27956	14241	3620	1.867	3.664	14.415
13:	49246	26151	13474	3423	1.883	3.655	14.387
14:	45751	23922	12350	3141	1.913	3.704	14.564
15:	43054	22466	11408	2876	1.916	3.774	14.968
16:	40466	21247	10835	2738	1.905	3.735	14.780
17:	38228	20210	10182	2570	1.892	3.755	14.873
Extrapolated attenuation factors					2.034	4.114	16.502
Extrapolated Deadtime / μs					2.870	2.847	2.645
Average deadtime / μs					2.787		

by the analysis of a rotation photo, or by the stepwise change of the temperature and the iterative adaption of the orientation matrix. The first variant necessitates a further rotation photo analysis at the final temperature, which interpretation is hampered by the appearance of powder rings of the beryllium domes, which overlap with Bragg-reflections of the crystal. Therefore, maybe not enough reflections for the determination of the crystal orientation can be found. The second method costs more time, which is limited at the synchrotron and the shrinking of the cold finger requests the gradually change of the crystal height. Thus the crystal can move out of the beam after some adaptations, as the result of small errors in each of the steps. To readjust the crystal to the center of the beam is almost impossible. For SmNiC_2 the temperature was directly lowered to 60 K and the orientation of the crystal could be found from a rotation photo analysis.

3.1.5 Techniques for ω - 2θ maps

The transition to a low temperature state can be accompanied by a structural distortion, which results in a lowering of the lattice symmetry, as it was observed for example in the transition-metal oxyhalides VOCl and CrOCl (Schönleber et al., 2009; Angelkort et al., 2009). A lower symmetry results in a splitting of reflections, which are on the face diagonals of the reciprocal lattice planes. A lattice distortion can be weak, with a small derivation of the angles from 90° only, which is maybe not visible in ordinary ω scans. Therefore, so-called ω - 2θ scans are performed for each of the reflections. They give the diffracted intensities as a function of the crystal orientation (ω) and the scattering angle (2θ)s.

For SmNiC_2 , with reciprocal axes length $a^* = 0.27053$, $b^* = 0.22078$ and $c^* = 0.16405 \text{ \AA}^{-1}$, a monoclinic lattice distortion with monoclinic angles α , β or γ would have been indicated by splittings of the reflections $(0\ 2\ \bar{2})$, $(2\ 0\ \bar{4})$ or $(2\ \bar{2}\ 0)$. These reflections fulfilled also the condition of being reachable within the limits of movement and having strong intensities. For the maps each reflection has to be centered with detector slits set to $4 \times 4 \text{ mm}^2$. No automatic procedure is available and a series of ω scans at slightly different 2θ values has to be performed individually. The difference in 2θ between the scans defines the stepsize along the direction of the scattering angle. Therefore it needs to be similar to the acceptance angle of the diffracted beam in 2θ . Best results can be obtained with detector slits set to $6.00 \times 0.02 \text{ mm}^2$, this corresponds to an acceptance angle of 0.0031° in 2θ . Each ω scan has to be done with a stepsize, small enough to resolve fine details, and a number

of steps, which allows the complete reflection profile to be displayed. In dependence of the crystal quality this is fulfilled by a stepsize of 0.002 to 0.004° and about 80 to 120 steps. After all scans of a reflection are finished the measured intensities from all scans have to be combined in one file. These data are used to create the ω - 2θ map of this reflection. The ω - 2θ maps of SmNiC₂, which were generated in accordance to the procedure described here, are shown in chapter 6. Only the combination of synchrotron radiation with the use of a four-circle diffractometer attached with a point detector allows the creation of ω - 2θ maps.

3.1.6 Data collection of a modulated structure

The solution of a modulated structure requires the measurement of integrated intensities of main and satellite reflections by ω scans. This procedure is called data collection. Requirements for a successful data collection are a sufficiently accurate matrix, describing the crystal orientation, and information about the optimum scan width, stepsize, time per step and aperture of the detector. For satellite reflections the exact modulation vector should be found or checked by so-called **q**-scans (Appendix A.1).

A data collection with the NaI(Tl)-scintillation counter enables the separate measurement of the intensities of all reflections. This is a big advantage over area detectors, especially for modulated structures, because satellite and main reflections can be measured with an individual measuring time per step. The disadvantage is the long duration in total, which limits the maximum number of reflections to be measured. As a consequence the method is only suitable for compounds having a small unit cell volume ($V \lesssim 300 \text{ \AA}^3$). It is a good practice to measure the reflections in shells of $\frac{\sin \theta}{\lambda}$ with similar number of reflections in each of it. In case of technical problems it is maybe not possible to finish the whole measurement, but at least the inner shells would be completed by adapting this procedure. An example for the used shells of SmNiC₂ and the number of satellite and main reflections measured in the shells is given in Table 3.3.

Table 3.3: Shells in $\frac{\sin\theta}{\lambda}$ with the numbers of main and first order satellite reflections measured for SmNiC₂.

Shell	$\frac{\sin\theta}{\lambda}$ limits (\AA^{-1})		No. of reflections		
	min	max	main	sat.	all
1:	0	0.41	38	81	119
2:	0.41	0.53	50	105	155
3:	0.53	0.63	67	117	184
4:	0.63	0.70	54	122	176
5:	0.70	0.74	44	66	110
reflections in total:			253	491	744

3.2 Experiments on a Mach3 diffractometer

3.2.1 Examination of the crystal quality

Additional experiments, necessary for a successful analysis of the structure of SmNiC₂, were carried out using a Nonius Mach3 diffractometer (Fig 3.3). This is a four-circle diffractometer designed in κ -geometry. The conventional X-ray radiation used for the experiments is generated by a rotating anode, which is operated at a generating power of 4.1 kW with an accelerating voltage of 55 kV and an electron current of 75 mA. The diffracted radiation is detected by a scintillation counter.

This diffractometer is used for preliminary tests of the crystal quality, for the determination of the crystal shape and for a collection of intensities for the structure refinement at room temperature. The quality of the crystal is inspected by performing ω scans of strong reflections, which are distributed over the three reciprocal lattice directions of the crystal. The shape of the peak profiles and the FWHM of the reflections determine the quality. The occurrence of peak splitting directly leads to a discarding of the sample. Also crystal, which shows peak widths distinctly larger than the lowest experimentally reachable value of about 0.1° , are not suitable for synchrotron experiments. In the ω scans the crystal is continuously rotated over an angle of $\Delta\omega = 1$ or 2° . The peak widths are calculated from fits of Gaussian or Pseudo-Voigt functions to the measured data.

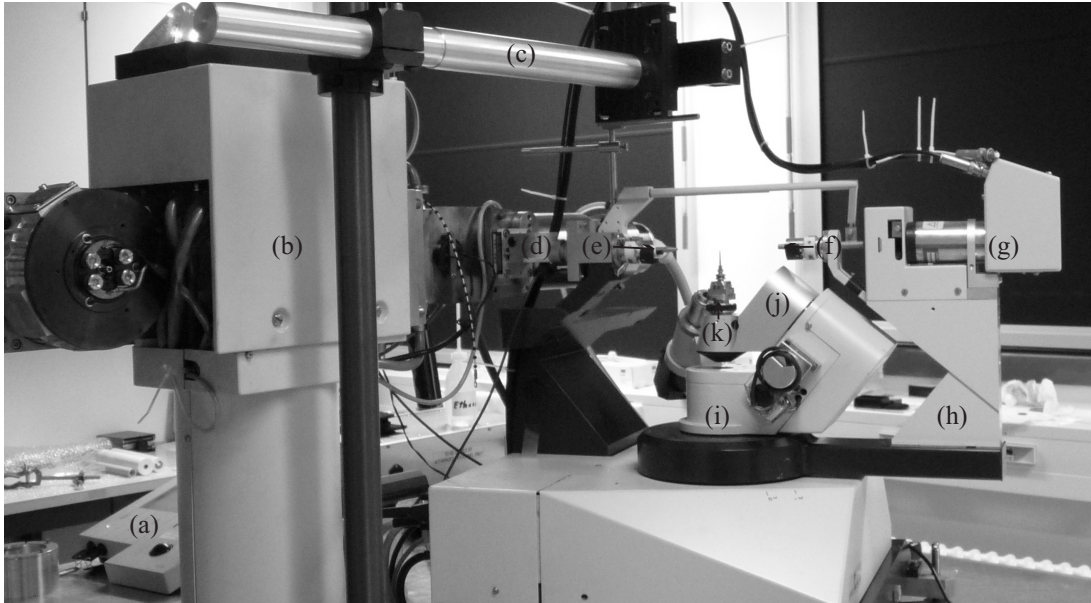


Figure 3.3: Setup of the Nonius Mach3 four-circle diffractometer with κ geometry and attached scintillation counter (installed at the Laboratory of Crystallography, University of Bayreuth). (a) Control panel of (b) rotating anode, (c) rack for the cooling system (not installed on the picture) (d) monochromator, (e) primary beam collimator, (f) detector collimator, (g) scintillation counter on the (h) 2θ arm, (i) ω block, (j) κ block, on which the (k) ϕ axis with goniometer head and crystal is mounted.

3.2.2 Crystal shape optimization by ψ scans

The effect of absorption of X-ray radiation by the diffracting sample attenuates the measured intensities in dependence of the beam path through the crystal. A correct structure description therefore necessitates a correction of this effect by the knowledge of the crystal shape. One way to determine the crystal shape is the measurement of ψ scans of selected reflections. Each reflection is measured repeatedly in varying orientations, differing in a rotation about the scattering vector. The angle of this rotation is the ψ angle (Fig. 3.4 (a)). In each scan the intensities of the reflections are determined in so-called parallel mode, when the detector and the crystal are simultaneously rotated about 2θ and ω , such that the condition $\omega = \frac{2\theta}{2}$ holds at any time. Best results can be reached with increments of 10° between the scan.

The program HABITUS (Herrendorf, 1993) is used to create a model for the crystal shape employing ψ dependence of the reflection intensities. In a semi-empirical optimization the program calculates the difference of the crystal shape from a sphere.

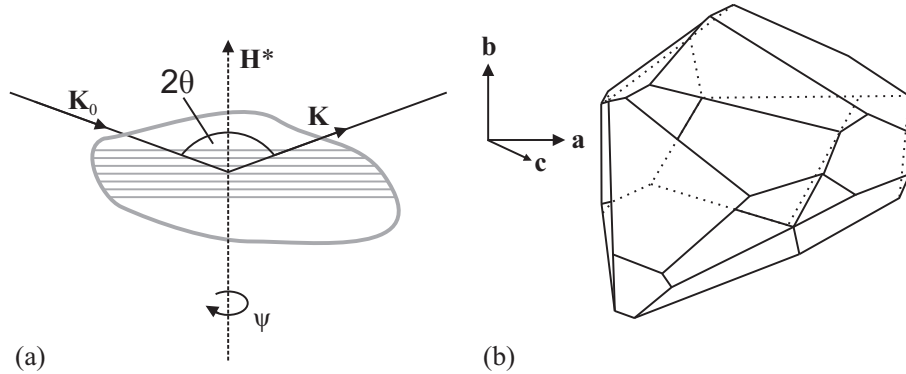


Figure 3.4: ψ Scan. Crystal rotation about the ψ axis (a) and refined crystal shape for SmNiC_2 (b).

As a consequence of the non-isotropic crystal shape the lengths of the beam path through the crystal are different for varying ψ angles and the amount of absorbed intensity depends on the length of the path. Therefore, the resulting intensities are different in each step of the rotation. Beginning from a starting model, e.g. an icosahedron, the program varies the distances to the center, the size and the tilting of the crystal faces, to equalize all values of the absorption corrected intensities. The refined shape of the model can be different from the shape of the real crystal, because additional absorptions, e.g. from the glue or the bundle of carbon fibers, are included in the shape of the model. But the rough shape and the dimensions should be the same for the model and the sample. The refined crystal shape the model for the used crystal of SmNiC_2 is shown in Fig. 3.4 (b). For SmNiC_2 the calculated faces and their distances to the center were used to correct the intensities for absorption effects with JANA2006.

3.2.3 Structure determination at room temperature

The non-modulated structure of SmNiC_2 at room temperature is not yet published, although it was expected to be isostructural to the other RNiC_2 compounds (Chapter 2.1). Therefore, the Mach3 diffractometer was used to measure the intensities of the reflections for a refinement of this structure. The intensities of 3299 reflections were measured applying the parallel mode in eleven shells up to $(\frac{\sin \theta}{\lambda})_{max} = 1.25 \text{ \AA}^{-1}$. The refinement using JANA2006 confirmed the CeNiC_2 -type structure and converged smoothly towards a good fit to the diffraction data with satisfying $R(\text{obs/all}) = 2.07/2.07$. Details of the data collection and refinement

procedure are given in Table 3.4. The structural parameters at room temperature are shown in Table 3.5. The free-refined values of the relative coordinates are very similar to the the literature values of DyNiC₂ from Jeitschko and Gerss (1986) – compare to Table 2.1.

Table 3.4: Structure of SmNiC₂ at room temperature. Details of the crystal, data collection and refinement procedure are given.

<i>Crystal data</i>	
Chemical formula	SmNiC ₂
Space group	<i>Amm</i> 2
<i>a</i> (Å)	3.7037 (3)
<i>b</i> (Å)	4.5279 (2)
<i>c</i> (Å)	6.0947 (4)
<i>V</i> (Å ³)	102.21 (1)
<i>Z</i>	2
Crystal size (mm ³)	0.12 × 0.06 × 0.004
<i>Data collection</i>	
Transmission T_{\min}/T_{\max}	0.092/0.299
No. of measured, unique and observed reflections ($I > 3\sigma(I)$)	3299, 961 961
R_{int}	0.042
<i>h</i>	0 → 9
<i>k</i>	0 → 11
<i>l</i>	−15 → 15
θ_{max} (°)	63
$(\frac{\sin(\theta)}{\lambda})_{\text{max}}$ (Å ^{−1})	1.254
<i>Refinement</i>	
<i>R</i> (obs/all)	0.021/0.027
<i>wR</i> (obs/all)	0.047/0.047
<i>S</i> (obs/all)	2.38/2.38
No. of parameters	15
$\Delta\rho_{\min}/\Delta\rho_{\max}$ (e Å ^{−3})	−1.48/0.7

Table 3.5: Relative atomic coordinates and atomic displacement parameters of the atoms of SmNiC₂ at room temperature. Standard deviations in the least significant digits are given in parentheses. Because of the symmetry of this structure, the values U_{12} and U_{13} are equal zero for all atomic positions. The last row lists equivalent isotropic thermal parameters computed from the anisotropic values.

Atom	Sm	Ni	C
x	0	0.5	0.5
y	0	0	0.1509 (7)
z	0	0.6125 (1)	0.3019 (5)
U_{11} (Å ²)	0.00418 (5)	0.00804 (17)	0.01323 (92)
U_{22} (Å ²)	0.00538 (4)	0.00412 (13)	0.00500 (66)
U_{33} (Å ²)	0.00519 (4)	0.00466 (12)	0.00738 (68)
U_{23} (Å ²)	0	0	0.0002 (9)
U_{iso}^{eq} (Å ²)	0.00491 (3)	0.00560 (8)	0.00753 (44)

Chapter 4

Layered perovskite-related compounds $A_nB_nO_{3n+2}$

4.1 Crystal chemical and physical properties

4.1.1 Layered construction principle

$Ca_2Nb_2O_7$ was the first compound, which was described as a layered perovskite-related structure of the series $A_nB_nO_{3n+2}$ (Brandon and Megaw, 1970). Initially, Rowland et al. (1958) had determined that $Ca_2Nb_2O_7$ gives X-ray powder diffraction that is different from that of cubic pyrochlore-type structures of compounds of identical stoichiometry e.g. $Cd_2Nb_2O_7$ (Jona et al., 1955)). From single-crystal diffraction data they found a monoclinic lattice and suggested the non-centrosymmetric space group $P2_1$. This space group is now confirmed as correct. In subsequent studies, also orthorhombic symmetry and centrosymmetric space groups were incorrectly assigned to compounds of the $A_nB_nO_{3n+2}$ series (Section 4.2). A series of comprehensive studies was performed by Nanot et al. (1974; 1976; 1979; 1981; 1986) and Ishizawa et al. (1975; 1976; 1980; 1981; 1982) on niobate and titanate compounds of this structure type. These investigations created the basis for the understanding of the structure and the physical properties of the series $A_nB_nO_{3n+2}$. In the decades following these studies several additional compounds were synthesized and analyzed. An overview of currently known compounds is given in two articles by Lichtenberg et al. (2001; 2008).

The basic crystal structure is described as slabs of the perovskite structure type ABO_3 separated from each other by gaps. The borders on both sides of the gaps

are formed by layers of oxygen. These oxygen atoms are not shared by octahedra of the next slab, which leads to one extra layer of oxygen for each slab with respect to ideal perovskite structure. Each slab is n BO_6 octahedra wide along the stacking direction. Therefore, the width of the slabs increases with n , which determines the structure type. Cations A occupy the voids between the octahedra. Compounds with integer n are known for n ranging from 2 to 7. In addition compounds with non-integral n represent structures with alternate arrangements of slabs of different width. $\text{Ce}_{4.33}\text{Ti}_{4.33}\text{O}_{15}$, for example, consists of the sequence of two slabs of width $n = 4$ and one slab of width $n = 5$. Thus the average number of octahedra is given by $n = 4.33$ (Lichtenberg et al., 2001). Along the stacking axis, the \mathbf{b} axis in this thesis, the octahedra are connected zig-zag like, while they form chains along the \mathbf{a} axis (Fig. 4.1). Neighboring slabs are shifted with respect to each other along \mathbf{a} by one half of an octahedral body diagonal. The stoichiometry of this series is alternatively written as ABO_x with the oxygen content $x = 3 + \frac{2}{n}$.

Existing at high temperatures (Cava and Roth, 1981; Ishizawa et al., 1982) or as hypothetical high-symmetry structures (Levin and Bendersky, 1999) the compounds possess orthorhombic structures with untilted octahedra. The space groups of these structures are either Cmcm for $n = \text{even}$ or Immm for $n = \text{odd}$. Unit cell parameters can be expressed in terms of $a_c \approx 3.9 \text{ \AA}$, the unit cell parameter of the cubic perovskite, as $a_o = a_c$, $b_o = (n + 1)\sqrt{2}a_c$ and $c_o = \sqrt{2}a_c$. The extent of the interslab region, the distance between the slabs, is approximately equal to the length of an edge (O–O distance) of an octahedron ($\approx \frac{1}{\sqrt{2}}a_c$).

Tilting of the octahedra leads to a lowering of both point and translational symmetry (Levin et al., 1998). The structures at room temperature or below are therefore either incommensurately modulated (Daniels et al., 2002) or have a monoclinic symmetry (Guevarra et al., 2005a;b). The fourfold monoclinic superlattices of the latter are obtained from the orthorhombic unit cells as $\mathbf{a}_m = 2\mathbf{a}_o$, $\mathbf{b}_m = -\mathbf{a}_o + \mathbf{b}_o$ and $\mathbf{c}_m = \mathbf{c}_o$. The space groups of the real structures were established as $\text{P}2_1$ (c unique) for $n = \text{even}$ (Scheunemann and Müller-Buschbaum, 1975; Guevarra et al., 2005b) and $\text{P}2_1/\text{b}$ (c unique) for $n = \text{odd}$ (Daniels et al., 2003; Guevarra et al., 2005a).

4.1.2 Low dimensional properties

The oxide materials of the series of layered perovskite-related compound $A_nB_nO_{3n+2}$ show a large variety of interesting electrical and magnetic properties. For example in

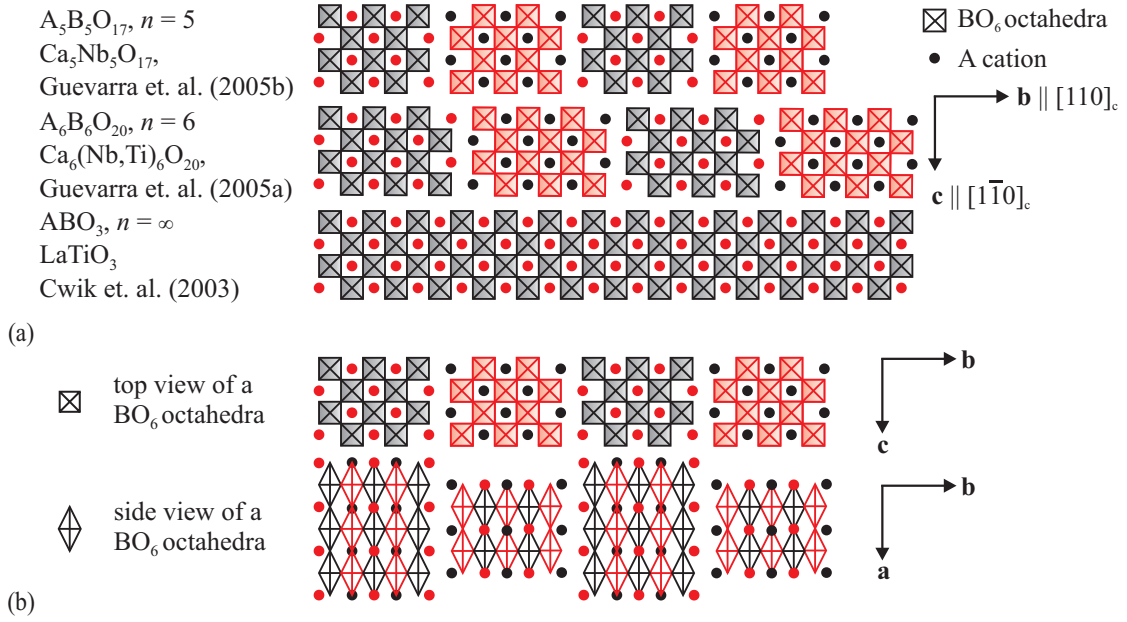


Figure 4.1: Idealized, non-distorted perovskite-related structures. (a) Crystal structures of the $n = 5, 6$ and ∞ members of the series $A_n B_n O_{3n+2}$ in the projection along **a**. For each structure the general formula and an example with reference is given. (b) Schematic projection of the zig-zag and chain like connections of the octahedra along **b** and **a**, respectively. The black and red colors indicate the differences in height along the direction of the projections.

the strontium niobates the electric character changes completely by a slight change of the oxygen content. While $Sr_2Nb_2O_7$ ($n = 4$) is ferroelectric, with one of the highest known ferroelectric transition temperature of $T_C = 1613$ K (Nanamatsu et al., 1975), $Sr_5Nb_5O_{17}$ ($n = 5$) is a quasi-1D metal. It shows highly anisotropic electrical properties with a metallic conductivity along the **a** axis (Kuntscher et al., 2002). This metallic character can be related to the chain-like arrangement of the NbO_6 octahedra along **a** along with a partially filled 3d band on the Nb atoms. As a consequence of the layered structure the resistivity is much larger perpendicular to the chains, because the gaps between the slabs hamper the electrical transport.

The varying electrical properties have been studied by three different experimental methods, namely DC-resistivity measurement, optical spectroscopy in the infrared range and angle-resolved photoemission spectroscopy (Kuntscher et al., 2004). All methods pointed to the same result, that the difference between the

$n = 4$ and 5 members can be found in the existence of a central chain of almost undistorted NbO_6 octahedra in $\text{Sr}_5\text{Nb}_5\text{O}_{17}$. Band structure calculations in the local density approach showed, that a predominant contribution to the density-of-states near the Fermi-energy is attributed to Nb atoms of the least distorted octahedra in the center of the slabs. Nb in octahedra closer to the borders of the slabs contribute significantly less, as these octahedra are more distorted. Such chains of nearly undistorted octahedra lack in $\text{Sr}_2\text{Nb}_2\text{O}_7$. Thus the quite large distortion of all octahedra prevent a metallic behavior in the case of $\text{Sr}_2\text{Nb}_2\text{O}_7$. An alternative explanation can be given by considering the valences of the ions in both compounds. For $\text{Sr}_2\text{Nb}_2\text{O}_7$ charge neutrality is reached with valences Sr^{2+} , Nb^{5+} and O^{2-} and an empty 3d band of the Nb atoms. On the other hand charge neutrality for $\text{Sr}_5\text{Nb}_5\text{O}_{17}$ leads to the same valences Sr^{2+} and O^{2-} , but requires $\text{Nb}^{4.8+}$ in average. Therefore, the 3d band consists of 0.2 electrons/Nb atom, which are responsible for the metallic behavior. Similar differences in the electrical behavior are also found for other niobates and titanates (Kuntscher et al., 2003; 2004; Lichtenberg et al., 2001; 2008).

Similar to the electrical properties the magnetic behavior shows a significant dependence on the crystal structure type. In this series magnetic superstructures can be formed, if the cation sites are occupied by ions having a magnetic moment. For titanates $\text{Ln}^{3+}\text{TiO}_x$ ($\text{Ln} = \text{Cr}, \text{Pr}, \text{Nd}, \text{Sm}$ or Eu) the magnetic properties are exclusively determined by the magnetic moments of the Ln^{3+} ions. In contrast, the magnetic properties of compounds, doped with iron at the B cation sites, are predominated by the iron (Lichtenberg et al., 2008). Examples for a significant change of the magnetic interaction, as a result of a slight variation of the iron content, are the two $\text{La}_n(\text{Ti}_{1-x}\text{Fe}_x)_n\text{O}_{3n+2}$ compounds with $x = 0.20$ for $n = 5$ and $x = 0.33$ for $n = 6$ (Chapter 8). The $n = 5$ compound displays almost an Curie-Weiss behavior without any clear indications for a magnetic ordering. Whereas the magnetic behavior with temperature of the $n = 6$ compound is markedly different from that of the $n = 5$ compound. It shows a strong ferromagnetic interaction at high temperatures with a change to antiferromagnetic interaction at about 280 K (compare figure 8.3). But both compounds remain paramagnetic at all temperatures and no long range order is developed.

The differences in the magnetic correlations are explained in the distinct lower concentration of magnetic Fe^{3+} ions of the $n = 5$ compound compared to the $n = 6$ type. Furthermore, two central layers, occupied predominately by Fe ions create a quasi-2D magnetic lattice in the case of $\text{La}_6(\text{Ti}_{0.67}\text{Fe}_{0.23})_6\text{O}_{20}$. Within the magnetic lattice ferromagnetic correlated clusters of in average $N_C = 51.5$ Fe ions are formed at

low temperature. Within each slab the clusters are linked by only a few inter-cluster connections, therefore their interaction is paramagnetic. Between neighboring slabs the interactions of the clusters are antiferromagnetic and enhanced at least by a factor of N_C . At higher temperatures the ferromagnetic interaction in the slabs dominates over the antiferromagnetic interaction between neighboring slabs and the clusters start to dissolve. Therefore the crossover from a ferromagnetic to an antiferromagnetic coupling appears. For $\text{La}_5(\text{Ti}_{0.77}\text{Fe}_{0.23})_5\text{O}_{17}$ only 1D chains of sites along **a** exist in the centered layers of the slabs, which are highly occupied by iron. Moreover, these chains are interrupted by non-magnetic Ti^{4+} ions and no significant magnetic interaction appears (Chapter 8).

A generalization of these results indicates the possibility of a magnetic superstructure with long range order in the $n = 7$ compound with the nominal composition $\text{La}_7\text{Ti}_4\text{Fe}_3\text{O}_{23}$. This compound would have an even higher concentration of magnetic Fe^{3+} ions in the inner three layers of each slab. Unfortunately the synthesis of this $n = 7$ compound was not successful yet. On the other hand, the magnetic interaction might be increased by the consideration of different magnetic ions, e.g. Mn^{3+} , on the B cation sites. As a result a (anti-)ferromagnetic ordering might appear.

4.2 Overlooked superstructure reflections

In the literature lattice parameters are given for many $A_n\text{B}_n\text{O}_{3n+2}$ compounds and crystal structures are described for several of them. Most compounds are of the type $n = 4, 4.5$ or 5 . Compounds with non-integer values other than 4.5 are relatively rare. Different monoclinic or orthorhombic space groups have been assigned to these compounds. Often compounds with the same n but different elements are described by different symmetries. Most compounds have been studied by X-ray powder diffraction, but only a few structures have been investigated by single-crystal X-ray diffraction.

Especially powder diffraction often leads to lattices with unit cell volumes smaller than cells concerning the tilting of the octahedra. This results either from a reduction of the length of the **a** axis to a value which is equivalent to the height of one BO_6 octahedron, e.g. in structure proposed for $\text{Ca}_2\text{Nb}_2\text{O}_7$ (Ishizawa et al., 1980), $\text{La}_2\text{Ti}_2\text{O}_7$ (Schmalle et al., 1993) or $\text{La}_4\text{Sr}_2\text{Ti}_6\text{O}_{20}$ (Canales-Vazquez et al., 2004). Alternatively, a reduction of the length of the stacking axes to a value

equal to the width of only one slab appears, e.g. used by Lichtenberg et al. (2008) for $\text{Sr}_2\text{LaTa}_3\text{O}_{11}$, Titov et al. (2005a) for $\text{La}_5\text{Ti}_4\text{FeO}_{17}$ or Levin et al. (1998) for $\text{SrNb}_4\text{Ti}_2\text{O}_{20}$.

Evidently, both effects of apparently shorter axes are reasoned in the overlook of weak superlattice reflections, which appears as a consequence of octahedra tilting. The overlook in the first kind of superlattice seems to appear only for compounds with even n . Because in compounds with $n = \text{odd}$ the BO_6 octahedra of equivalent layers in neighboring slabs are additionally shifted by $\frac{1}{2}\mathbf{c}_m$ compared with the $n = \text{even}$ compounds, where these octahedra are only shifted along \mathbf{a} with respect to each other (Fig. 4.1). The lack of the latter kind of superlattice reflections is most often combined with the assumption of an orthorhombic symmetry. Thus the octahedra tilting is not (completely) included in these structure descriptions.

In other compounds the observed orthorhombic structures might only represent the average structure of a modulated structure. This happened for example for $\text{Sr}_2\text{Nb}_2\text{O}_7$. There the modulation of the structure was confirmed by Daniels et al. (2002) after the analysis of the intensities of main and satellite reflections measured with synchrotron radiation. Whereas the average structure was already known since their determination by Nanamatsu et al. (1975).

Consequently, X-ray diffraction techniques, which are not able to resolve the weak superlattice reflections are not suitable for the analysis of the perovskite-related structures $A_nB_nO_{3n+2}$. The superlattice reflections are not visible in the powder diffractograms, resulting from the loss of information caused by the projection of the 3D space onto a 1D axis. Therefore powder X-ray diffraction is not a suitable technique for a precise determination of these structures. But also by the use of single-crystal X-ray diffraction techniques superlattice reflections might be overlooked. Either a point detector is used for the experiments and the reflections are not measured, because a wrong idea of the structure with a smaller unit cell is considered. Or by use of an area detector system the exposure time is not adapted to resolve superlattice reflections.

Chapter 5

Diffraction experiments with area detectors

5.1 Experiments on a Mar345dtb diffractometer

The collection of intensity data for both compounds $\text{La}_n(\text{Ti,Fe})_n\text{O}_{3n+2}$ with $n = 5$ and 6 were performed at the Laboratory of Crystallography, University of Bayreuth, by use of a Marresearch Mar345dtb diffractometer (Fig. 5.1). The use of this area detector system allows the measurement of a large number of reflections. The diffractometer is equipped with a Mar345 Image Plate (IP), which has a diameter of 345 mm. For each digitized image this corresponds to 2300×2300 pixels with a pixelsize of $150 \times 150 \mu\text{m}^2$. The possible maximum of measured intensity of a reflection is limited by the dynamic range of the detector, which is 17 bit. This correspond to possible intensities from 0 to 131071 counts.

The IP contains layers of photo-stimulable phosphor of europium-doped barium halides ($\text{BaF}(\text{Br,I}):\text{Eu}^{2+}$), that store the information of incident photons in form of a photo-induced transfer of electrons from the europium ions to the halide vacancies (Giacovazzo et al., 2002). The information can be read out by a stimulated emission caused by red laser light (wavelength of 633 nm). The wavelength of the emitted light is 390 nm (3.2 eV) and is detectable by a photomultiplier (Glusker and Trueblood, 2010). The number of the emitted blue photons is proportional to the amount of absorbed X-ray photons. After reading the IP is erased by strong visible light from halogen lamps and ready for another exposure to X-rays. Area detectors offer the possibility of simultaneous measurement of several reflections. Thus the measurement time is much shorter compared with that by use of a point detector. Moreover,

IP detectors are especially suitable for the measurement of weak reflections, because of a low noise level. On the other hand, the reflection intensities determined by use of a point detector are more precise than those resulting from a measurement with an area detector, because the counting statistics of the first reduce the standard uncertainties of the reflection intensities (Giacovazzo et al., 2002).

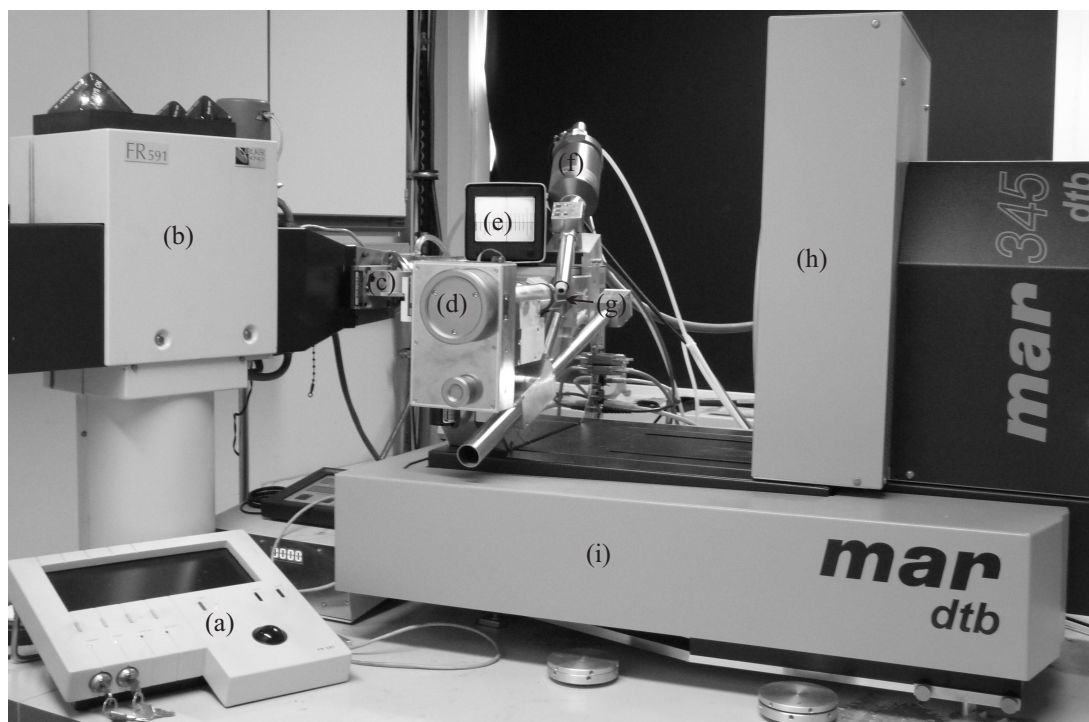


Figure 5.1: Setup of the Mar345dtb Image-Plate diffractometer with attached Cryostream open-flow nitrogen cryostat (installed at the Laboratory of Crystallography, University of Bayreuth). (a) Control panel of (b) rotating anode, (c) monochromator, (d) ϕ axis, (e) screen for control of crystal alignment, (f) cooling system, (g) goniometer head with crystal, (h) IP detector and (i) diffractometer baseplate with tracks for changing distance and tilt of the detector.

The X-ray radiation is generated by a rotating anode with a molybdenum target, which is operated at a power of 4.1 kW with a voltage of 55 kV and a current of 75 mA. The goniometer of the Mar345dtb diffractometer possesses only one axis for rotation of the crystal around the ϕ axis, which is oriented perpendicular to the direction of the primary beam (Fig. 5.1). To increase the maximum resolution the IP is mounted on a motorized 2θ arm, which can reach up to 30° offset

for a maximum possible resolution of $d = 0.48 \text{ \AA}$ for molybdenum radiation. Data collections are automatically carried out by use of the Mar345dtb software (Klein, 2012) after the experimental parameters for each run are defined. During the measurement the crystal is rotated about ϕ in increments with a constant speed. For each increment a separate frame is stored, which contains the information about the diffracted intensities. Additionally for all frames of one set the information about the collimator (slit width) and beam settings (wavelength, beamsize), the exposure settings (exposure time, total number of frames in the set, width of increments $\Delta\phi$) and the goniometer settings (2θ offset, starting angle ϕ_0 , crystal-detector distance) are stored. The combination of this information is used in the integration software programs (e.g. EVAL15; Chapter 5.2) for the determination of the crystal orientation expressed in the coordinate system of the diffractometer. Thus the orientation matrix, which contains this information, is used for the identification of the Miller indices of the reflections and for the integration of their intensities, which are mostly distributed over a few frames.

For $\text{La}_n(\text{Ti,Fe})_n\text{O}_{3n+2}$ each data set consisted of four runs with varying 2θ offset (0 and 30°) and exposure time (up to 384s). This enabled the measurement of strong reflections without overexposure besides weak superlattice reflections having sufficient intensities even at high 2θ values. The individual runs were combined and scaled to each other utilizing EVAL15. This resulted in complete sets of diffraction data up to a resolutions of $[\sin(\theta)/\lambda]_{\max} = 0.89 \text{ \AA}^{-1}$. The measurement of ϕ ranges of 180 or 360° in each of the runs enhanced the redundancy of the final data. A crystal-to-detector distance of 150 mm and an increment of $\Delta\phi = 0.5^\circ$ enabled the separation of closely spaced neighboring reflections. Experimental details for the individual temperatures are given in Table 7.1.

As already discussed in chapter 3.1.2 measurements at low temperatures require a stable sample cooling. On the Mar345dtb diffractometer the crystal temperature was selected by use of a Cryostream open-flow nitrogen cryostat (Oxford Cryosystems). It works similar to the helium open-flow cryostat described in chapter 3.1.2, but uses nitrogen instead of helium. This cryogen limits the lowest reachable temperature to about 80 K. By use of electrical heating the gas can be brought up to almost 500 K (Fig. 5.2 (a)).

For the application of the open-flow cryostat the crystal should be mounted in a way, which avoids thermal conduction between the crystal and the goniometer head, in contrast to the crystal preparation for the use with the closed-cycle cryostat described in chapter 3.1.2. Therefore, the crystal is pasted with the help of a few

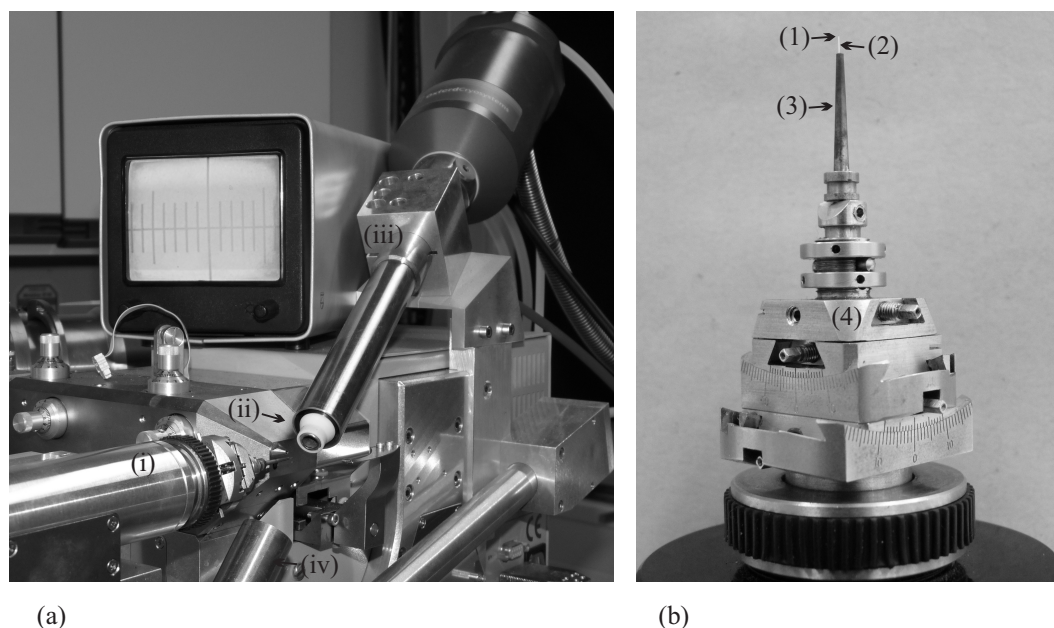


Figure 5.2: Low temperature measurements on the Mar345dtb diffractometer (installed at the Laboratory of Crystallography, University of Bayreuth). (a) Setup of the Cryostream open-flow nitrogen cryostat and (b) crystal preparation on a glass fiber. Parts of the cooling device: (i) ϕ axis with attached goniometer head and crystal, (ii) nozzle of (iii) the cryostat for the cold nitrogen stream pointing to the crystal and (iv) suction tube for the exhaust of the cold gas. The crystal (1) is glued to boron glass fiber (2), which is glued in the copper pin (3). The pin is screwed onto a goniometer head (4).

drops of two-component glue on the top of a boron glass fiber. The fiber is glued with the same glue to a copper pin. The height of the crystal over the goniometer head is in total about 22.5 mm, 20 mm from the length of the copper pin plus additional 2.5 mm from the glass fiber. The diameter of the glass fiber is optimal between 0.05 and 0.1 mm. A thicker fiber would absorb a noticeable amount of the X-ray radiation, while a thinner fiber would oscillate in the nitrogen gas stream (Fig. 5.2 (b)).

5.2 Integration with EVAL15

The processing of the measured intensities of $\text{La}_n(\text{Ti,Fe})_n\text{O}_{3n+2}$ with $n = 5$ and 6 was performed by use of EVAL15. The term EVAL15 denotes the complete EVAL15

program suite as well as the key component of the program suite, which is doing the integration. Unlike other integration programs (e.g. CRYSTALIS Pro software (Oxford Diffraction, 2006)) the EVAL15 method is based on an ab-initio calculation of the three-dimensional reflection profiles on the basis of a few known parameters of the crystal, the diffractometer and the experiment. These parameters are the crystal size, crystal shape and mosaicity of the crystal, the diffractometer geometry, detector type and point spread of the detector as well as the wavelength, divergence and focus technique of the beam. The method is described in detail by Schreurs et al. (2010). As an advantage EVAL15 can handle incommensurate modulated structures as well as periodic ones, what is not possible in most other integration programs. Moreover, it can be used independent of the choice of the diffractometer and is not limited to diffractometers or detectors of a single manufacturer. At the laboratory of Crystallography EVAL15 has been adapted for successful integrations of data from the Mar345dtb IP diffractometer, of data from synchrotron experiments at the HASYLAB beamlines D3 and F1, Hamburg, as well as of neutron diffraction data measured at FRM II, Garching.

For both $\text{La}_n(\text{Ti,Fe})_n\text{O}_{3n+2}$ compounds the intensities were integrated on basis of a monoclinic unit cell with a length of the stacking axis equal to $c_m = 31.5906 \text{ \AA}$ and $c_m = 37.1469 \text{ \AA}$ for $n = 5$ and 6 , respectively. These long axes were still successfully described by use of EVAL15, but especially the latter value is at the limit of separation of neighboring reflections for the used crystal-to-detector distance. A larger distance between crystal and detector would increase the separation, but at the same time the divergence of the beam increases the reflection area on the detector. Therefore, the overlap problem is not solved completely in that way. On the other hand with increasing crystal-to-detector distance the $(\frac{\sin \theta}{\lambda})_{max}$ value is reduced. As a consequence less unique reflections are measured and the number of refineable parameters of the structure is decreased. Thus the upper limit of unit cell parameters for a successful structure solution is about 40 \AA by use of EVAL15, when the diffraction data is collected with conventional X-rays sources.

The EVAL15 program suite consists of a few individual programs, which are used for different steps in the procedure of reflection indexing and data integration. The procedure starts with an inspection of the frames in the program VIEW (Schreurs et al., 2010)¹ (Fig. 5.3). The orientation of the crystal is found by help of DIRAX (Duisenberg, 1992) and refined with PEAKREF, together with experimental

¹For all programs given without individual references.

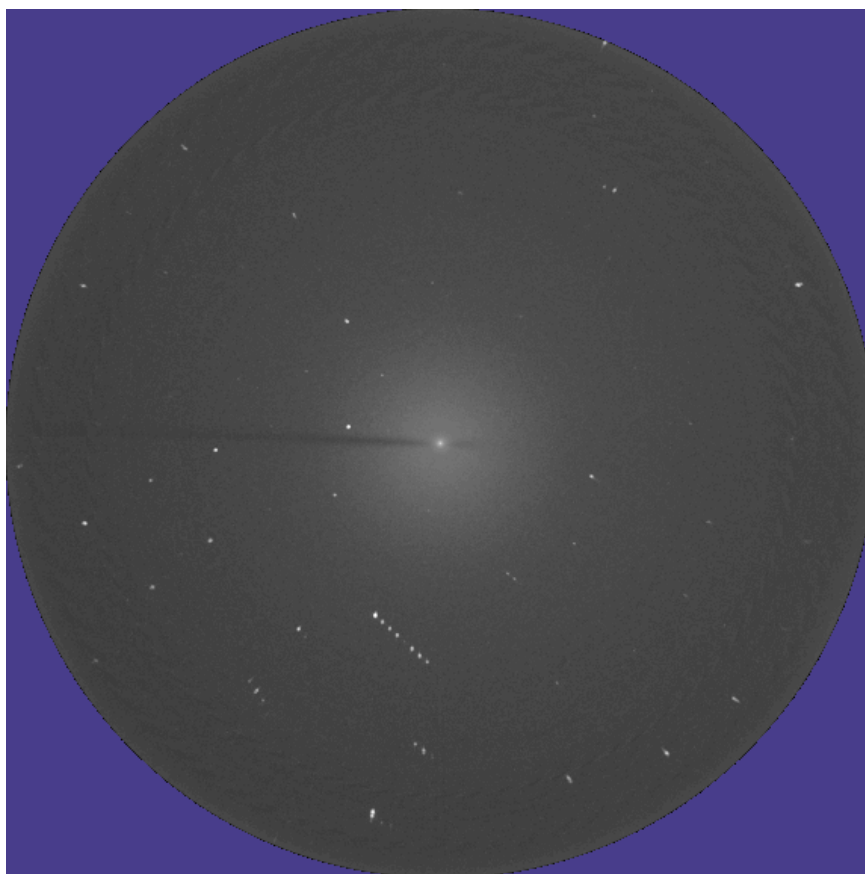


Figure 5.3: Program window from the EVAL15 program suite. One frame of $\text{La}_5(\text{Ti}_{0.80}\text{Fe}_{0.20})_5\text{O}_{17}$ ($n = 5$) plotted with VIEW. The black sphere represent the sensitive area of the detector, while reflections are drawn as light spots. In the lower part a series of neighboring reflections (2 3 l) is visible, with l ranging from 5 to 12.

parameters like crystal-to-detector distance. With this information the reflections are indexed. For the refinement the angular positions of the reflections are obtained from the frames using BUILDSEARCH. After all parameters are sufficiently well described by the refined values the intensities of the reflections are gathered from the frames using BUILDDATCOL. For the integration of the data the experimental parameters are combined with information about the crystal, e.g. mosaicity, and the detector, e.g. point spread. The latter properties can be refined in EVAL15, which is also performing the integration (Fig. 5.4). In an analysis the quality of the integration process is checked by use of ANY. The integrated intensities are scaled and corrected for absorption by use of SADABS (Sheldrick, 2008). The output files of

SADABS can be utilized by several structure refinement programs, e.g. JANA2006 (Petricek et al., 2006). A case study for the use of EVAL15 has been given by Li (2010) for the incommensurately modulated structure of Rb_2ZnCl_4 .

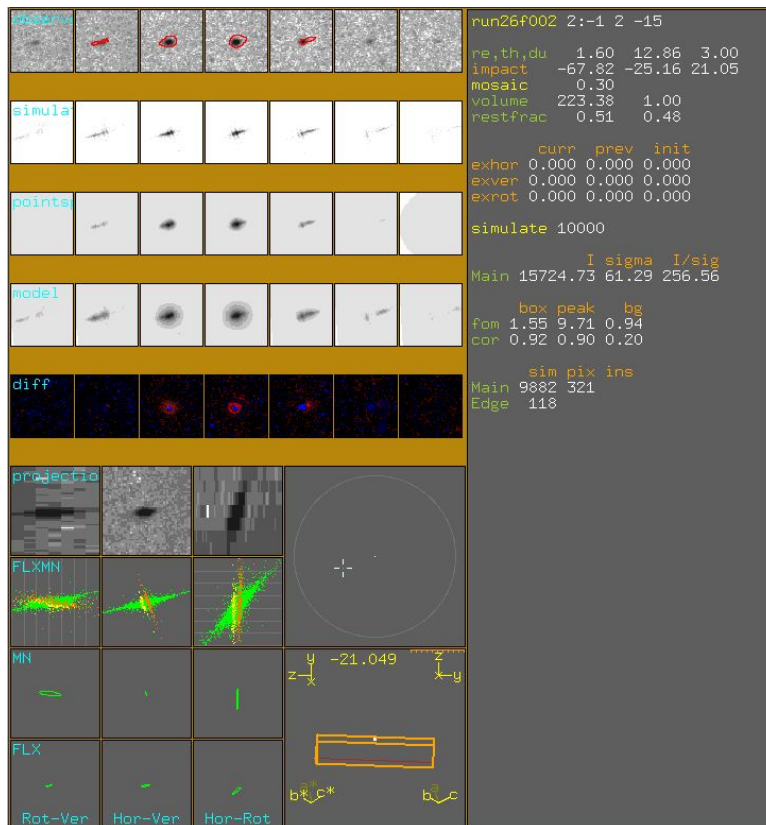


Figure 5.4: A EVAL15 program window for the reflection $(\bar{1}, 2, \bar{15})$ with refined crystal orientation and mosaicity.

5.3 Unit cell determination with a Huber four-circle diffractometer

Determination of the thermal evolution of the unit cell parameters of a compound requires the precise measurement of the reflection angles, which describe the crystal orientation and detector position. The best experimental X-ray device for this purpose is a four-circle diffractometer with a point detector. Because the determination of the angles in this way is more accurate than by extraction of these parameters

from the frames of area detector data sets. At the Laboratory of Crystallography, University of Bayreuth, the evolution of unit-cell parameters can be studied on a Huber four-circle single-crystal diffractometer with Mo- $K\alpha$ radiation from a sealed X-ray tube (Fig. 5.5). Because of its larger dimensions it allows an even more precise determination than the Mach3 diffractometer (Chapter 3.2).

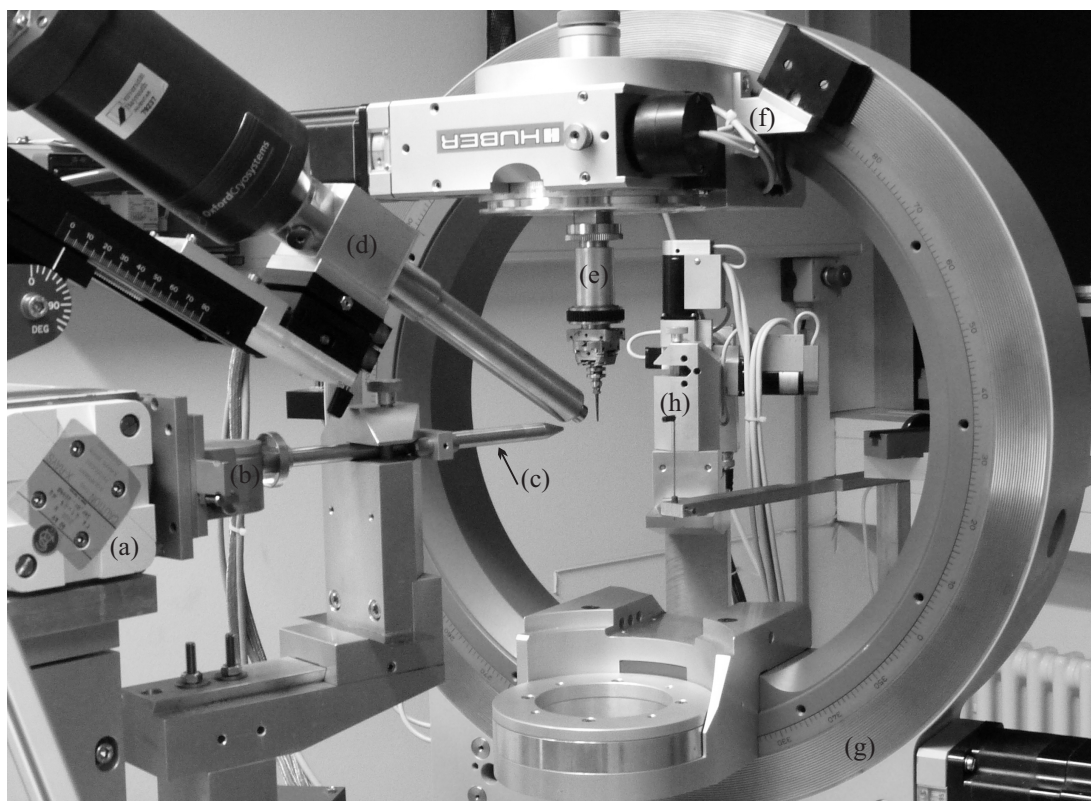


Figure 5.5: Setup of a Huber four-circle diffractometer using the Euler-geometry with attached Cryostream open-flow nitrogen cryostat (installed at the Laboratory of Crystallography, University of Bayreuth). (a) Sealed X-ray tube, (b) monochromator, (c) primary beam collimator, (d) cooling system, (e) ϕ axis with attached goniometer head and crystal, (f) χ block for the movement on (g) the Euler cradle and (h) point detector mounted on the 2θ arm.

By use of this diffractometer exact unit cell parameters are obtained from the angular information of about 25 reflections in the range $40^\circ \leq 2\theta \leq 50^\circ$, which are distributed as uniformly as possible over the three reciprocal lattice directions of the crystal. Each reflection is measured in four equivalent positions (Table 5.1)

eliminating any errors in crystal centering on the diffractometer and the errors in the zero positions of the diffractometer circles (Gollwitzer, 2004). Sample temperatures are selected using an identical Cryostream nitrogen cryostat as on the Mar345dtb diffractometer (Chapter 5.1).

Table 5.1: List of the angular values 2θ , ω , χ and ϕ of the four equivalent positions of a reflection in Euler geometry (Eichhorn, 1993).

No.	angles of equivalent positions			
1	2θ	ω	χ	ϕ
2	-2θ	$-\omega$	$180^\circ + \chi$	ϕ
3	-2θ	$-2\theta + \omega$	$-\chi$	$180^\circ + \phi$
4	2θ	$2\theta - \omega$	$180^\circ - \chi$	$180^\circ + \phi$

For $\text{La}_5(\text{Ti}_{0.80}\text{Fe}_{0.20})_5\text{O}_{17}$ ($n = 5$) the evolution of the unit-cell parameters was studied by this method by Philipp Dorscht in the framework of his bachelor thesis in close collaboration with the author of the present thesis. Unit-cell parameters determined at 18 different temperatures in the range from 90 to 370 K agreed well with those determined from the IP frames by use of EVAL15, but showed smaller standard derivations. The evolution of the unit-cell parameters is given in Chapter 7.

Chapter 6

Commensurate charge-density wave with frustrated interchain coupling in SmNiC_2 ¹

6.1 Introduction

Ternary carbides RTC_2 containing a rare-earth (R) and a transition-metal (T) element have been synthesized in the 1980s for the complete series of rare-earth elements and several transition metals, like Mn, Fe and Ni (Bodak and Marusin, 1979; Semenenko et al., 1983; Jeitschko and Gerss, 1986). The rare-earth elements are responsible for the paramagnetic properties and the development of antiferromagnetic (AF) order at low temperatures in most compounds $R\text{NiC}_2$ (Yakinthos et al., 1990; Onodera et al., 1998). Exceptions are LaNiC_2 , which is non-magnetic and develops superconductivity with $T_C = 2.7$ K (Subedi and Singh, 2009), and SmNiC_2 , which becomes ferromagnetic (FM) below $T_C = 17.7$ K (Onodera et al., 1998).

The phase diagram of SmNiC_2 is complicated by the appearance of a charge-density wave (CDW) below $T_{\text{CDW}} = 148$ K (Murase et al., 2004). Satellite reflections have been found in X-ray diffraction below T_{CDW} at incommensurate positions given by the modulation wave vector $\mathbf{q}_{\text{CDW}} = (0.5, \sigma_2, 0)$ with $\sigma_2 = 0.516$ at $T = 60$ K (Shimomura et al., 2009). The CDW disappears at T_C where FM order develops.

Compounds $R\text{NiC}_2$ and $R_5\text{Ir}_4\text{Si}_{10}$ —both containing rare earth elements—are of interest, because they are atypical, strong-coupling CDW systems and provide the

¹This chapter has been published as: Wölfel, A., Li, L., Shimomura, S., Onodera, H. and van Smaalen, S.: Commensurate charge-density wave with frustrated interchain coupling in SmNiC_2 ; *Phys. Rev. B*, **82**: 054120 (2010)

opportunity to study the interplay between CDWs and magnetism (Becker et al., 1999; Shimomura et al., 2009). Like SmNiC_2 , $\text{Er}_5\text{Ir}_4\text{Si}_{10}$ has an incommensurate CDW below 155 K, but it develops antiferromagnetic (AF) order below $T_N = 2.8$ K (Galli et al., 2000). $\text{Lu}_5\text{Ir}_4\text{Si}_{10}$ has a commensurate CDW below 83 K (Becker et al., 1999); it is non-magnetic and develops superconductivity below 3.9 K (Shelton et al., 1986). Unlike SmNiC_2 , the CDWs persist in the AF and superconducting phases of these compounds (Becker et al., 1999; Galli et al., 2002).

Similarities between the CDWs in SmNiC_2 and $\text{Er}_5\text{Ir}_4\text{Si}_{10}$ include anomalies at the respective transition temperatures in the temperature dependencies of the electrical resistivity, the lattice parameters and the specific heat (Murase et al., 2004; Shimomura et al., 2009; Galli et al., 2000). The temperature dependencies of the magnetic susceptibility exhibit clear anomalies at T_C or T_N , but the CDW transitions are invisible in these experiments (Onodera et al., 1998; Galli et al., 2000). This has been explained by the large contribution of local moments to the susceptibility as opposed to the contributions of Pauli paramagnetism (Galli et al., 2000; Shimomura et al., 2009).

Canonical CDW compounds are characterized by a large anisotropy of their electrical resistivity, with the direction of the lowest resistivity defining the direction of the CDW (Gruener, 1994). A strong interchain coupling is responsible for a much lower anisotropy for $R\text{NiC}_2$ and $R_5\text{Ir}_4\text{Si}_{10}$ than found in canonical CDW systems, with values of $\rho_c/\rho_a \approx 5.0$ and $\rho_b/\rho_a \approx 2.8$ for SmNiC_2 (Shimomura et al., 2009), and of $\rho_a/\rho_c = \rho_b/\rho_c \approx 2.4$ for $\text{Er}_5\text{Ir}_4\text{Si}_{10}$ (Galli et al., 2000). However, an important difference exists between these compounds. In $\text{Er}_5\text{Ir}_4\text{Si}_{10}$ the \mathbf{c} -axis is the direction of both the smallest resistivity and the incommensurate CDW with $\mathbf{q} = (0, 0, \sim 0.22)$. For SmNiC_2 the incommensurate component of \mathbf{q}_{CDW} is along \mathbf{b}^* , suggesting an incommensurate CDW along \mathbf{b} , while the lowest resistivity is along \mathbf{a} , suggesting the \mathbf{a} -axis as direction of the CDW. Electronic band-structure calculations of SmNiC_2 have indicated a CDW wave vector of $(0.5, 0.56, 0)$, close to the observed \mathbf{q}_{CDW} (Laverock et al., 2009). However, the published Fermi surface is composed of warped planes perpendicular to \mathbf{a} (Laverock et al., 2009), a feature which would support the interpretation of \mathbf{a} as the direction of the CDW, in agreement with the classical picture of band structures of CDW materials (Gruener, 1994).

Here we will show that the CDW in SmNiC_2 should be interpreted as a commensurate CDW centered on chains of Ni atoms along \mathbf{a} . The observed pairing of Ni atoms is intrinsically frustrated on the lattice of SmNiC_2 , and this frustration is proposed to be responsible for the incommensurate component of $\sigma_2 \approx 0.516$.

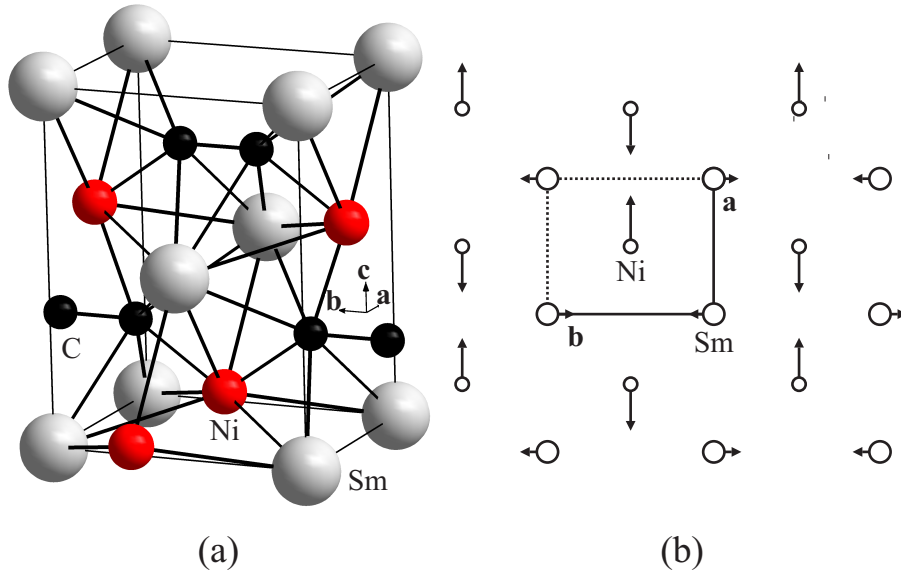


Figure 6.1: (a) Crystal structure of SmNiC₂. (b) One layer of Sm/Ni atoms with atomic displacements (multiplied by 25) due to the modulation indicated by arrows for $t = 0.246$.

6.2 Experimental

Single-crystalline material of SmNiC₂ has been used as described before (Shimomura et al., 2009). A crystal of dimensions $0.12 \times 0.06 \times 0.035 \text{ mm}^3$ was selected for X-ray diffraction experiments using synchrotron radiation of wavelength 0.5600 \AA . The crystal was glued to a carbon fiber that was attached to the cold finger of a closed-cycle helium cryostat mounted on the Huber four-circle diffractometer at beamline D3 of HASYLAB at DESY, Hamburg, Germany. X-ray diffraction was measured with a scintillation detector at selected temperatures between 9 K and room temperature. Preliminary X-ray diffraction experiments have been performed on a Nonius Mach3 diffractometer with Mo-K α radiation from a rotating anode generator. They confirmed the orthorhombic CeNiC₂ structure type with space group $Amm2$ and lattice parameters $a = 3.7037(3)$, $b = 4.5279(2)$ and $c = 6.0947(4) \text{ \AA}$ at room temperature, in agreement with previous studies [Fig. 6.1(a)] (Bodak and Marusin, 1979; Jeitschko and Gerss, 1986).

The crystal shape was determined by refinement against ψ scans of selected reflections, and it was subsequently used for absorption correction of the intensity data (see below).

The synchrotron experiment was used to determine the orthorhombic lattice parameters at low temperatures. At $T = 60$ K they are $a = 3.6965$ (5), $b = 4.5293$ (7) and $c = 6.0955$ (8) Å. In a first experiment so-called ω - 2θ maps were measured for the three reflections $(0\ 2\ \bar{2})$, $(2\ 0\ \bar{4})$ and $(2\ \bar{2}\ 0)$. For this purpose the detector slits were set to 6×0.02 mm², corresponding to an acceptance angle in the direction of 2θ of 0.0031° . Centered on each reflection ω -scans of 101 steps were carried out for a series of 81 2θ -values with step sizes of 0.003° in ω and 0.002° in 2θ . The results give the diffracted intensity as a function of the orientation of the crystal and the scattering angle. For the orthorhombic lattice all reflections are expected to appear as single peaks. A splitting of one of the three reflections $(0\ 2\ \bar{2})$, $(2\ 0\ \bar{4})$ and $(2\ \bar{2}\ 0)$ would indicate a monoclinic lattice distortion, with monoclinic angle α , β or γ , respectively. At 60 and 9 K all ω - 2θ maps exhibit single maxima (Fig. 6.2). These results show that the lattice remains orthorhombic in both the CDW and the FM-ordered phases.

Within the CDW phase, q -scans along \mathbf{b}^* and centered on $(0.5\ 3\ \bar{2})$ confirmed the presence of satellite reflections with modulation wave vector \mathbf{q}_{CDW} and $\sigma_2 = 0.516$ at a temperature of 60 K. Employing this modulation wave vector, intensities were measured by ω -scans of the Bragg reflections $(h\ k\ l\ m)$ up to $\sin(\theta)/\lambda = 0.74$ Å⁻¹. All main reflections ($m = 0$) and first-order satellites ($|m| = 1$) were measured. ω -Scans at the positions of 71 second-order satellites ($|m| = 2$) up to $\sin(\theta)/\lambda = 0.41$ Å⁻¹ and of 84 second-order satellites for $0.57 < \sin(\theta)/\lambda < 0.74$ Å⁻¹ showed that they were too weak to be measured in our experiment. Integrated intensities were corrected for Lorentz and polarization effects and for absorption. Averaging in point symmetry $mm2$ resulted in a data set of 119 main reflections and 192 first-order satellite reflections, of which 119 respectively 185 reflections had intensities larger than three times their standard uncertainties (observed reflections).

The modulated crystal structure has been described within the superspace approach, with a symmetry given by the superspace group $Amm2(\frac{1}{2}\ \sigma_2\ 0)000$ (van Smaalen, 2007; Janssen et al., 2006). The intensities of the first-order satellite reflections could be described by a displacive modulation consisting of single-harmonic functions for all three crystallographically independent atoms in the unit cell of the average structure:

$$u_i(\bar{x}_{s4}) = A_i \sin(\bar{x}_{s4}) + B_i \cos(\bar{x}_{s4}) \quad (6.1)$$

for $i = x, y, z$ and with $\bar{x}_{s4} = t + \mathbf{q}_{\text{CDW}} \cdot \mathbf{x}^0$, where t is the phase of the modulation wave and \mathbf{x}^0 are the basic-structure coordinates. Structure refinements with the

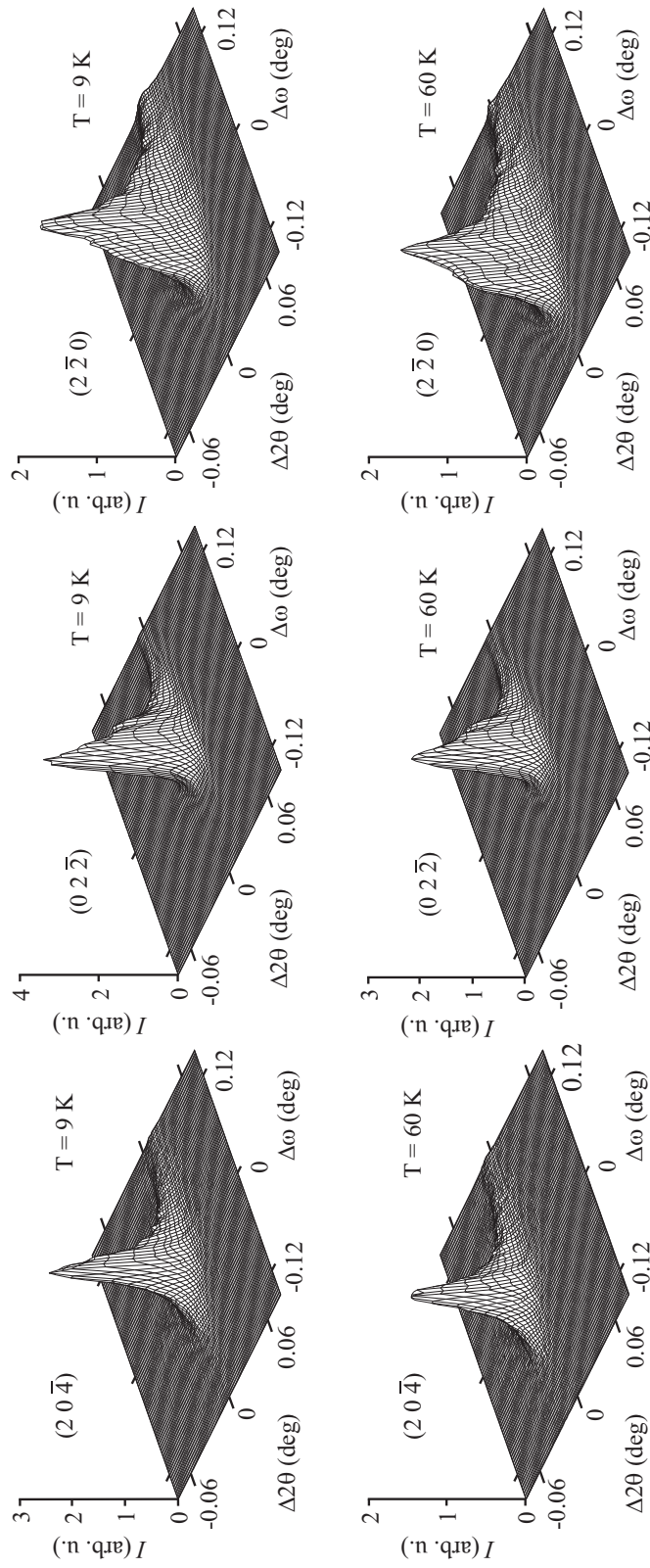


Figure 6.2: Diffracted intensity (I) as a function of scattering angle 2θ and crystal orientation ω for three reflections at the temperatures of 60 and 9 K. $\Delta 2\theta$ and $\Delta\omega$ indicate the deviations from the center of the scans. The Intensity is in arbitrary units.

computer program JANA2006 (Petricek et al., 2006) resulted in an excellent fit to the diffraction data with $R_F = 0.014$ for the main reflections and $R_F = 0.031$ for the satellites (Table 6.1).

Table 6.1: Structural parameters at $T = 60$ K. (x^0, y^0, z^0) are the fractional coordinates of the basic structure; modulation amplitudes according to Eq. 6.1 are given in \AA ; and the equivalent isotropic atomic displacement parameter is given in \AA^2 . Standard uncertainties are in parentheses. $B_y = A_z = 0$ for all atoms.

Atom	Sm	Ni	C
x^0	0	0.5	0.5
y^0	0	0.5	0.1519(21)
z^0	0	0.1115(2)	0.2948(16)
A_x (\AA)	0	-0.0501(5)	-0.0001(20)
B_x (\AA)	0	0	0.0200(23)
A_y (\AA)	0.0270(2)	0	0
B_z (\AA)	0.0116(1)	0	0
U_{iso}^{eq} (\AA^2)	0.0022(1)	0.0032(3)	0.0066(20)

6.3 Discussion

The crystal structure [Fig. 6.1(a)] does not allow a straightforward identification of the atomic chains carrying the quasi-one-dimensional (1D) valence band responsible for the CDW, since all atoms could contribute to it. In the basic structure at 60 K, shortest Ni–Ni and Sm–Sm distances are equal to the lattice parameter $a = 3.697$ \AA , and chains along \mathbf{a} of either type of atom would qualify as 1D system. The shortest distances between metal atoms are, however, between Ni and Sm with values of 3.001 (0) and 3.004 (1) \AA , while distances between atoms apart by the centering translation are equal to 3.797 (2) \AA and only slightly larger than the shortest distance between atoms of the same kind. Therefore, the low-dimensional electron band could be a mixed Sm/Ni band on layers perpendicular to \mathbf{c} or pure Sm or pure Ni bands on layers perpendicular to \mathbf{a} . Simple atomic chains along \mathbf{b} are unlikely because of the long distance of $b = 4.529$ \AA between those atoms. The identification of the 1D

system within the basic structure depends on the orbital contributions to the valence band and can only be obtained through electronic band-structure calculations.

A periodic lattice distortion is intrinsic to CDWs, because the gain of electronic energy is achieved through a modulation of the positions of the atoms carrying the low-dimensional valence band responsible for the CDW. Ni atoms exhibit the largest modulation amplitude (Table 6.1), and they should, therefore, carry the CDW. This interpretation is supported by the variation of interatomic bonding distances due to the modulation wave, which is by far the largest variation for the Ni atoms neighboring along \mathbf{a} (Fig. 6.3). The modulations of Sm and C follow those of Ni, such that the shortest interatomic distances remain as constant as possible (Fig. 6.3).

The crystal structure can be described as a stacking along \mathbf{c} of layers of Sm and Ni atoms, *i.e.* the layer at $z = 0$ contains Sm atoms at $z = 0$ and Ni atoms at $z = 0.1156$ [Fig. 6.1(a)]. Carbon atoms are located between the layers. In Fig. 6.1(b) the structure of one layer is given together with arrows indicating the atomic displacements due to the modulation wave for a phase of $t \approx 0.25$. The Ni atoms form dimerised chains along \mathbf{a} , suggesting this to be the direction of the CDW. Neighboring chains are out of phase, as it is imposed by elastic coupling via Ni–Sm–Ni bond paths. Only an antiphase relation between neighboring chains allows displacements of Sm atoms leading to the minimization of the variation of the shortest metal–metal bonds within the layers. The optimal modulation wavevector would be $(0.5, 0.5, 0)$ for single layers.

Neighboring layers are related by the A -center. Their phase difference would be 90° for a commensurate CDW with wavevector $(0.5, 0.5, 0)$. Atoms, which are modulated in one layer would have zero displacements in the neighboring layers. The resulting structure—although not impossible—appears unlikely, because all Ni atoms have identical environments and only half of them would participate in the CDW. On the other hand, unequal modulations of Ni atoms would imply the loss of the A -center, in which case symmetry would not enforce a relation between the modulations of Ni atoms on neighboring layers. The A -center appears to provide a perfect frustration between the modulations on chains of nickel atoms in neighboring layers, which can only be resolved by zero modulation amplitude on every second layer, or by an incommensurate coupling between the layers—as it is the observed experimentally. This explains the incommensurability of the second component, $\sigma_2 = 0.516$, of \mathbf{q}_{CDW} .

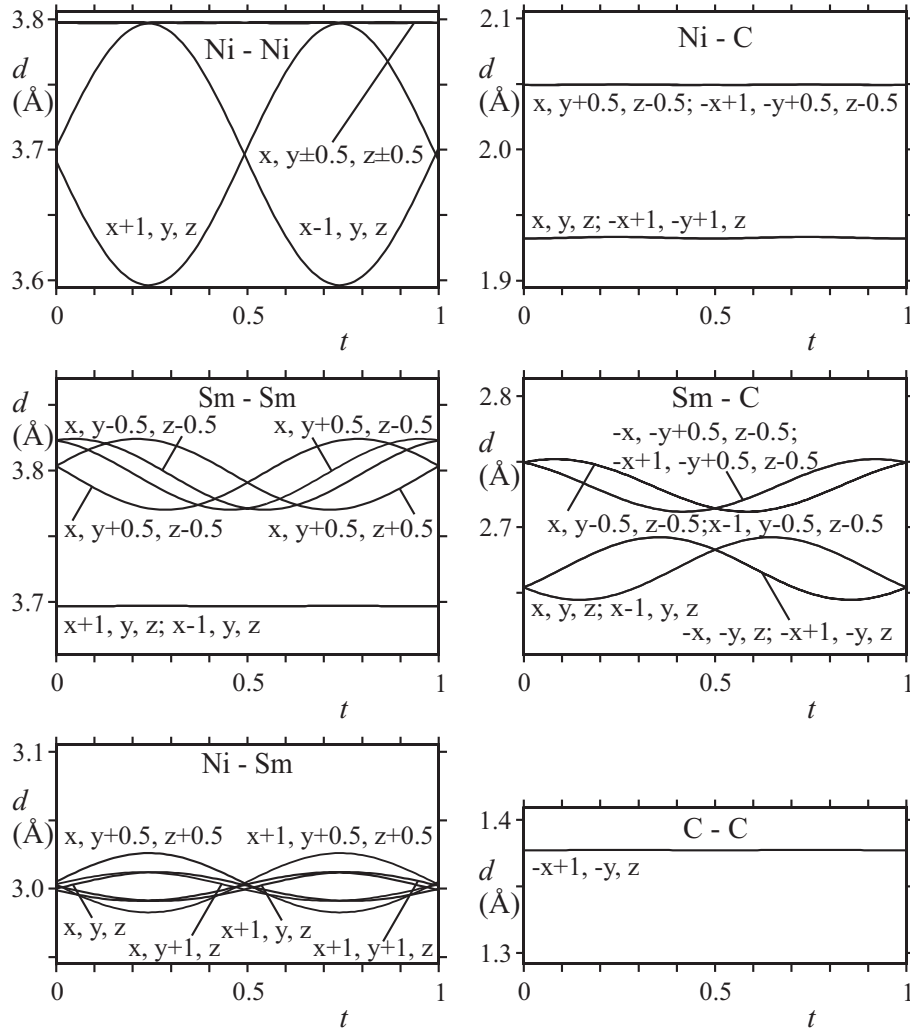


Figure 6.3: Interatomic distances (d) as a function of the phase t of the modulation wave. Symmetry operators apply to the second atom in each pair. Atomic coordinates from Table 6.1

Carbon is present in the structure as C_2 units with a C–C distance of 1.376 (13) Å, almost equal to a typical value for a C–C double bond. This distance does not vary in the modulated structure, indicating that carbon does not participate in the CDW, because any variation of the charge-transfer between carbon and the metal atoms would have modified the character, and therefore the length of the C–C bond.

The electronic band structure of $SmNiC_2$ —calculated within the local density approximation—has led to the identification of a maximum in the electronic susceptibility at a wavevector of $(0.5, 0.56, 0)$, close to the observed incommensurate modulation wavevector of the CDW (Laverock et al., 2009). The nesting condition is, however, between parts of the Fermi surface that are warped planes perpendicular to the direction of \mathbf{a} , and separated by the commensurate value of $\sigma_1 = 0.5$. The other non-zero component of \mathbf{q}_{CDW} is parallel to the Fermi surface and it is explained by the warped character of these planes in a way similar to that for canonical CDW systems like $NbSe_3$ (Schäfer et al., 2001). In those cases the parallel component has always been commensurate, while in the present case it has been found to be incommensurate.

We have demonstrated here that there is frustration between the CDW modulations on neighboring atomic planes perpendicular to \mathbf{c} , and we propose that this frustration is responsible for the incommensurability of second component of the CDW wavevector. The frustration pertains to the periodic lattice distortion intrinsic to the CDW, but it is also reflected in the electronic band structure, thus explaining the incommensurability of the nesting vector found in Ref. Laverock et al. (2009).

Important evidence for the direction of the CDW comes from fluctuations above T_{CDW} , as they can be observed by diffuse X-ray scattering. Shimomura *et al.* (Shimomura et al., 2009). have reported the temperature dependence of the diffuse scattering in the $\mathbf{b}^*, \mathbf{c}^*$ plane, *i.e.* concentrating on the direction given by the incommensurate component of \mathbf{q}_{CDW} . A re-analysis of those data, now including the diffuse scattering at $T = 160$ K in the $\mathbf{a}^*, \mathbf{b}^*$ plane, shows that the correlation lengths at this temperature are 116 Å along \mathbf{a} and 94 Å along \mathbf{b} . The longer correlation length along \mathbf{a} supports the notion that \mathbf{a} rather than \mathbf{b} is the direction of the CDW. It would be interesting to obtain these correlation lengths as a function of temperature up to at least room temperature. The proposed direction of the CDW chains along \mathbf{b} would require a slower decrease of the correlation length along \mathbf{b} than along \mathbf{a} . Such experiments would require a considerable amount of beam time at a synchrotron source, and they are beyond the scope of the present work.

6.4 Conclusions

We have shown that the lattice of SmNiC_2 remains orthorhombic within the CDW and ferromagnetic phases. The incommensurately modulated structure provides compelling evidence for a CDW that is centered on the chains of Ni atoms along \mathbf{a} . The observed CDW should be interpreted as a commensurate CDW (twofold superstructure) centered on the chains of Ni atoms along \mathbf{a} , which then have a frustrated three-dimensional coupling, leading to the observed incommensurability of the modulated structure of the CDW state. Of course, the present analysis does not exclude possible contributions of Sm orbitals to the low-dimensional valence band.

Chapter 7

Anisotropic thermal expansion of $\text{La}_n(\text{Ti,Fe})_n\text{O}_{3n+2}$ ($n = 5$ and 6)¹

7.1 Introduction

$\text{La}_5(\text{Ti}_{0.8}\text{Fe}_{0.2})_5\text{O}_{17}$ ($n = 5$) and $\text{La}_6(\text{Ti}_{0.67}\text{Fe}_{0.33})_6\text{O}_{20}$ ($n = 6$) belong to the homologous series $\text{A}_n\text{B}_n\text{O}_{3n+2}$, where $\text{A} = \text{Ca}, \text{Sr}, \text{La}, \text{Ce}, \text{Pr}, \text{Nd}$ or Sm , $\text{B} = \text{Mg}, \text{Al}, \text{Ti}, \text{V}, \text{Cr}, \text{Mn}, \text{Fe}, \text{Ta}, \text{Ga}, \text{Nb}$ or Yb , and $2 \leq n \leq 7$. The crystal structures comprise slabs of perovskite-type structure of n octahedra thick stacked along \mathbf{b} and separated by oxygen-rich layers (Fig. 7.1). The stoichiometry is ABO_y with $y = 3 + \frac{2}{n}$.

At high temperatures or as hypothetical high-symmetry structures $\text{A}_n\text{B}_n\text{O}_{3n+2}$ compounds are centrosymmetric with unit cells $a_o = a_c$, $b_o = (n + 1)\sqrt{2}a_c$ and $c_o = \sqrt{2}a_c$, where a_c is the lattice parameter of a cubic perovskite structure ABO_3 (Levin and Bendersky, 1999). Symmetries are given by orthorhombic spacegroups Immm for n is odd or Cmcm for n is even. In the temperature range which is investigated here, compounds $\text{A}_n\text{B}_n\text{O}_{3n+2}$ either have incommensurately modulated structures (Daniels et al., 2002), or fourfold superstructures of the orthorhombic basic structure (Scheunemann and Müller-Buschbaum, 1975; Daniels et al., 2003; Guevarra et al., 2005b; 2007). The formation of superstructures is caused by tilting of BO_6 octahedra and results in a monoclinic lattice distortion with spacegroups $\text{P2}_1/\text{b}$ (No. 14, c unique) for n is odd and P2_1 (No. 4, c unique) for n is even. Superlattice reflections are weak and have been overlooked in several previous studies (Drews et al., 1996; Abrahams et al., 1998; Titov et al., 2005a;b).

¹This chapter has been submitted for publication as: Wölfel, A., Dorscht, P., Lichtenberg, F. and van Smaalen, S.: Anisotropic thermal expansion of $\text{La}_n(\text{Ti,Fe})_n\text{O}_{3n+2}$ ($n = 5$ and $n = 6$); submitted to: *Acta Crystallogr. B*

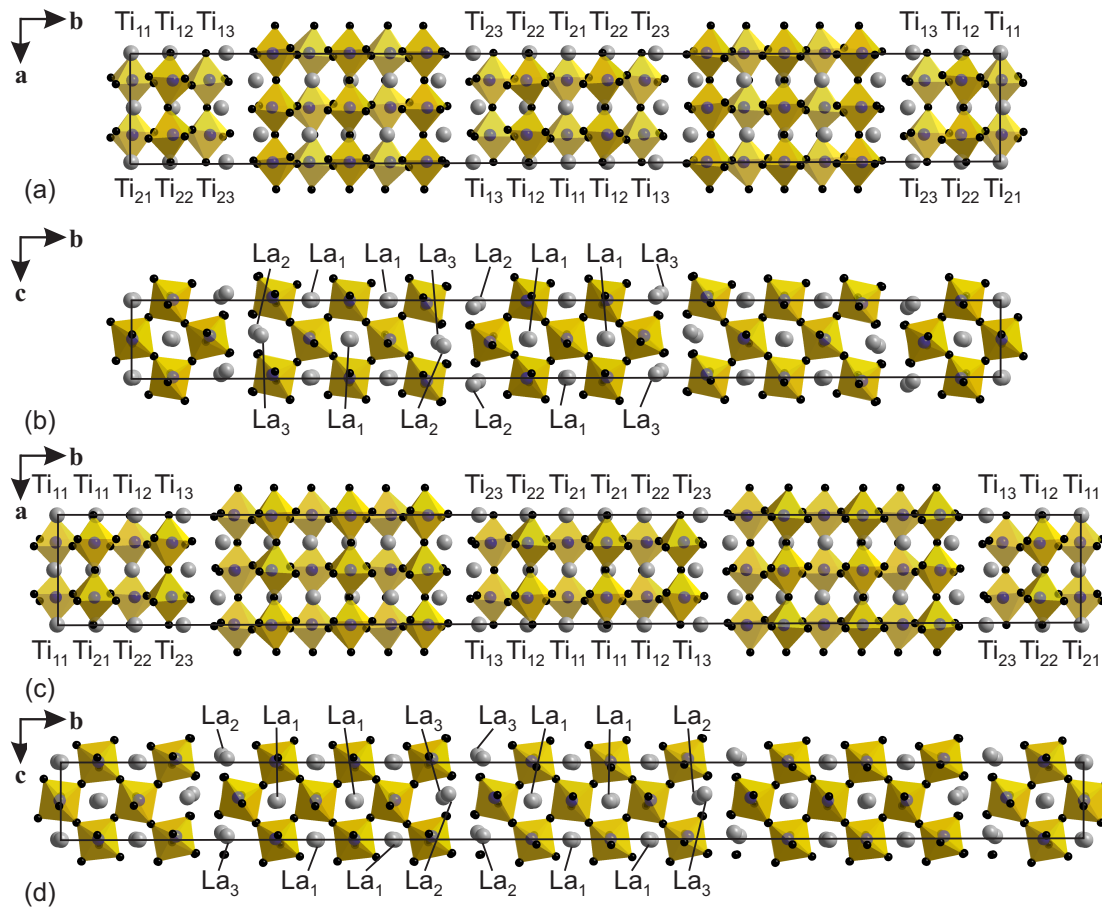


Figure 7.1: Crystal structures of (a), (b) $\text{La}_5(\text{Ti}_{0.8}\text{Fe}_{0.2})_5\text{O}_{17}$ and (c), (d) $\text{La}_6(\text{Ti}_{0.67}\text{Fe}_{0.33})_6\text{O}_{20}$. The pseudo-orthorhombic supercells are indicated by solid lines. Gray circles represent La atoms and $(\text{Ti,Fe})\text{O}_6$ octahedra are outlined. The numbering denotes the crystallographically independent Ti/Fe and La sites in the supercell description.

The homologous series $A_nB_nO_{3n+2}$ includes compounds that are high- T_C ferroelectric compounds, *e.g.* $La_2Ti_2O_7$, $Ca_2Nb_2O_7$, $Sr_2Nb_2O_7$ ($n = 4$) and $Sr_6Nb_4Ti_2O_{20}$ ($n = 6$) (Nanamatsu et al., 1974; Nanamatsu and Kimura, 1974; Nanamatsu et al., 1975; Isupov, 1999). Other compounds, like $La_5Ti_5O_{17}$ and $Sr_5Nb_5O_{17}$, are quasi-one-dimensional metals with their highest conductivities parallel to the layers (Kuntzsch, et al., 2002; 2003). Recently $La_5(Ti_{0.8}Fe_{0.2})_5O_{17}$ and $La_6(Ti_{0.67}Fe_{0.33})_6O_{20}$ have attracted interest because of their magnetic properties. Lichtenberg et al. (2008) have shown that $La_5(Ti_{0.8}Fe_{0.2})_5O_{17}$ is paramagnetic for temperatures within at least 2–390 K, while $La_6(Ti_{0.67}Fe_{0.33})_6O_{20}$ shows a crossover in magnetic behavior at about room temperature, but apparently lacks magnetic order down to at least 2 K.

One possible mechanism for the variation of physical properties is the variation of crystal structures with temperature or pressure. The effects of hydrostatic pressure on the crystal structures of $A_nB_nO_{3n+2}$ have been studied by Loa et al. (2004) for pressures up to 27 GPa for $La_5Ti_5O_{17}$. The compressibility is anisotropic with the largest compressibility along the stacking direction. Loa et al. (2004) also found that the compressibility of a single slabs is of similar magnitudes along all three crystallographic axes, while most of the compression along the stacking direction originates in a reduction of the width of the interslab region. This behavior was explained by the presence of strong T–O bonds within the slabs, while they are missing between the slabs. To our knowledge studies of the thermal expansion of compounds $A_nB_nO_{3n+2}$ are not available in the literature. Here we show that $La_5(Ti_{0.8}Fe_{0.2})_5O_{17}$ and $La_6(Ti_{0.67}Fe_{0.33})_6O_{20}$ exhibit anisotropic thermal expansion within the range of temperatures 90–370 K. Unlike the compressibility of related $La_5Ti_5O_{17}$ (Loa et al., 2004), the largest thermal expansion is found in a direction parallel to the layers. The thermal evolution of the crystal structures shows that the anisotropy of the thermal expansion can be explained by temperature-dependent tilts of the (Ti,Fe) O_6 octahedral groups.

7.2 Experimental

7.2.1 Synthesis

Crystalline rods of compounds $La_n(Ti_{1-x}Fe_x)_nO_{3n+2}$ with nominal compositions $x = 1/5$ for $n = 5$ and $x = 1/3$ for $n = 6$, have been synthesized by floating-zone melting in argon at temperatures between 1100 and 1200 K. The starting materials were

stoichiometric mixtures of La_2O_3 , Fe_2O_3 and TiO_2 . Sample preparation is described by Lichtenberg et al. (2008).

7.2.2 Single-crystal X-ray diffraction

Small parts of the single-crystalline rods of either composition were crushed. Sub-millimeter-sized, metallic gray fragments were glued to glass fibers and tested for crystalline quality by ω scans on a Nonius MACH3 four-circle diffractometer. These tests have shown that the quality of the best crystals is higher for the $n = 5$ samples than for the $n = 6$ samples. For $n = 5$, Bragg reflections showed a full-width at half-maximum (FWHM) of approximately 0.10 deg, similar to the instrumental resolution. For the best crystals of $n = 6$, the FWHM of ω scans were larger than 0.13 deg. The observation of decreasing crystal quality with increasing n is in agreement with the results of Guevarra et al. (2007).

The crystal of highest quality of either compound was selected for temperature-dependent single-crystal X-ray diffraction experiments on a Marresearch MAR345 DTB image-plate diffractometer with Mo- $K\alpha$ radiation from a rotating-anode X-ray generator. Sample temperatures were selected employing an Oxford Cryostream N_2 open-flow cryostat (accuracy of at least 1 K). For both compounds, complete data sets of Bragg reflections were collected at seven temperatures between 90 and 350 K. To increase the effective dynamic range of the data sets, images were measured with three different exposure times of 6, 48 and 384 seconds. Lattice parameters and integrated intensities of the Bragg-reflections were extracted from the measured images by use of EVAL15 (Schreurs et al., 2010); subsequent numerical absorption correction and scaling were applied using SADABS (Sheldrick, 2008). For each data set Bragg reflections measured at different ψ -values were averaged with symmetry equivalent reflections with JANA2006 (Petricek et al., 2006). Experimental details are given in Table 7.1.

The thermal evolution of the lattice parameters was studied for the $n = 5$ compound at 18 different temperatures in the range between 90 and 370 K on a Huber four-circle diffractometer with Mo- $K\alpha$ radiation from a sealed X-ray tube, and equipped with a point-detector. Lattice parameters determined by these measurements agree well with those determined from the image-plate experiments, but they show smaller standard derivations. For structure refinements of $n = 5$, the lattice parameters determined with the four-circle-diffractometer were combined with integrated intensities from the image-plate data.

Table 7.1: Crystal data of $\text{La}_5(\text{Ti}_{0.8}\text{Fe}_{0.2})_5\text{O}_{17}$ and $\text{La}_6(\text{Ti}_{0.67}\text{Fe}_{0.33})_6\text{O}_{20}$ at seven temperatures. For all refinements: non-standard setting $C'2_1/d(\sigma_1\sigma_2)0\bar{1}0$ of superspacegroup No. 14.1-2.1 $P2_1/b(\sigma_1\sigma_2\ 0)00$ (Stokes et al., 2011) with centering vectors $(\frac{1}{2}, 0, 0, \frac{1}{2})$, $(\frac{3}{4}, \frac{1}{2}, 0, \frac{1}{4})$, $(\frac{1}{4}, \frac{1}{2}, 0, \frac{3}{4})$ and symmetry operators $(x_1\ x_2\ x_3\ x_4)$, $(-x_1 -x_2 -x_3 -x_4 + \frac{1}{2})$, $(-x_1 -x_2 + \frac{1}{2}\ x_3 + \frac{1}{2}\ -x_4 + \frac{1}{2})$, $(x_1\ x_2 + \frac{1}{2}\ -x_3 + \frac{1}{2}\ -x_4)$. For $\text{La}_5(\text{Ti}_{0.8}\text{Fe}_{0.2})_5\text{O}_{17}$: $\mathbf{q} = (0\ \frac{1}{12}\ 0)$, $t_0 = 0$, crystal size $0.22 \times 0.05 \times 0.02\ \text{mm}^3$. For $\text{La}_6(\text{Ti}_{0.67}\text{Fe}_{0.33})_6\text{O}_{20}$: $\mathbf{q} = (0\ \frac{1}{14}\ 0)$, $t_0 = \frac{1}{56}$, crystal size $0.12 \times 0.08 \times 0.005\ \text{mm}^3$.

	90 K	150 K	200 K	250 K	295 K	320 K	350 K
Crystal data							
Chemical formula							
Basic structure, a (Å)	7.827 (5)	7.8266 (15)	7.8295 (16)	7.8339 (17)	7.8370 (16)	7.8394 (15)	7.8422 (16)
b (Å)	5.218 (4)	5.2203 (13)	5.2213 (14)	5.2222 (15)	5.2237 (13)	5.2244 (13)	5.2254 (14)
c (Å)	5.537 (3)	5.5404 (11)	5.5418 (12)	5.5444 (13)	5.5459 (12)	5.5468 (11)	5.5484 (12)
γ (°)	90.02 (5)	89.988 (16)	89.994 (17)	90.007 (17)	90.001 (17)	89.997 (16)	89.998 (17)
V (Å ³)	226.1 (3)	226.37 (8)	226.55 (9)	226.82 (10)	227.04 (9)	227.18 (8)	227.37 (9)
D_x (Mg m ⁻³)	5.937	5.931	5.915	5.919	5.913	5.910	5.905
μ (mm ⁻¹)	18.68	18.66	18.61	18.62	18.60	18.59	18.58
Data collection							
T_{\min}/T_{\max}	0.385/0.747	0.390/0.747	0.387/0.747	0.385/0.747	0.382/0.747	0.386/0.747	0.388/0.747
No. of measured, unique and observed reflections ($I > 3\sigma(I)$)	53568, 7093, 6809	50994, 6469, 6210	51050, 6471, 6204	58927, 6510, 6146	50644, 5368, 5074	58267, 6525, 6149	58567, 6517, 6166
R_{int}	0.038	0.038	0.038	0.045	0.042	0.044	0.045

Continued on next page ...

Table 7.1: Continued from previous page

	90 K	140 K	200 K	250 K	295 K	320 K	350 K
<i>hklm</i> range							
<i>h</i>	-13 → 13	-13 → 13	-13 → 13	-13 → 13	-12 → 12	-13 → 13	-13 → 13
<i>k</i>	-8 → 8	-8 → 8	-8 → 8	-8 → 8	-8 → 7	-8 → 8	-8 → 8
<i>l</i>	-9 → 9	-9 → 9	-9 → 9	-9 → 9	-8 → 8	-9 → 9	-9 → 9
<i>m</i>	-5 → 6	-5 → 6	-5 → 6	-5 → 6	-5 → 6	-5 → 6	-5 → 6
θ_{\max} (°)	38.6	36.4	36.4	36.5	33.8	36.5	36.5
$(\sin(\theta/\lambda))_{\max}$ (Å ⁻¹)	0.878	0.835	0.835	0.837	0.782	0.837	0.836
Refinement							
<i>R</i> (obs/all)	0.029/0.031	0.029/0.031	0.029/0.031	0.033/0.036	0.030/0.033	0.029/0.037	0.034/0.037
<i>wR</i> (obs/all)	0.043/0.043	0.043/0.043	0.042/0.042	0.048/0.048	0.042/0.045	0.050/0.050	0.050/0.050
<i>S</i> (obs/all)	2.70/2.66	2.70/2.66	2.63/2.59	2.79/2.72	2.84/2.77	2.91/2.84	2.90/2.83
No. of parameters	147	147	147	146 ²	147	147	147

Continued on next page ...

²Occupancy of Fe13 was fixed to 0, because a free refinement resulted in a small, but negative value, which was zero within the standard uncertainties.

Table 7.1: Continued from previous page

	90 K	140 K	200 K	250 K	295 K	320 K	350 K
Crystal data							
Chemical formula	$\text{La}_6(\text{Ti}_{0.67}\text{Fe}_{0.33})_6\text{O}_{20}$						
Basic structure, a (Å)	7.821 (2)	7.8248 (18)	7.8267 (19)	7.8302 (19)	7.8367 (18)	7.8339 (19)	7.8379 (18)
b (Å)	5.2697 (18)	5.2721 (14)	5.2714 (16)	5.2737 (16)	5.2775 (14)	5.2752 (13)	5.2768 (13)
c (Å)	5.5468 (18)	5.5483 (16)	5.5503 (17)	5.5518 (18)	5.5561 (17)	5.5520 (18)	5.5545 (14)
γ (°)	90.02 (2)	90.007 (17)	90.019 (17)	90.001 (18)	90.044 (17)	89.990 (16)	89.996 (17)
V (Å ³)	228.62 (11)	228.88 (10)	228.99 (11)	229.26 (12)	229.79 (11)	229.44 (10)	229.73 (10)
D_x (Mg m ⁻³)	6.011	6.004	6.001	5.995	5.981	5.990	5.982
μ (mm ⁻¹)	18.96	18.94	18.93	18.91	18.86	18.89	18.87
Data collection							
T_{\min}/T_{\max}	0.330/0.748	0.338/0.748	0.341/0.748	0.343/0.748	0.367/0.748	0.353/0.748	0.349/0.748
No. of measured, unique and observed reflections ($I > 3\sigma(I)$)	48590, 12253, 11223	55250, 12312, 11441	56173, 12184, 11268	56192, 12311, 11385	37403, 12067, 11548	52264, 11906, 10996	56062, 12281, 11137
R_{int}	0.055	0.048	0.048	0.047	0.041	0.046	0.048

Continued on next page ...

7.2.3 Structure refinements in (3+1)-dimensional superspace

Superstructures can be described as commensurately modulated structures within the superspace approach (Janssen et al., 2006; van Smaalen, 2007). Perez-Mato et al. (1999) has demonstrated that the superspace formalism can be used for the description of all members of a homologous series as commensurately modulated structures by a unified structure model, where the modulation wave vector \mathbf{q} and the modulation functions depend on n in a systematic way. For the series $A_nB_nO_{3n+2}$, Elcoro et al. (2004) have proposed a model for the superspace description of $\text{NaCa}_4\text{Nb}_5\text{O}_{17}$, which was adapted by Guevarra et al. (2007) to the $n = 5$ and $n = 6$ compounds $\text{Ca}_n(\text{Nb,Ti})_n\text{O}_{3n+2}$. The latter superspace models directly apply to $\text{La}_5(\text{Ti}_{0.8}\text{Fe}_{0.2})_5\text{O}_{17}$ ($n = 5$) and $\text{La}_6(\text{Ti}_{0.67}\text{Fe}_{0.33})_6\text{O}_{20}$ ($n = 6$), where La replaces Ca, Ti replaces Nb and Fe replaces Ti.

Structure refinements were performed with JANA2006 and followed the procedure of Guevarra et al. (2007). All structure refinements converged smoothly towards a good fit to the diffraction data as indicated by low R-values (Table 7.1). R-values for $\text{La}_6(\text{Ti}_{0.67}\text{Fe}_{0.33})_6\text{O}_{20}$ higher than those for $\text{La}_5(\text{Ti}_{0.8}\text{Fe}_{0.2})_5\text{O}_{17}$, are explained by the lower crystal quality of $n = 6$, probably resulting from stacking faults or other defects. They initiated attempts to improve the quality of the structure models of $n = 6$ by the introduction of additional modulation parameters of higher order. However, all additional refinements did not lead to significant non-zero values of the additional parameters nor to improved R-values. Other extended models, *e.g.* the use of anharmonic ADPs, failed to significantly lower the R-values, but led to unphysical probability densities. Furthermore these refinements suffered from high correlations between parameters and convergence problems. Therefore, we have taken as final models those superspace models involving harmonic ADPs (Table 7.1). For the analysis of the structural properties, the superspace structure models were transformed into superstructures (Fig. 7.1).

7.3 Results and discussion

7.3.1 Crystal structures

The crystal structures of $\text{La}_5(\text{Ti}_{0.8}\text{Fe}_{0.2})_5\text{O}_{17}$ ($n = 5$) and $\text{La}_6(\text{Ti}_{0.67}\text{Fe}_{0.33})_6\text{O}_{20}$ ($n = 6$) are only weakly dependent on temperature. Apart from a general contraction upon cooling, the major changes can be characterized as a variation of the tilt of

the BO_6 octahedra with temperature. They are responsible for the anisotropy of the thermal expansion, as discussed in Section 7.3.2. Other structural features, like the distribution of titanium and iron within the compounds, hardly depend on temperature. They are in agreement with the structural features of related compounds $\text{A}_n\text{B}_n\text{O}_{3n+2}$, as it is discussed below (Elcoro et al., 2004; Daniels et al., 2002; Zuniga and Darriet, 2003; Guevarra et al., 2005b; 2007).

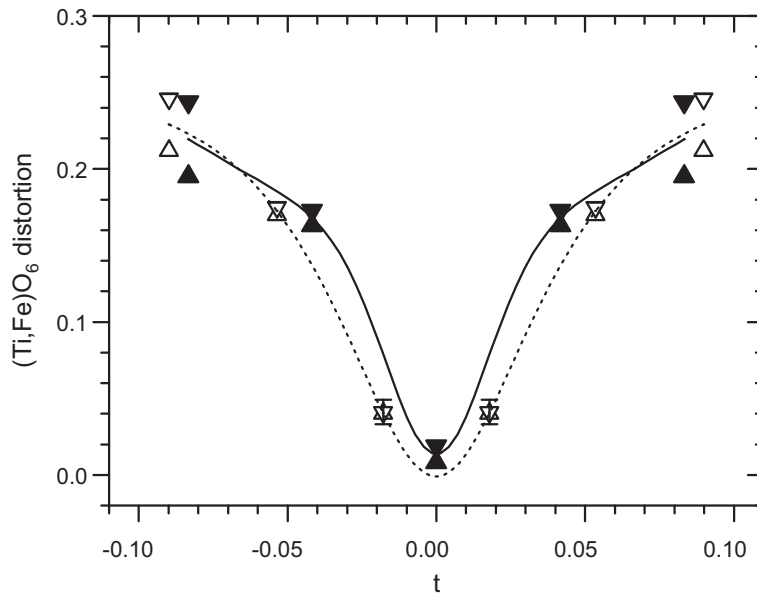


Figure 7.2: Polyhedron distortions of $(\text{Ti,Fe})\text{O}_6$ octahedra as a function of t , where $t = 0$ refers to the centers of the slabs. Filled triangles and the solid line correspond to $\text{La}_5(\text{Ti}_{0.8}\text{Fe}_{0.2})_5\text{O}_{17}$; open triangles and the dotted line refer to $\text{La}_6(\text{Ti}_{0.67}\text{Fe}_{0.33})_6\text{O}_{20}$. Triangles pointing up represent distortions of octahedra in one row along \mathbf{b} , while the triangles pointing down refer to distortions of octahedra in the second rows. Error bars represent the spread of values for variation of temperature. They are smaller than the sizes of the symbols, if error bars are not shown.

The distortion of the octahedral coordination polyhedra $(\text{Ti,Fe})\text{O}_6$ can be characterized by the values of the lengths of the six $(\text{Ti,Fe})\text{--O}$ bonds in each octahedron. The spread in bond lengths around a single metal atom decreases from the rim to the center of a slab (See supplementary material), in perfect agreement with the variation of bond lengths in $\text{Ca}_5(\text{Nb}_{0.8}\text{Ti}_{0.2})_5\text{O}_{17}$ and $\text{Ca}_6(\text{Nb}_{0.67}\text{Ti}_{0.33})_6\text{O}_{20}$ (Guevarra et al., 2007). A measure for the variation of bond lengths is the distortion

index (Lichtenberg et al., 2008),

$$\text{polyhedron distortion} = \frac{\max(d[\text{B-O}]) - \min(d[\text{B-O}])}{\text{ave}(d[\text{B-O}])}, \quad (7.1)$$

which is largest at the borders and smallest in the middle of the slabs (Fig. 7.2), again in agreement with $\text{Ca}_n(\text{Nb}_{1-x}\text{Ti}_x)_n\text{O}_{2n+3}$ and other $n = 5, 6$ compounds (Daniels et al., 2002; Zuniga and Darriet, 2003; Guevarra et al., 2005b; 2007). The dependence of the octahedral distortion on the location within the slabs is a general feature of $\text{A}_n\text{B}_n\text{O}_{3n+2}$ compounds. It reflects the flexibility of the structures in the interslab regions.

The 14 structure models indicate a preferential occupancy of Fe^{3+} at sites near the centers of the slabs, while the octahedra at the borders are almost exclusively occupied by Ti^{4+} (Fig. 7.3). This implies that Ti^{4+} is located at the centers of the most distorted octahedra, in contrast with the compounds $\text{Ca}_n(\text{Nb}_{1-x}\text{Ti}_x)_n\text{O}_{3n+2}$ ($n = 5$ and $n = 6$) and $\text{Sr}_5(\text{Nb}_{0.8}\text{Ti}_{0.2})_5\text{O}_{3n+2}$, where Ti^{4+} is accommodated in the least distorted octahedra (Drews et al., 1996; Guevarra et al., 2005b; 2007). Previously, the preference of Ti^{4+} for less distorted environments was assumed to be a driving force for the chemical order. A comparison of the present crystal structures with those published unequivocally shows that the valence of the ions is the driving force for chemical order. In all compounds, the sites at the borders of the slabs are fully occupied by the ion of highest valence. Since the interslab regions accommodate the excess of oxygen ions, local charge compensation appears to be the major factor in determining the chemical order in these compounds. This interpretation is in agreement with the local charge compensation observed for $\text{NaCa}_4\text{Nb}_5\text{O}_{17}$ ($n = 5$) (Zuniga and Darriet, 2003).

The consequences of the different concentrations of the magnetic ions Fe^{3+} for the understanding of different magnetic behaviors of $n = 5$ and $n = 6$ will be discussed elsewhere (Wölfel et al., 2012).

The atomic valences of Ti and Fe have been calculated by the Bond-Valence Method (Brown, 2002). Ti^{4+} appears underbonded at most sites and Fe^{3+} appears overbonded with respect to the formal valences [Fig. 7.4(a)]. This behavior is explained by the fact that the structure models provide positions of oxygen atoms that are the average of oxygen positions for TiO_6 and oxygen positions for FeO_6 octahedra.

Apparently, Fe^{3+} requires a more relaxed environment than Ti^{4+} does, in order to arrive at the expected values for their valences, in agreement with the ionic sizes

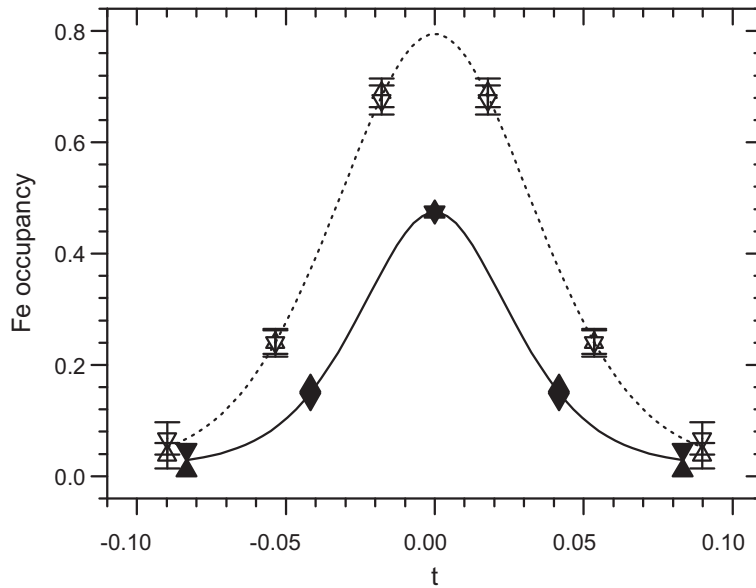


Figure 7.3: Fraction of (Ti,Fe) sites that is occupied by Fe^{3+} as a function of t , where $t = 0$ refers to the centers of the slabs. Symbols and curves have similar meanings as in Fig. 7.2.

of 0.645 \AA for Fe^{3+} and 0.605 \AA for Ti^{4+} (Shannon, 1976). This interpretation is supported by the dependence of the valences on the site occupancies of the two atomic species. At the borders of the slabs, sites are fully occupied by Ti and the computed valences of Ti are nearly equal to the formal valence of four. The large differences between formal and computed valence of Fe at these sites is without consequence, because these sites do not contain Fe [Figs. 7.3 and 7.4(a)]. Sites fully occupied by Fe are not available, but a linear fit to the calculated valences results in an extrapolated value of 3.1 for Fe at fully occupied sites, close to the formal valence of three [Fig. 7.4(b)].

Figure 7.4(b) demonstrates that the refined oxygen positions indeed represent the average of oxygen positions in TiO_6 and FeO_6 octahedra weighted according to the occupancies by Ti and Fe, respectively. At the same time, the observed dependence of valence on occupational fraction demonstrates the power and sensitivity of the Bond-Valence method.

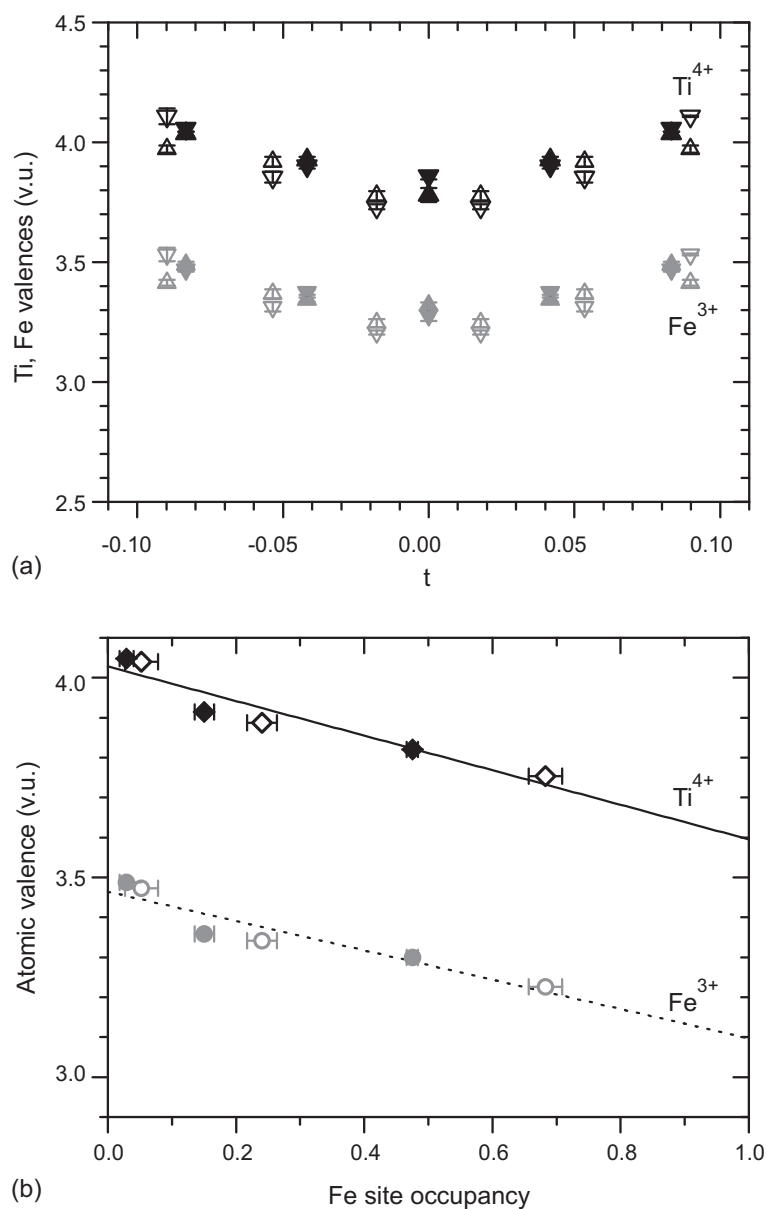


Figure 7.4: (a) Atomic valences of Ti and Fe as a function of t , where $t = 0$ refers to the centers of the slabs. (b) Atomic valences as a function of the site occupancy by Fe. Symbols have similar meanings as in Fig. 7.2. Lines are linear fits to the data, resulting in extrapolated values of $V[\text{Ti}] = 4.03(2)$ for pure Ti sites, and $V[\text{Fe}] = 3.10$ for pure Fe sites. Atomic valences have been computed with parameters $R_0(\text{Ti-O}) = 1.815 \text{ \AA}$, $R_0(\text{Fe-O}) = 1.759 \text{ \AA}$ and $b = 0.37 \text{ \AA}$ (Brese and O'Keeffe, 1991).

Table 7.2: Thermal expansion coefficients. The volume (α_V) and linear thermal expansion coefficients along the three lattice directions (α_a , α_b and α_c) as well as the expansion coefficients for the thicknesses of the slabs (d_1) and interslab regions (d_2) have been obtained by a linear fit to the measured data in the interval T_1 – T_2 for $n = 5$ and $n = 6$. (compare to Figs. 7.5 and 7.8).

z	$n = 5$		$n = 6$	
	T_1 – T_2 (K)	$\alpha_z \times 10^5$ (K ⁻¹)	T_1 – T_2 (K)	$\alpha_z \times 10^5$ (K ⁻¹)
V	175–370	2.43 (7)	90–350	1.70 (14)
V			200–350	1.94 (30)
a	175–370	1.09 (2)	90–350	0.76 (6)
b	90–370	0.52 (2)	90–350	0.48 (6)
c	90–370	0.80 (2)	90–350	0.45 (6)
d_1	90–350	0.78 (3)	90–350	0.65 (6)
d_2	90–350	–0.1 (8)	90–350	–0.1 (2)

7.3.2 Thermal expansion

Lattice parameters depend smoothly on temperature with the exception of the values of $n = 6$ at 295 K. We believe the latter values to be inaccurate, and they have not been considered in the analysis presented here.

The thermal expansion α_V has comparable values for the compounds $n = 5$ and $n = 6$ [Fig. 7.5(c) and Table 7.2]. The same is true for the anisotropy of the thermal expansion, exemplified by the linear thermal expansion coefficients along the three basis vectors of the unit cell (Table 7.2).

Standard uncertainties of the lattice parameters reflect the accuracy of these parameters at each single temperature. The relative accuracies of these parameters at different temperatures are higher, because misalignments and other instrumental properties do not change during a temperature-dependent experiment. This feature explains the temperature dependence of the lattice parameters, which is much more smooth than expected on the basis of the experimental standard uncertainties [Figs. 7.5(a) and 7.5(b)]. This argument applies more strict to the data for $n = 5$ than to the data for $n = 6$, because the poorer crystal quality of the latter has detrimental influences on the accuracies of reflection positions from which lattice parameters are computed.

According to these considerations, a clear deviation from linear behavior is ob-

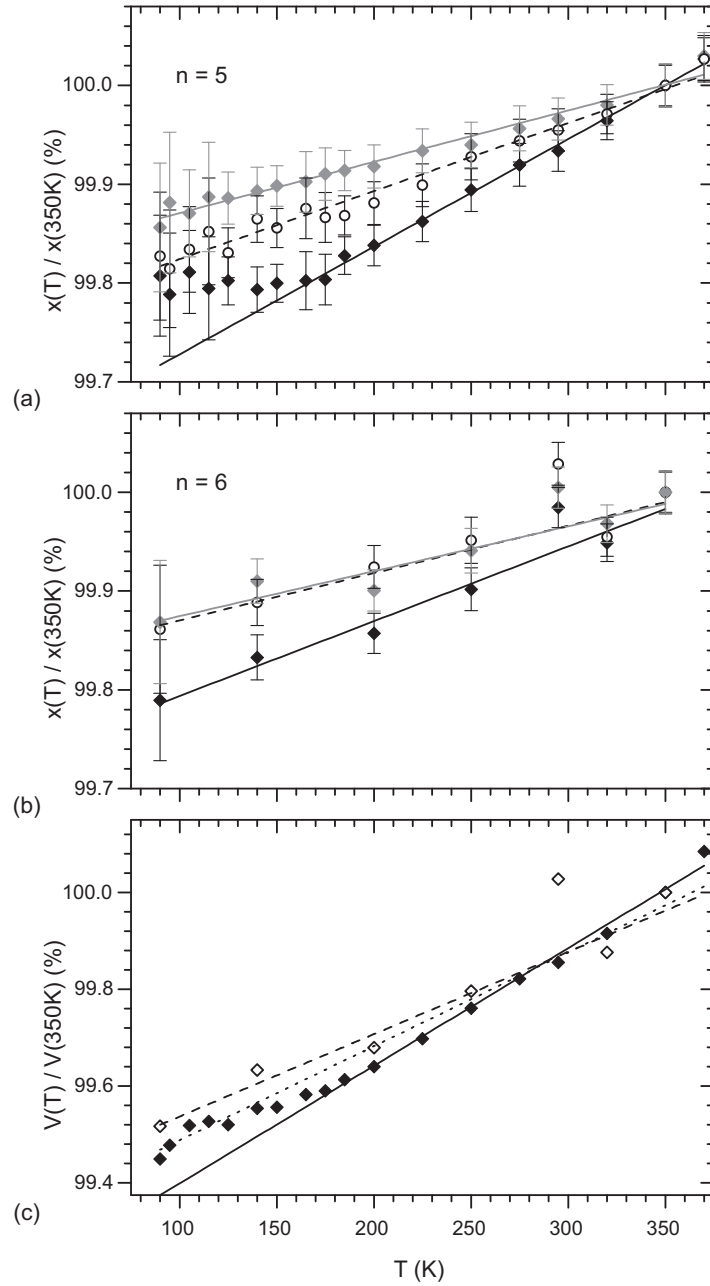


Figure 7.5: Temperature dependence of the lattice parameters of (a) $\text{La}_5(\text{Ti}_{0.8}\text{Fe}_{0.2})_5\text{O}_{17}$ ($n = 5$), (b) $\text{La}_6(\text{Ti}_{0.67}\text{Fe}_{0.33})_6\text{O}_{20}$ ($n = 6$), and (c) the volume of the unit cell of $n = 5$ (filled diamonds) and $n = 6$ (open diamonds; dashed line for full-range fit, dotted line for fit to 200-350 K data). Displayed is the relative change with respect to the values at $T = 350$ K. In (a) and (b) black diamonds stand for a , gray diamonds refer to b , and circles reflect values of c . Lines are a linear fit to the data points according to Table 7.2.

served for the lattice parameter a of $n = 5$ below $T \approx 175$ K, where a appears to be nearly constant down to the lowest measured temperature of 90 K [Fig. 7.5(a)]. Data for $n = 6$ are too sparse and too inaccurate, in order to draw any conclusions in this respect, but they are certainly not at variance with such a behavior [Fig. 7.5(b)]. Any deviation from linear behavior cannot be established for the other two lattice parameters of both compounds within their experimental accuracies. The non-linear behavior of a is reflected in a non-linear decrease of the unit-cell volumes below $T \approx 175$ K [Fig. 7.5(c)].

A second feature of the experimental data is the anisotropy of the thermal expansion. Above ~ 175 K, the largest linear thermal expansion is along the a axes, which is a direction parallel to the slabs. This finding is in contrast with the anisotropic compressibility of the $n = 5$ type compound $\text{La}_5\text{Ti}_5\text{O}_{17}$, which has been found to be largest in the direction perpendicular to the layers (Loa et al., 2004). It may be compared to other layered compounds, which may show a much higher expansion perpendicular to the layers (graphite)³ or which may show nearly isotropic expansion (WSe_2)⁴ (Bailey and Yates, 1970; Murray and Evans, 1979).

One reason for the observed thermal behavior is that $\text{A}_n\text{B}_n\text{O}_{3n+2}$ compounds are not layered compounds in a classical sense, where slabs would interact via weak Van der Waals forces. All $\text{A}_n\text{B}_n\text{O}_{3n+2}$ compounds include A cations between the layers, which are responsible for strong chemical bonds across the interlayer gap. However, both the crossover in behavior at $T = 175$ K and the observed anisotropy are explained by the thermal evolution of the crystal structures, as it is demonstrated below (Section 7.3.3).

7.3.3 Octahedral tiltings

Several structural features do not depend on temperature, including the distribution of Ti/Fe cations and the distortions of the octahedral groups (Section 7.3.1). Apart from distortions, the octahedral groups are tilted with respect to an arrangement aligned with the coordinate axes, as it is found in the perovskite structure type (Fig.

³Graphite anisotropic thermal expansion at LT (20-270K) show a small negative expansion parallel to the layers (called the perpendicular direction) and a large, positive expansion perpendicular to the layers (called the parallel directions; parallel to the stacking axis).

⁴2H-MoS₂ and 2H-WSe₂ lattice parameters $a=b$ and c of the hexagonal lattices of these two compounds in dependence on temperature (10-320K). The values are not very accurate, but they do show the anisotropic nature of the expansion, that is higher along c , i.e. in the direction perpendicular to the layers.

7.6). The tilting is mainly about **a** ($\delta_a \approx 10.5$ deg) and about **b** ($\delta_b \approx 8.5$ deg), while the tilt about **c** is small and independent from temperature ($\delta_c = 0.9$ deg). Different tilts of octahedral groups determine different shapes of coordination polyhedra of the La cations, with larger tilts corresponding to smaller volumes of the LaO_{12} and LaO_{13} polyhedra.

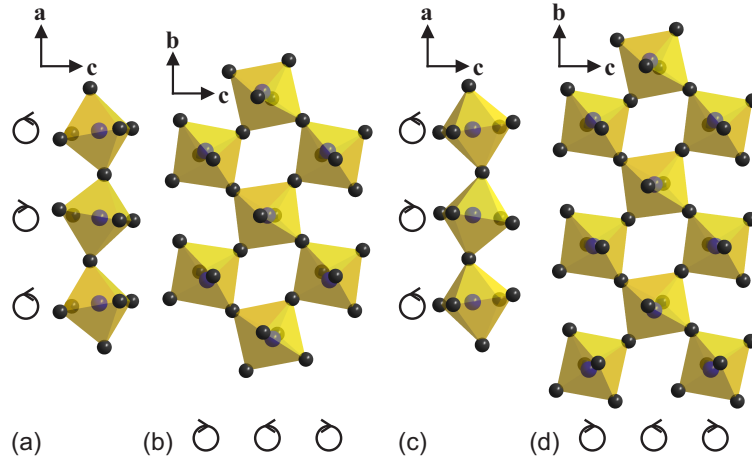


Figure 7.6: Projections of the crystal structures at 90 K, showing tiltings of $(\text{Ti,Fe})\text{O}_6$ octahedral groups in (a), (b) $\text{La}_5(\text{Ti}_{0.8}\text{Fe}_{0.2})_5\text{O}_{17}$ and (c), (d) $\text{La}_6(\text{Ti}_{0.70}\text{Fe}_{0.30})_6\text{O}_{20}$. The sense of the tilt is indicated.

A larger tilt, for example, about **b** implies shorter **a** and **c** axes. Accordingly, the anisotropy of the thermal expansion can be explained by the temperature dependence of the tilts. On increasing temperature from 150 to 350 K, the tilt angles about **b** decrease by 0.8 deg and thus explain the relatively large expansions along **a** in both compounds (Fig. 7.6). The tilts about **b** at 90 K are nearly equal or smaller than at 150 K, thus explaining the departure from linearity of the temperature dependence of the *a* axis in $n = 5$ (compare to Fig. 7.5). The increase of *c* on heating is partly compensated by a concomitant decrease of the inter slab region (see below). The expansion along **b** is considerably smaller than the expansion along **a**, because the thermal variation of the tilt about **a** is much smaller than the thermal variation of the tilt about **b** (Fig. 7.7).

This mechanism of the thermal expansion is corroborated by consideration of the thicknesses (d_1) of the slabs and the width (d_2) of the interslab regions [compare to Loa et al. (2004)]. All of the thermal expansion along **c** can be assigned to an expansion of the slabs, while the width of the interslab regions is independent from temperature within the experimental accuracy (Fig. 7.8).

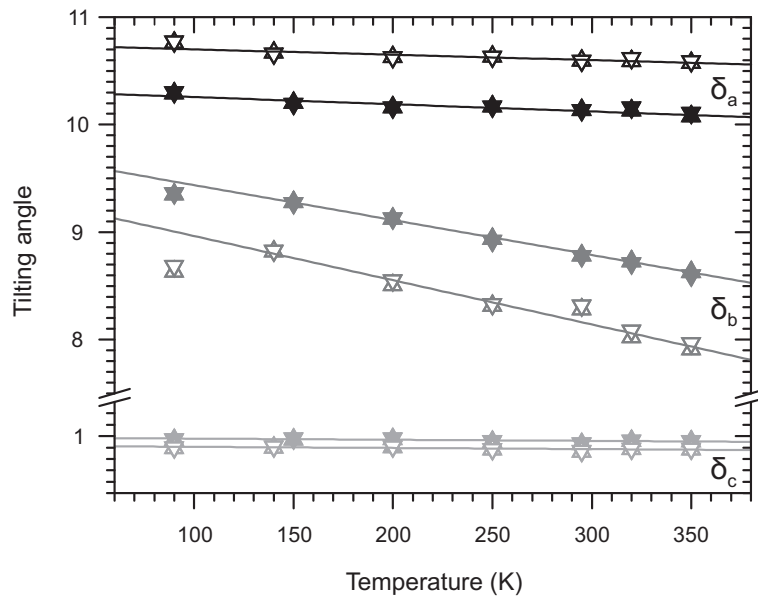


Figure 7.7: Temperature dependence of the tilting angles δ_a (black), δ_b (dark gray) and δ_c (light gray) of selected octahedra in $\text{La}_5(\text{Ti}_{0.8}\text{Fe}_{0.2})_5\text{O}_{17}$ (filled symbols) and $\text{La}_6(\text{Ti}_{0.67}\text{Fe}_{0.33})_6\text{O}_{20}$ (open symbols). Triangles pointing up represent tilting angles of octahedra in one **b-c**-layer, while the triangles pointing down refer to octahedra tiltings in a second layer displaced by $\mathbf{a}/2$. The lines are linear fits to the data. The data points for 90 K are excluded from the fit, because they deviate from the linear behavior for δ_b .

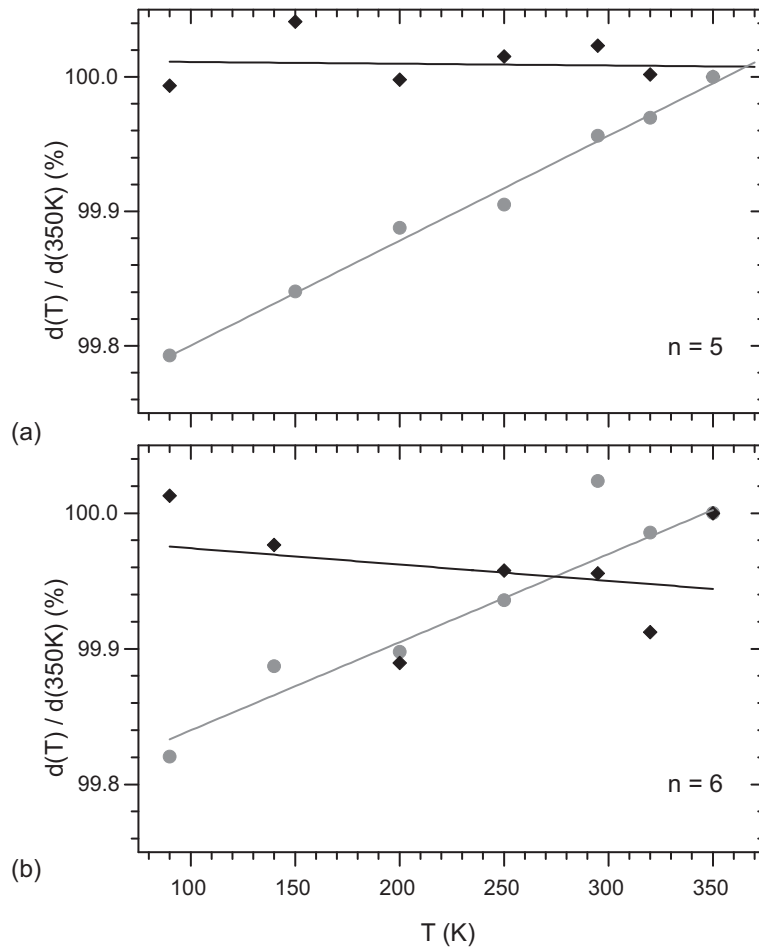


Figure 7.8: Temperature dependence of the thicknesses of the slabs (d_1 ; gray circles) and the interslab regions (d_2 ; black diamonds) relative to the values at 350 K of (a) $\text{La}_5(\text{Ti}_{0.8}\text{Fe}_{0.2})_5\text{O}_{17}$ ($n = 5$) and (b) $\text{La}_6(\text{Ti}_{0.67}\text{Fe}_{0.33})_6\text{O}_{20}$ ($n = 6$). Lines are a linear fit to the data points according to Table 7.2.

7.4 Conclusions

The crystal structures of $\text{La}_5(\text{Ti}_{0.8}\text{Fe}_{0.2})_5\text{O}_{17}$ ($n = 5$) and $\text{La}_6(\text{Ti}_{0.67}\text{Fe}_{0.33})_6\text{O}_{20}$ ($n = 6$) have been determined at seven temperatures between 90 and 350 K. They have revealed a temperature-independent, partial chemical order of Ti/Fe over the B sites of $\text{A}_n\text{B}_n\text{O}_{3n+2}$, with iron concentrated towards the centers of the slabs. A comparison with chemical order in other compounds $\text{A}_n\text{B}_n\text{O}_{3n+2}$ has shown that local charge compensation is the driving force for chemical order, where the highest-valent cation goes to sites near the oxygen-rich borders of the slabs (Drews et al., 1996; Guevarra et al., 2005b; 2007).

Octahedral distortions are found to increase from the centers to the borders of the slabs. They are independent from temperature in very good approximation. Since they appear not to be related to the nature or valence of the cation that resides at their centers, the distortions are likely the result of resolving internal stress between neighboring slabs. Indeed, consideration of the computed valences of Ti and Fe in dependence on the occupational fraction of the site by Fe suggests that the oxygen environment and valence of Fe are that of Fe^{3+} and the oxygen environment and valence of Ti are that of Ti^{4+} , irrespective of the location of the metal ion within the structure [Fig. 7.4(b)].

The thermal expansions of $n = 5$ and $n = 6$ have been determined for temperatures between 90 and 370 K. Thermal expansion is found to be anisotropic with the largest value along a direction parallel to the slabs. This behaviour is at variance with the anisotropy of the compressibility of related $\text{La}_5\text{Ti}_5\text{O}_{17}$, which is largest in the direction perpendicular to the slabs (Loa et al., 2004).

The origin of the anisotropy of the thermal expansion is found to be the temperature dependence of tilts of the octahedral $(\text{Ti,Fe})\text{O}_6$ groups. It is likely that the same mechanism will determine similar anisotropic thermal expansion in other compounds $\text{A}_n\text{B}_n\text{O}_{3n+2}$. While pressure compresses the interslab regions more than the slabs, the effect of temperature is the opposite, with a clear thermal expansion of the width of the slabs and a width of the interslab region that is independent from temperature.

Chapter 8

Two-dimensional magnetic clusters in $\text{La}_n(\text{Ti}_{1-x}\text{Fe}_x)_n\text{O}_{3n+2}$ ($n = 5$ with $x = 0.2$ and $n = 6$ with $x = 0.33$)¹

8.1 Introduction

The layered perovskite-related compounds $\text{A}_n\text{B}_n\text{O}_{3n+2}$, where A is an alkaline earth or rare earth element, B is a transition metal and $2 \leq n \leq 6$, display a wide range of physical phenomena in dependence on their chemical composition (Lichtenberg et al., 2001; 2008). The compounds $\text{La}_2\text{Ti}_2\text{O}_7$, $\text{Ca}_2\text{Nb}_2\text{O}_7$, and $\text{Sr}_2\text{Nb}_2\text{O}_7$ ($n = 4$) are high- T_C ferroelectric compounds, with Curie temperatures T_C above 1615 K (Nanmatsu et al., 1975; Nanamatsu and Kimura, 1974; Nanamatsu et al., 1974). The $n = 4$ compounds are pure-valence compounds comprising La^{3+} and Ti^{4+} or Ca^{2+} and Nb^{5+} . Compounds with $n > 4$ have a mixed-valence character. For example, $\text{Sr}_5\text{Nb}_5\text{O}_{17}$ ($n = 5$) has an average valence of niobium of 4.8+. The 0.2 valence electrons per niobium atom are located in the quasi-one-dimensional (1D) valence band, and are thus responsible for the low-dimensional electronic properties and metal-to-semiconductor phase transition of this compound (Kuntscher et al., 2002). Substitutions can restore the insulating character. For example, the $\text{Ca}_n(\text{Nb}_{1-x}\text{Ti}_x)_n\text{O}_{3n+2}$ are pure-valence compounds composed of Ca^{2+} , Nb^{5+} and Ti^{4+} if the composition is $x = 0.2$ for $n = 5$ or $x = 1/3$ for $n = 6$. These compositions are close to the experi-

¹This chapter has been published as: Wölfel, A., Lichtenberg, F. and van Smaalen, S.: Two-dimensional magnetic clusters in $\text{La}_n(\text{Ti}_{1-x}\text{Fe}_x)_n\text{O}_{3n+2}$ ($n = 5$ with $x = 0.2$ and $n = 6$ with $x = 0.33$); *J. Phys. : Condens. Matter*, **25**: 076003 (2013)

mentally determined compositions of single crystals of these compounds (Guevarra et al., 2007).

The compounds $A_nB_nO_{3n+2}$ may have technical applications because of their dielectric, electrical or magnetic properties. Ceramics of insulating $n = 5$ compounds, like $\text{Ca}_5(\text{Nb}_{0.8}\text{Ti}_{0.2})_5\text{O}_{17}$, $\text{Sr}_5(\text{Nb}_{0.8}\text{Ti}_{0.2})_5\text{O}_{17}$ and $(\text{La}_{0.8}\text{Ca}_{0.2})_5\text{Ti}_5\text{O}_{17}$, have been discussed for possible applications in dielectric resonators at microwave frequencies (Jawahar et al., 2002; Sebastian and Jantunen, 2008; Manan et al., 2011). Conducting, single-crystalline $n = 5$ compounds, like $\text{Ca}_5\text{Nb}_5\text{O}_{17}$, have been investigated in view of applications in resistive memory switching (Koval et al., 2011). Recently, it was proposed that multiferroic compounds could form, if B-site cations are substituted by magnetic elements like iron (Lichtenberg et al., 2008; Titov et al., 2005a). Single-crystals of insulating $\text{La}_n(\text{Ti}_{1-x}\text{Fe}_x)_n\text{O}_{3n+2}$ have been grown for $n = 5$ with nominal composition $x = 0.2$ and for $n = 6$ with nominal composition $x = 1/3$. Although the magnetic susceptibilities indicated strong ferromagnetic interactions at high temperatures in $n = 6$, both compounds failed to develop long-range magnetic order at low temperatures (Lichtenberg et al., 2008). Specifically, $n = 6$ is paramagnetic at all temperatures but with a crossover from strong ferromagnetic coupling at high temperatures to predominantly antiferromagnetic coupling below room temperature.

Here, we report the crystal structures of $\text{La}_n(\text{Ti}_{1-x}\text{Fe}_x)_n\text{O}_{3n+2}$ ($n = 5$ and 6). The partial order of iron over the crystallographically independent B sites provides an explanation for the failure to develop long-range magnetic order. Instead, we propose that the $n = 6$ compound develops two-dimensional ferromagnetic clusters at low temperatures, while $n = 5$ remains paramagnetic, because the concentration of magnetic ions is much smaller in $n = 5$ than in $n = 6$.

8.2 Experimental

Crystalline rods of compositions $\text{La}_5(\text{Ti}_{0.8}\text{Fe}_{0.2})_5\text{O}_{17}$ ($n = 5$) and $\text{La}_6(\text{Ti}_{0.67}\text{Fe}_{0.33})_6\text{O}_{20}$ ($n = 6$) were grown by floating-zone melting as described elsewhere (Lichtenberg et al., 2008). Small fragments of each rod were selected for X-ray diffraction experiments on a Marresearch MAR345dtb image-plate diffractometer with Mo-K α radiation from a rotating-anode. For both compounds complete data collections up to resolutions of $[\sin(\theta)/\lambda]_{\max} = 0.89 \text{ \AA}^{-1}$ were measured at seven different temperatures between $T = 90$ and 350 K, employing an Oxford Cryostream open-flow

cryostat to select the sample temperatures. The software EVAL15 (Schreurs et al., 2010) was used to extract lattice parameters and integrated intensities of Bragg reflections from the measured images. Scaling and absorption correction were applied by the software SADABS (version 2008/1) (Sheldrick, 2008), resulting in a total of 14 data sets of integrated intensities of Bragg reflections.

Structure refinements were performed within the superspace formalism (Elcoro et al., 2004; van Smaalen, 2007), employing the models of $\text{Ca}_n(\text{Nb,Ti})_n\text{O}_{3n+2}$ ($n = 5, 6$) as start models, where La replaces Ca, Ti replaces Nb and Fe replaces Ti (Guevarra et al., 2007). Refinements with JANA2006 (Petricek et al., 2006) converged smoothly towards a good fit to the diffraction data with $R_F(\text{obs}) = 0.034$ for $n = 5$ and $R_F(\text{obs}) = 0.062$ for $n = 6$ at $T = 320 \text{ K}$.² The larger R_F values for $n = 6$ are explained by the lower crystal quality of the compound with higher n , in agreement with an earlier study on $\text{Ca}_n(\text{Nb,Ti})_n\text{O}_{3n+2}$ ($n = 5, 6$) (Guevarra et al., 2007). The lower crystal quality was confirmed by so-called ω scans of Bragg reflections in single-crystal X-ray diffraction of several fragments of the crystalline rods, which were all broader in the case of $n = 6$ than for $n = 5$.

8.3 Structural features

The crystal structures of compounds $\text{A}_n\text{B}_n\text{O}_{3n+2}$ consist of slabs with the perovskite structure type of n octahedra BO_6 wide (figure 8.1). The symmetry is orthorhombic $Immm$ (n is odd) or $Cmcm$ (n is even) with lattice parameters $a_o = a_c$, $b_o = (n + 1)\sqrt{2}a_c$ and $c_o = \sqrt{2}a_c$, where $a_c \approx 3.9 \text{ \AA}$ is the lattice parameter of cubic perovskite (Levin and Bendersky, 1999). These centrosymmetric orthorhombic structures can be found at high-temperatures (Nanamatsu et al., 1975; 1974; Nanamatsu and Kimura, 1974), or they are hypothetical high symmetry structures for other compounds.

The true crystal structures involve octahedral tilting, as it is allowed through lowering of both point symmetry and translational symmetry (Levin and Bendersky, 1999). $\text{Sr}_2\text{Nb}_2\text{O}_7$ ($n = 4$) is incommensurately modulated with acentric orthorhombic symmetry (Daniels et al., 2002). Other compounds have monoclinic symmetries on a fourfold superlattice. The primitive monoclinic unit cells are obtained

²Fits of similar quality were obtained for the data measured at other temperatures. Details of the structure refinements and a discussion of the thermal expansion of $n = 5$ and 6 will be presented elsewhere.

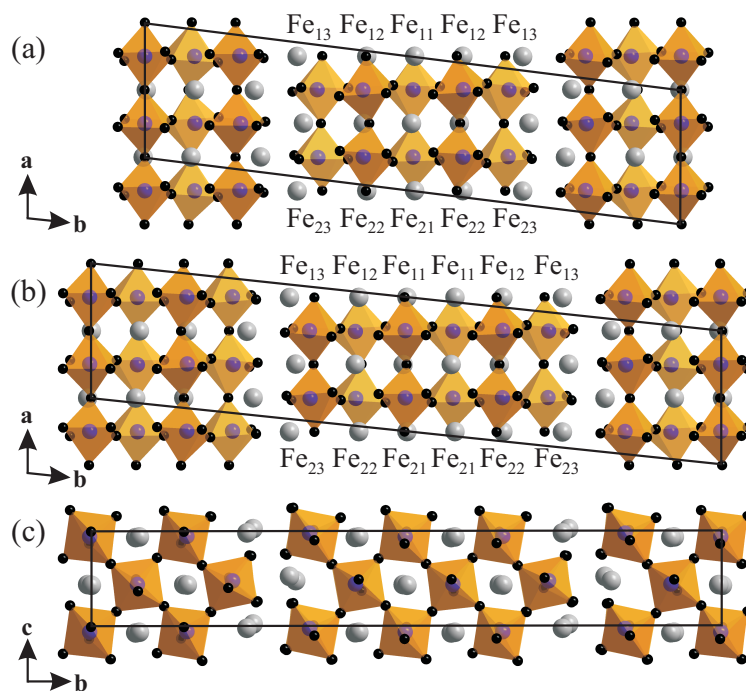


Figure 8.1: The crystal structures of (a) $\text{La}_5(\text{Ti}_{0.8}\text{Fe}_{0.2})_5\text{O}_{17}$ ($n = 5$) and (b), (c) $\text{La}_6(\text{Ti}_{0.67}\text{Fe}_{0.33})_6\text{O}_{20}$ ($n = 6$). The monoclinic unit cells are indicated by lines. Circles represent La atoms, while $(\text{Ti,Fe})\text{O}_6$ octahedra are outlined. The numbering denotes the crystallographically independent Ti/Fe sites.

from the centered orthorhombic unit cells as $\mathbf{a}_m = 2\mathbf{a}_o$, $\mathbf{b}_m = \mathbf{a}_o + \mathbf{b}_o$ and $\mathbf{c}_m = \mathbf{c}_o$. Crystal structures with these lattices have been found for several $n = 5$ and $n = 6$ compounds (figure 8.1) (Guevarra et al., 2007; 2005a). The space groups were established as $P2_1/b$ (c unique) for $n = 5$ and $P2_1$ (c unique) for $n = 6$. The superlattice reflections pertaining to the doubling of \mathbf{a} are weak. Apparently, they have been overlooked in several reports on the crystal structures of the compounds $A_nB_nO_{3n+2}$ (Titov et al., 2005a;b; Drews et al., 1996; Abrahams et al., 1998). Here, $\text{La}_n(\text{Ti}_{1-x}\text{Fe}_x)_n\text{O}_{3n+2}$ ($n = 5, 6$) have been found to be isostructural with $\text{Ca}_n(\text{Nb}, \text{Ti})_n\text{O}_{3n+2}$ ($n = 5, 6$). The lattice parameters at $T = 320$ K are $a_m = 7.8394$ (11), $b_m = 31.591$ (7), $c_m = 5.5468$ (11) Å and $\gamma_m = 97.125$ (16) deg for $n = 5$, and $a_m = 7.8339$ (19), $b_m = 37.133$ (7), $c_m = 5.5520$ (18) Å and $\gamma_m = 96.046$ (16) deg for $n = 6$.

Structure refinements included the free variation of the Ti/Fe ratios on all six crystallographically independent B sites (figure 8.1), as well as any structural distortion allowed by symmetry. The refined compositions are $x = 0.17$ (1) for $n = 5$ and $x = 0.32$ (1) for $n = 6$. These values differ by up to a few standard uncertainties from the nominal values, precluding a meaningful interpretation of these differences. It is noticed that the nominal compositions are in agreement with complete chemical order, where Fe_{11} and Fe_{21} sites could be occupied by Fe and Fe_{12} , Fe_{22} , Fe_{13} and Fe_{23} sites could be occupied by Ti (figure 8.1). In these idealized structures, $n = 6$ would contain 2D lattices of magnetic ions, while $n = 5$ would contain magnetic $\text{Fe}_{11}/\text{Fe}_{21}$ chains along \mathbf{a} , arranged in planes at the centers of the slabs. The observed partial chemical order corresponds to dilution of the low-dimensional magnetic systems, while a small fraction of magnetic ions is then found in the $\text{Fe}_{12}/\text{Fe}_{22}$ layers [figures 8.2(c) and 8.2(d)]. The diffraction experiments did not show any structured diffuse scattering nor an increased level of diffuse scattering. On the basis of these observations, we can exclude strong correlations between occupancies of neighboring sites. The presence of two-dimensional Fe clusters within the $\text{Fe}_{11}/\text{Fe}_{21}$ layers, as discussed below, will thus be the result of a pure statistical process.

The crossover of magnetic behavior of $\text{La}_6(\text{Ti}_{0.67}\text{Fe}_{0.33})_6\text{O}_{20}$ ($n = 6$) does not arise due to temperature-dependent structural distortions, because crystal structures of both $n = 5$ and $n = 6$ are essentially independent of the temperature, while small variations of, for example, the Fe–O–Fe bond angle are similar for $n = 5$ and $n = 6$ (figures 8.2(a) and (b)). Phase transitions have not been found between 90 and 350 K.

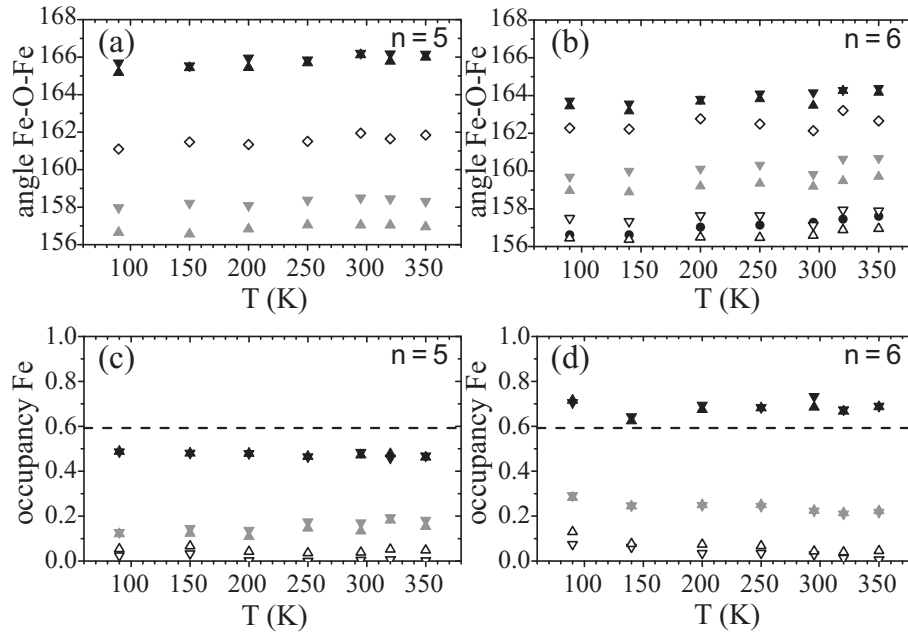


Figure 8.2: The temperature dependence of selected structural features of $\text{La}_5(\text{Ti}_{0.8}\text{Fe}_{0.2})_5\text{O}_{17}$ and $\text{La}_6(\text{Ti}_{0.67}\text{Fe}_{0.33})_6\text{O}_{20}$. The bond angle B–O–B for selected contacts between BO_6 octahedral groups in (a) $n = 5$, and (b) $n = 6$. The occupancy by Fe of the six crystallographically independent B sites in (c) $n = 5$, and (d) $n = 6$. Occupancies of Fe_{11} (black), Fe_{12} (grey), Fe_{13} (open symbol) are given by triangles pointing down. The triangles pointing up indicate occupancies of Fe_{21} (black), Fe_{22} (grey) and Fe_{23} (open symbol). The percolation threshold of the two-dimensional square lattice is indicated by dashed lines.

8.4 Discussion

The refined structure models involve incomplete Ti/Fe ordering over the B sites (figures 8.2(c) and (d)), similar to the incomplete Nb/Ti ordering in $\text{Ca}_n(\text{Nb,Ti})_n\text{O}_{3n+2}$ ($n = 5, 6$) (Guevarra et al., 2007). Despite double \mathbf{a} axes, sites related by an approximate translation of $\frac{1}{2}\mathbf{a}_m = \mathbf{a}_o$ have nearly equal occupancies. The Fe_{13} and Fe_{23} sites are almost exclusively occupied by non-magnetic Ti^{4+} . Accordingly, the structures contain non-magnetic layers of a width equal to the length of two octahedral groups plus one inter-slab spacing (compare figure 8.1), implying that both compounds form two-dimensional magnetic systems in very good approximation.

Each BO_6 octahedral group in the perovskite structure is connected to six neighboring octahedral groups by B–O–B contacts via common oxygen atoms. Assuming these linkages to represent the paths of largest magnetic interactions, the following model can be developed. One layer of perovskite structure supports strong magnetic interactions along \mathbf{a} , but no obvious magnetic coupling along \mathbf{b} . A pair of layers then forms a two-dimensional magnetic lattice [compare figure 8.1(c)].

The major fraction of iron ions in $\text{La}_6(\text{Ti}_{0.67}\text{Fe}_{0.33})_6\text{O}_{20}$ ($n = 6$) is located in the two central layers of the slab, and $n = 6$ contains a two-dimensional magnetic lattice. In case of perfect chemical order $n = 6$ would be a pure two-dimensional magnetic system. Long-range magnetic order could be expected at low temperatures due to very weak interlayer magnetic interactions or magnetoelastic coupling, which would render the system effectively three-dimensional.

The two-dimensional magnetic lattice in $n = 6$ contains a substantial fraction of non-magnetic sites, which—together with the the large separation and concomitantly very weak interactions between neighboring magnetic layers—is sufficient to prevent long-range magnetic order down to at least 4 K. Nevertheless, the occupancy fraction of $p = 0.67$ (3) of magnetic Fe^{3+} ions on Fe_{11} and Fe_{21} sites is above the percolation limit of $p_c = 0.593$ for the two-dimensional square lattice (Ziff, 1992). Accordingly, large patches of neighboring magnetic sites can be expected to be present within each layer of $\text{La}_6(\text{Ti}_{0.67}\text{Fe}_{0.33})_6\text{O}_{20}$.

The crystal structure of $n = 6$ can thus be visualized as containing two-dimensional clusters of iron atoms of varying sizes located at the center of the slabs. Strong magnetic interactions exist within a cluster, while clusters are bounded by many B sites occupied by Ti^{4+} (magnetic 'vacancies') and might have only an occasional magnetic bridge to a neighboring cluster within the same slab. The temperature dependence of the magnetic susceptibility at high temperatures indicates that the

strong magnetic coupling between iron atoms is ferromagnetic ($\theta^{high} = 281$ K in figure 8.3).

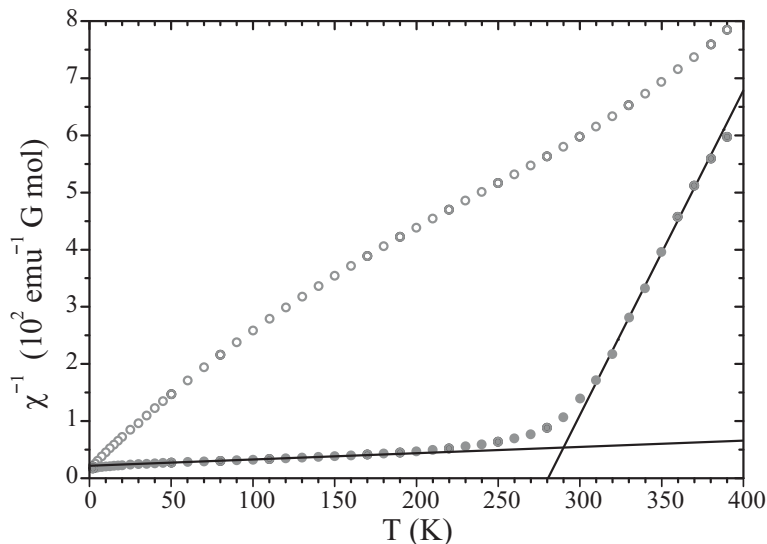


Figure 8.3: Inverse magnetic susceptibility χ^{-1} as a function of temperature for $\text{La}_5(\text{Ti}_{0.8}\text{Fe}_{0.2})_5\text{O}_{17}$ (open circles) and $\text{La}_6(\text{Ti}_{0.67}\text{Fe}_{0.33})_6\text{O}_{20}$ (filled circles). Data reproduced from Lichtenberg et al. (2008). Solid lines represent fits of the Curie-Weiss law, $\chi^{-1} = (T - \theta)/C_{\text{Curie}}$, to the data of $n = 6$. For the temperature range of 50–150 K parameters are $C_{\text{Curie}}^{low} = 9.066 \text{ emuG}^{-1}\text{Kmol}^{-1}$ and $\theta^{low} = -196$ K; for the temperature range of 310–380 K parameters are $C_{\text{Curie}}^{high} = 0.176 \text{ emuG}^{-1}\text{K mol}^{-1}$ and $\theta^{high} = 281$ K.

We propose that at low temperatures, short-range magnetic order of the moments of Fe^{3+} ions exists within two-dimensional clusters, while different clusters have independent orientations of their moments, so that the state of two-dimensional magnetic clusters is again paramagnetic. It is noticed that the two-dimensional magnetic lattices in the compounds presently studied have larger separations and are much more weakly coupled than those in diluted two-dimensional magnetic compounds with the K_2NiF_4 type crystal structure, like $\text{Rb}_2\text{Co}_y\text{Mg}_{1-y}\text{F}_4$ ($0 < y < 1$) (Cowley et al., 1980).

The Curie-Weiss theory describes the temperature dependence of the response to magnetic fields by two parameters (Blundell, 2001). The first is the temperature θ , which is positive for ferromagnetic and negative for antiferromagnetic interactions. Its magnitude is a measure for the strength of the interactions, and observed values of 281 and -196 K indicate strong interactions. The second parameter is the Curie

constant C_{Curie} , which is the inverse slope of χ^{-1} vs temperature. Its value is related to the concentration of magnetic sites and the magnitude μ_{eff} of the magnetic moment of each site, according to Blundell (2001),

$$C_{\text{Curie}} = \frac{\mu_0}{3k_B} \frac{N}{V} \mu_{\text{eff}}^2 \quad (8.1)$$

where μ_0 is the permeability of vacuum, k_B is the Boltzmann constant, and N is the number of moments in volume V .

The magnetic moment of one Fe^{3+} ion is known, and the concentration of these ions can be computed from the chemical formula and unit-cell volume. If clusters of N_C ferromagnetically coupled iron ions are formed, the moment of one cluster is N_C times the moment of one Fe^{3+} ion, while the concentration of clusters is exactly $\frac{1}{N_C}$ of the concentration of Fe^{3+} ions. The different dependencies of the Curie constant on the effective magnetic moment and the concentration of magnetic ions (equation 8.1), then allow the average size of magnetic clusters to be computed from the ratio of Curie constants at low and high temperatures (figure 8.3),

$$N_C = \frac{C_{\text{Curie}}^{\text{low}}}{C_{\text{Curie}}^{\text{high}}} = 51.5. \quad (8.2)$$

The boundaries of magnetic clusters are defined by a high concentration of non-magnetic Ti^{4+} ions at B sites. The supposedly ferromagnetic interactions between clusters thus rely on a few inter-cluster contacts within one slab and will be much reduced as compared to the ferromagnetic coupling of individual Fe^{3+} ions. On the other hand, any magnetic interactions between clusters in neighboring slabs will be enhanced by at least a factor of N_C as compared to the magnetic interactions between individual atoms. Together, these effects may explain the crossover from strong ferromagnetic coupling between iron ions at high temperatures to predominantly antiferromagnetic coupling between magnetic clusters at low temperatures.

The situation for $\text{La}_5(\text{Ti}_{0.8}\text{Fe}_{0.2})_5\text{O}_{17}$ ($n = 5$) is different. Fe_{11} and Fe_{21} sites with iron occupancies of $p_{11} = 0.46$ (2) and $p_{21} = 0.47$ (2) form one layer of perovskite structure with strong magnetic interactions along **a**. The two-dimensional lattice is completed by the layers of Fe_{12} ($p_{12} = 0.19$ (2)) and Fe_{22} ($p_{12} = 0.18$ (2)). Strong magnetic interactions along **b** involve one Fe_{11} site and either one of the two possible Fe_{12} in the neighboring layers (figure 8.1(a)), whose occupancies thus need to be combined to compute the probability of the presence of a magnetic ion on this site of the square lattice. In $n = 5$, a square lattice of magnetic B sites thus exists

with alternating occupancies of $p_{high} = 0.47$ and $p_{low} = 0.37$. Both values are much smaller than the occupancy by magnetic ions of the square lattice in $n = 6$. Furthermore, both values are well below the percolation limit, which then explains the absence of the formation of extended magnetic clusters in $n = 5$. Nevertheless, the magnetic behavior of $n = 5$ deviates from that of an ideal paramagnet with a slope of $\chi^{-1}(T)$ that continuously changes with temperature. This behavior suggests that local correlations between magnetic moments might still develop in $n = 5$ for magnetic ions belonging to single clusters of Fe atoms of small sizes.

8.5 Conclusions

We have argued that the crossover at room temperature of magnetic behavior of $\text{La}_6(\text{Ti}_{0.67}\text{Fe}_{0.33})_6\text{O}_{20}$ ($n = 6$) is the result of the formation of two-dimensional magnetic clusters of average size of 51.5 Fe^{3+} ions. The formation of clusters is facilitated by chemical order, concentrating iron at the centers of the slabs of perovskite-type structure (figure 8.1). The absence of clear magnetic correlations in $\text{La}_5(\text{Ti}_{0.8}\text{Fe}_{0.2})_5\text{O}_{17}$ ($n = 5$) is explained by the lower concentration of magnetic Fe^{3+} ions in $n = 5$ as compared to $n = 6$. Long-range magnetic order might develop in compounds $\text{A}_n\text{B}_n\text{O}_{3n+2}$ with still higher concentrations of iron in the central layers. The synthesis of compounds with a higher iron content is conceivable if more than three elements with different valencies are considered for the A and B sites. Furthermore, the chemical order might be increased by combining elements of more different ion sizes. Finally, it is noticed that compounds $\text{A}_n\text{B}_n\text{O}_{3n+2}$ with odd values of n form centrosymmetric structures, while those with even n are acentric. $n = 6$ compounds are thus suitable candidates for multiferroic properties.

Chapter 9

Summary

This dissertation reports on the results of studies on magnetic materials on the basis of the analysis of exemplary low temperature crystal structures of the ternary carbide SmNiC_2 and the perovskite-related layered compounds $\text{La}_5(\text{Ti}_{0.80}\text{Fe}_{0.20})_5\text{O}_{17}$ and $\text{La}_6(\text{Ti}_{0.67}\text{Fe}_{0.33})_6\text{O}_{20}$.

Structural properties were analyzed in dependence of the temperature by use of single-crystal X-ray diffraction. The X-ray diffraction experiments gave exact diffraction intensities, used for the refinement of crystal structures at different temperatures as well as precise reflection positions for the determination of the temperature-dependent evolution of the lattice parameters. Moreover, the possibility of a lowering of the lattice symmetry at different temperatures was examined and the exact value of the modulation wave vector was determined in the modulated state. By use of integrated diffraction intensities, crystal structures were described either as incommensurate (in the case of SmNiC_2) or as commensurate modulated superstructures (in the case of $\text{La}_5(\text{Ti}_{0.80}\text{Fe}_{0.20})_5\text{O}_{17}$ and $\text{La}_6(\text{Ti}_{0.67}\text{Fe}_{0.33})_6\text{O}_{20}$).

Measurements of SmNiC_2 were performed at beamline D3 of HASYLAB at DESY, Hamburg, within the temperature range 8–300 K and at the Laboratory of Crystallography at the University of Bayreuth at room temperature. At both sites four-circle-diffractometer with a point detector attached were available for this purpose. The analysis of the integrated diffraction intensities allowed an identification of the room temperature structure as a normal periodic structure of the CeNiC_2 -type. The refined structure model matched well with the data from the measurement.

In low-temperature experiments reflection peaks were analyzed for a possible peak-splitting as a consequence of a lowering of the symmetry of the crystal lattice by use of ω - 2θ -maps in the charge-density wave state as well as in the ferromag-

netically ordered state. It was found, that no lattice distortion is associated with the changes of the magnetic properties. At 60 K and at 9 K the crystal lattice has orthorhombic symmetry. By use of so-called \mathbf{q} -scans the existence of first order satellites was confirmed and the exact values of the components of the modulation wave vector \mathbf{q}_{CDW} were determined. Satellite reflections of higher order could not be found neither with \mathbf{q} -scans nor during the data collection of reflection intensities at potential reflection positions.

From the intensities of main and satellite reflections, measured at 60 K, a structure model was found, which describes the incommensurately modulated structure in the charge-density wave state. The refined structure model matched well with the diffraction data of the measurement. The basic structure is described by layers of Sm and Ni atoms, stacked along the \mathbf{c} axis. Between the layers C atoms are arranged as rigid C_2 dumbbells. Ni atoms form dimerized chains along the \mathbf{a} axis and show the largest displacement modulation of all atoms as well as the largest variations of the bond distances to neighboring atoms. Thus, the Ni atoms carry the valence band, which is responsible for the charge-density wave. This result is confirmed by a measurement of the electrical resistivity, which is smallest along the \mathbf{a} axis. From these results it follows, that for a single layer of Ni atoms a commensurate \mathbf{q}_{CDW} would result. A frustration is caused by the interchange of the modulation with the lattice centering of the structure, which renders the modulation incommensurate in all layers.

As representatives of another kind of compounds the $n = 5$ and $n = 6$ members of the homologous series of perovskite-related layered compounds $A_nB_nO_{3n+2}$, $La_5(Ti_{0.80}Fe_{0.20})_5O_{17}$ and $La_6(Ti_{0.67}Fe_{0.33})_6O_{20}$, were analyzed. The compounds of this class consist of layers of the perovskite-type structure. The thickness of each layer is given by the parameter n , which represents the number of BO_6 octahedra in a layer along the stacking direction. Both compounds have fundamentally different symmetries. While the $n = 5$ compound is centrosymmetric, the $n = 6$ compound is acentric. Nevertheless, it is possible to describe both structures on the basis of a unique structure type within (3+1)-dimensional superspace with modulation functions and modulation wave vectors depending in a systematic way on n .

The two compounds in the focus of the research show completely different magnetic properties, which are revealed in the temperature-dependent magnetic susceptibility. Measurements show for the $n = 6$ compound a behavior clearly different from the common paramagnetic characteristic with a ferromagnetic interaction of the magnetic moments at higher temperatures. At about room temperature a

crossover to an antiferromagnetic interaction is visible, but no phase-transition appears. Whereas the $n = 5$ compound does not show a crossover nor a clear (anti-)ferromagnetic interaction can be found (Lichtenberg et al., 2008).

Single-crystal X-ray diffraction experiments were done in the temperature range 90–350 K with a Marresearch Mar345dtb image-plate diffractometer at the Laboratory of Crystallography at the University of Bayreuth for the examination of the structural reasons of the differences. The higher dimensional structural model was adapted successfully for both compounds, resulting in a sufficient match of the model and the diffraction data. In both compounds no structural phase-transition was found. Moreover, selected structural parameters, as for example the B–O–B bond angle, do not show any noticeable change at temperatures of about 290 K.

Instead the maximum concentration of magnetic Fe atoms realized in the central layers of each slab is suggested as the mechanism for the different magnetic properties. In the case of the $n = 5$ compound the maximum concentration is too low for the formation of magnetic interacting clusters. In the case of $n = 6$ clusters of 52 iron ions in average are formed. At temperature above room temperature the magnetic moments of the iron atoms within the clusters are aligned parallel by applying an external magnetic field, while the magnetic moments of neighboring clusters are aligned anti-parallel at lower temperatures. This effect explains the crossover of the temperature-dependent behavior of the magnetic susceptibility. Both compounds, however, do not show a long-range magnetic order at any temperature, but remain always paramagnetic.

By use of the diffraction data an anisotropic thermal expansion was found in both compounds with the strongest expansion along an axis parallel to the layers. This is different to the expansion in many other layered structures. The mechanism was found in a tilting of BO_6 octahedra, mainly about an axis parallel to the crystallographic \mathbf{b} axis. At high temperatures the octahedra are arranged more parallel to the \mathbf{a} axis as at lower temperatures. As a consequence the \mathbf{a} axis shows the strongest thermal expansion, at least in the high temperature range. A similar mechanism is proposed to be valid for the thermal evolution in other $\text{A}_n\text{B}_n\text{O}_{3n+2}$ compounds, too. This behavior is in contrast to the anisotropy of the compressibility, as it has been found for $\text{La}_5\text{Ti}_5\text{O}_{17}$ (Loa et al., 2004) with the strongest compression along the stacking axis. As a consequence of hydrostatic pressure the interslab distance along the stacking direction is compressed strongly, while the thickness of the slabs is changed clearly less. In contrast the slabs show a clear expansion with rising temperature, while the interslab distances are almost temperature-independent.

Analysis of the diffraction data revealed an incomplete order of Fe/Ti at the B-sites, which is almost temperature-independent. A comparison with the chemical order in other $A_nB_nO_{3n+2}$ compounds allowed an identification of a local charge balancing as the driving force, with the ion of highest valence concentrated at the borders of the slabs. Thus, the accumulation of oxygen atoms there is balanced. In a similar way the distortion of the octahedra is temperature-independent, with a decreasing strength of the distortion from the borders of the slab towards the center. No relation between the nature or valence of the ions in the center of the octahedra and the strength of the distortion seems to exist, because the dependence from the positions of the octahedra exists in a similar way in all known $A_nB_nO_{3n+2}$ compounds, where these distortions have been analyzed (Drews et al., 1996; Guevarra et al., 2005b; 2007). Instead the distortion seems to be the result of resolving internal stress between neighboring slabs.

Valences of Ti and Fe ions were calculated with the Bond-Valence method. The results show, that calculated valences depend on the site occupancy by Ti and Fe ions. The best agreement between formal and calculated valences are found for sites, which are almost exclusively occupied by Ti ions. A similar good coincidence follows for a exclusive occupancy of Fe ions from a linear extrapolation of the refined site occupancies of the iron ions. In these cases the oxygen environment and the valences of Ti are that of Ti^{4+} and the oxygen environment and the valences of Fe are that of Fe^{3+} . At sites occupied by both ions the refined oxygen positions represent the average of oxygen positions in TiO_6 and FeO_6 octahedra, weighted to the occupancies of Ti^{4+} and Fe^{3+} .

This dissertation shows, that the concept of superstructures in magnetic compounds can be extended successfully to incompletely ordered magnetic systems and to those systems, which arise as the consequence of a phase transition from magnetic ordered systems.

Chapter 10

Zusammenfassung

Diese Dissertation berichtet die Ergebnisse von Untersuchungen an magnetischen Materialien auf Basis der Analyse beispielhafter Tieftemperaturstrukturen des ternären Carbids SmNiC_2 und der perowskitartigen Schichtverbindungen $\text{La}_5(\text{Ti}_{0.80}\text{Fe}_{0.20})_5\text{O}_{17}$ und $\text{La}_6(\text{Ti}_{0.67}\text{Fe}_{0.33})_6\text{O}_{20}$.

Die strukturellen Eigenschaften wurden temperaturabhängig mittels Einkristallröntgenbeugung untersucht. Bei den Röntgenbeugungsexperimenten wurden sowohl genaue Reflexintensitäten für die Verfeinerung von Kristallstrukturen bei verschiedenen Temperaturen, als auch präzise Reflexlagen für die Ermittlung der temperaturbedingten Änderungen der Gitterkonstanten gemessen. Des Weiteren wurde im Hinblick auf eine mögliche Abnahme der Gittersymmetrie bei verschiedenen Temperaturen untersucht und der genaue Wert des Modulationswellenvektors in einem modulierten Phasenzustand ermittelt. Mit Hilfe der integrierten Reflexintensitäten konnten die Strukturen beider Verbindungsklassen in den untersuchten Temperaturbereichen durch inkommensurabel (im Fall von SmNiC_2) bzw. durch kommensurabel modulierte Überstrukturen (im Fall von $\text{La}_n(\text{Ti}_{1-x}\text{Fe}_x)_n\text{O}_{3n+2}$ mit $n = 5$ und 6) beschrieben werden.

Für SmNiC_2 wurden Messungen an der Strahllinie D3 des HASYLABS am DESY in Hamburg im Temperaturbereich zwischen 8 und etwa 300 K sowie am Lehrstuhl für Kristallographie der Universität Bayreuth bei Raumtemperatur durchgeführt. An beiden Messstätten standen hierzu Vierkreis-Diffraktometer, ausgerüstet mit Punktzählern zur Verfügung. In Folge der Analyse der integrierten Reflexintensitäten konnte die Struktur bei Raumtemperatur als gewöhnliche, periodische Kristallstruktur des CeNiC_2 -Typs identifiziert werden. Das verfeinerte Strukturmodell zeigte eine sehr gute Übereinstimmung mit den gemessenen Daten.

In Tieftemperaturexperimenten wurden Reflexe in Hinblick auf eine mögliche Aufspaltung in Folge einer Symmetrierniedrigung des Kristallgitters durch ω - 2θ -Maps sowohl des Ladungsdichtewellenzustandes, als auch des ferromagnetisch geordneten Zustandes untersucht. Es zeigte sich, dass keine Gitterverzerrung mit den Veränderungen der magnetischen Eigenschaften einhergeht. Sowohl bei 60 K, als auch bei 9 K liegt ein orthorhombisches Kristallgitter vor. Mit Hilfe sogenannter \mathbf{q} -scans konnte die Existenz von Satelliten erster Ordnung bestätigt und die exakten Werte der Komponenten des Modulationswellenvektors \mathbf{q}_{CDW} bestimmt werden. Satelliten höherer Ordnungen konnten weder in \mathbf{q} -scans, noch in Rahmen der Intensitätsmessungen an potentiellen Reflexpositionen gefunden werden.

Aus den integrierten Intensitäten der Haupt- und Satellitenreflexe, gemessen bei 60 K ließ sich ein Strukturmodell erarbeiten, dass die inkommensurabel modulierte Struktur im Zustand der Ladungsdichtewelle beschreibt. Das verfeinerte Modell lieferte eine sehr gute Übereinstimmung mit den gemessenen Reflexintensitäten. Die Basisstruktur kann beschrieben werden, als bestehend aus einzelnen Schichten von Sm und Ni Atomen, die entlang der \mathbf{c} Achse gestapelt sind. Zwischen diesen Schichten sind C Atome als starre C_2 -Hanteln angeordnet. Ni Atome formen dimerisierte Ketten entlang der \mathbf{a} Achse und zeigen sowohl die größte Verschiebungsmodulation aller Atome als auch die größte Variation der Bindungslängen zu benachbarten Atomen. Daher lassen sich die Ni Atome als Träger des Valenzbandes identifizieren, das für die Ladungsdichtewelle verantwortlich ist. Dies haben auch Messungen des elektrischen Widerstands bestätigt, der entlang der \mathbf{a} Achse den kleinsten Wert annimmt. Aus diesem Ergebnis folgt, dass sich für eine einzelne Schicht von Ni Atomen ein kommensurabler \mathbf{q}_{CDW} ergeben würde. Durch die Wechselwirkung der Modulation und der Gitterzentrierung der Kristallstruktur kommt es allerdings zu einer Frustration, die in einer inkommensurablen Modulation aller Schichten resultiert.

Als eine weitere Verbindungsklasse wurden die $n = 5$ und 6 Vertreter der homologen Reihe perowskitartiger Schichtverbindungen $A_nB_nO_{3n+2}$, $La_5(Ti_{0.80}Fe_{0.20})_5O_{17}$ und $La_6(Ti_{0.70}Fe_{0.30})_6O_{20}$, untersucht. Bei den Verbindungen dieser Klasse handelt es sich um schichtartige Kristallstrukturen, die aus Schichten des Perowskit-Strukturtyps bestehen. Die Dicke einer Schicht ist durch den Parameter n bestimmt, der die Anzahl der BO_6 Oktaeder in einer Schicht entlang der Stapelrichtung angibt. Beide SVerbindungen unterscheiden sich grundlegend in ihrer Symmetrie. Während die $n = 5$ Verbindung zentrosymmetrisch ist, ist die $n = 6$ Verbindung azentrisch. Dennoch ist es möglich beide Strukturen auf Basis eines einzigen Strukturtyps im

(3+1)-dimensionalen Superraum zu beschreiben, wobei Modulationsfunktionen und Modulationswellenvektoren systematisch von n abhängen.

Die beiden untersuchten Verbindungen zeigen deutlich unterschiedliche magnetischen Eigenschaften, die sich durch die temperaturabhängige magnetische Suszeptibilität ausdrücken lassen. Deren Messung zeigt für $n = 6$ ein deutliches von der üblichen paramagnetischen Charakteristik abweichendes Verhalten mit einer ferromagnetischen Wechselwirkung der magnetischen Momente bei höheren Temperaturen. Bei etwa Raumtemperatur ereignet sich ein Übergang zu einem antiferromagnetischen Verhalten bei niedrigeren Temperaturen, der aber nicht mit einer Phasenumwandlung einhergeht. Für die $n = 5$ Verbindungen hingegen ist kein derartiger Übergang und auch keine deutliche (anti-) ferromagnetische Wechselwirkung festzustellen (Lichtenberg et al., 2008).

Zur Ermittlung der strukturellen Ursachen der Unterschiede wurden Einkristallröntgenbeugungsexperimente im Temperaturbereich zwischen 90 und 350 K mit einem Marresearch Mar345dtb Image-Plate Diffraktometer am Lehrstuhl für Kristallographie der Universität Bayreuth durchgeführt. Für beide Verbindungen konnte das höherdimensionale Strukturmodell erfolgreich angewendet werden, was zu zufriedenstellenden Übereinstimmungen des Modells und der gemessenen Reflexdaten führte. Für beide Verbindungen konnten keine strukturellen Phasenübergänge ermittelt werden. Auch zeigten die untersuchten Strukturparameter, wie z.B. die Fe-O-Fe Bindungswinkel, keine auffälligen Änderungen im Temperaturbereich um 290 K.

Stattdessen konnte die maximal realisierte Konzentration von magnetischen Eisenionen in den zentralen Schichten der einzelnen Stapel als Ursache für die abweichenden magnetischen Eigenschaften vorgeschlagen werden. Im Falle von $n = 5$ ist diese zu gering, als dass sich magnetische wechselwirkende Cluster ausbilden könnten. Für $n = 6$ liegen derartige Cluster vor, deren durchschnittliche Größe auf 52 Eisenionen bestimmt werden konnte. Bei Temperaturen oberhalb der Raumtemperatur richten sich beim Anlegen eines äußeren magnetischen Felds die magnetischen Momente in den Clustern parallel aus, während sich bei tieferen Temperaturen die magnetischen Momente der Cluster in benachbarten Schichten antiparallel ausrichten. Dieser Vorgang erklärt den Übergang im temperaturabhängigen Verhalten der inversen magnetischen Suszeptibilität. Es soll betont werden, dass beide Verbindungen in keinem Temperaturbereich eine vollständige, langreichweitige magnetische Ordnung erreichen, sondern immer paramagnetisch bleiben.

Mit Hilfe der gemessenen Daten konnte auch ein anisotropes thermisches Ausdehnungsverhalten beider Strukturen ermittelt werden, mit der stärksten Ausdehn-

ung entlang einer Achse parallel zu den Schichten. Dies ist im Widerspruch zum Verhalten vieler anderer Schichtverbindungen. Als Ursache konnte eine Verkipfung der BO_6 Oktaeder, hauptsächlich um eine Achse parallel zur kristallographischen **b** Achse, identifiziert werden. Hierbei richten sich die Oktaeder bei hohen Temperaturen mehr parallel zur **a** Achse aus. Als eine Folge zeigt die **a** Achse, zumindest im Hochtemperaturbereich, die stärkste thermische Ausdehnung. Ein derartiger Mechanismus kann auch für die thermische Ausdehnung in anderen $\text{A}_n\text{B}_n\text{O}_{3n+2}$ Verbindungen angenommen werden. Dieses Verhalten steht im Gegensatz zur Anisotropie der Kompressibilität, wie sie für $\text{La}_5\text{Ti}_5\text{O}_{17}$ ermittelt wurde (Loa et al., 2004). Als Folge des hydrostatischen Drucks werden die Zwischenschichtbereiche entlang der Stapelrichtung stark komprimiert, während sich die Dicke der Stapel deutlich weniger ändert. Im Gegensatz dazu zeigen die Stapelbreiten eine starke thermische Ausdehnung, während die Breite der Zwischenschichtbereiche nahezu unabhängig ist von Temperaturänderungen.

Die Analyse der Daten zeigte, dass die unvollständige chemische Ordnung von Fe/Ti auf den B Gitterplätzen nahezu temperaturunabhängig ist. Aus dem Vergleich mit der chemischen Ordnung in anderen $\text{A}_n\text{B}_n\text{O}_{3n+2}$ Verbindungen ergibt sich ein lokaler Ladungsausgleich als Triebfeder für die chemische Ordnung, bei der das höchstgeladene Ion an den Rändern der Stapel konzentriert ist, wodurch die Anreicherung von Sauerstoffatomen dort ausgeglichen wird. Diese Anordnung erfolgt immer in der geschilderten Weise unabhängig von den jeweiligen, in den Verbindungen vorhandenen Ionen. Auch die Verzerrung der Oktaeder erwies sich als nahezu temperaturunabhängig, wobei die Stärke der Verzerrung von den Rändern der Stapel zu deren Mitten hin abnimmt. Auch hierbei scheint kein Zusammenhang mit der Natur oder der Valenz der Kationen im Zentrum der Oktaeder zu bestehen, denn diese Beziehung besteht gleichartig in allen bekannten $\text{A}_n\text{B}_n\text{O}_{3n+2}$ Verbindungen, an denen diese Verzerrungen untersucht wurden (Drews et al., 1996; Guevarra et al., 2005b; 2007). Stattdessen kann eine Erklärung im damit einhergehenden Abbau von internen Spannungen zwischen den einzelnen Stapeln gegeben werden.

Die Valenzen der Ti und Fe Ionen wurden mittels der Bond-Valence-Methode berechnet. Dabei zeigte sich, dass die berechneten Valenzen von den Besetzungswahrscheinlichkeiten der Gitterplätze mit Fe und Ti Ionen abhängen, während sie weitgehend temperaturunabhängig sind. Die größte Übereinstimmung zwischen formaler und berechneter Valenz ergibt sich für die Gitterplätze, die fast ausschließlich mit Ti Ionen besetzt sind. Eine ähnlich gute Übereinstimmung ergibt sich aus einer linearen Extrapolation der vorkommenden Besetzungswahrscheinlichkeiten

der Eisenionen für eine ausschließliche Besetzung mit Fe Ionen. In diesen Fällen entsprechen die Sauerstoffumgebungen und die Valenzen für Fe, denen von Fe^{3+} und die Sauerstoffumgebungen und die Valenzen für Ti, denen von Ti^{4+} . An gemischt besetzten Gitterplätzen entsprechen die verfeinerten Sauerstoffumgebungen einer Mittelung über die Umgebungen von TiO_6 und FeO_6 Oktaedern gewichtet mit den Besetzungswahrscheinlichkeiten von Fe^{3+} und Ti^{4+} .

In der Dissertation konnte gezeigt werden, dass das Konzept von Überstrukturen magnetischer Verbindungen auch erfolgreich auf nicht vollständig geordnete magnetische Systeme und auf solche Systeme, die sich durch einen Phasenübergang aus magnetisch geordneten Systemen ergeben, erweitert werden kann.

Appendix A

Appendix SmNiC₂

A.1 Step scans to determine the σ_2 value of the modulation vector \mathbf{q}

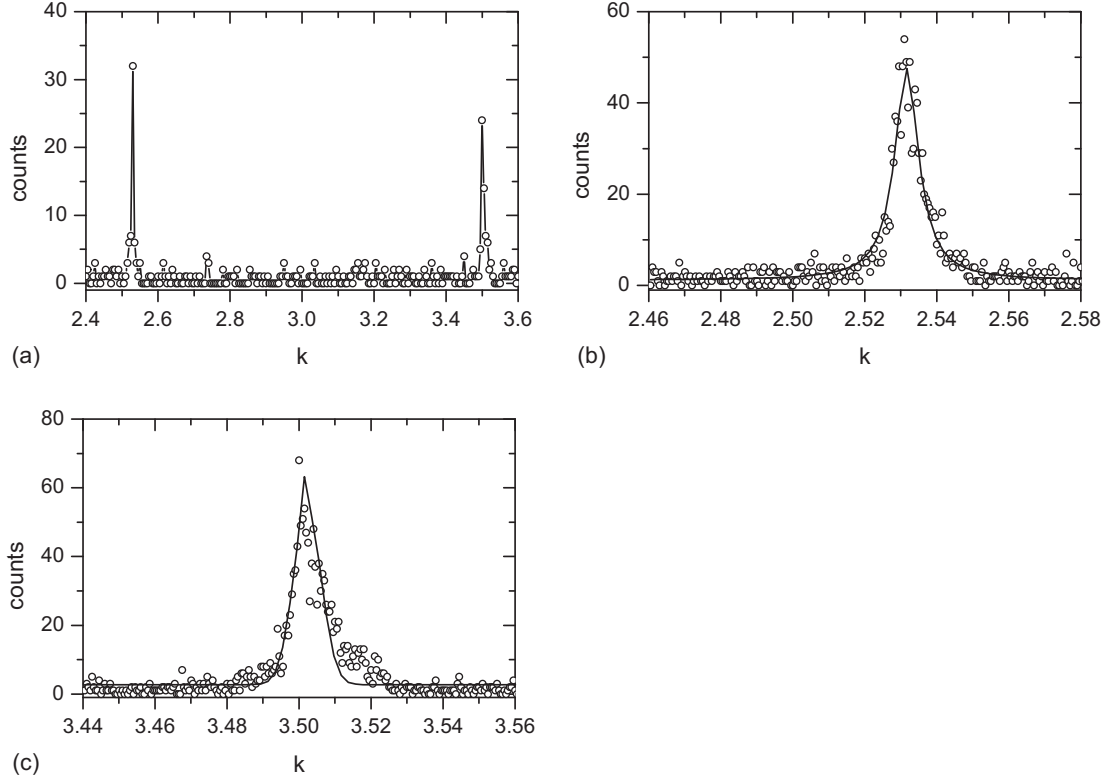


Figure A.1: Step scans along the direction of \mathbf{b}^* . (a) Centered at $(0.5 \ 3.0 \ -2)$, measuring time at each of the 241 steps was 1 s, the distance between two adjacent measuring points were chosen to $0.005 \times b^*$. Two first order satellites are visible with about 25 to 30 counts in the maximum at about $k = 2.525$ and $k = 3.505$. No second order satellites are visible. (b) Centered at $(0.5 \ 2.52 \ -2)$, 241 steps, measuring time 2s/step, step size $0.0005 \times b^*$. Maximum is located at $k = 2.5305$. (c) Centered at $(0.5 \ 3.50 \ -2)$, 241 steps, measuring time 2s/step, step size $0.0005 \times b^*$. Maximum is located at $k = 3.4995$. From both determined reflection positions the exact value of the σ_2 component of the modulation vector $\mathbf{q} = (0.5 \ 0.516 \ 0)$ was calculated. The lines are drawn to guide the eyes.

A.2 Intensities of main and satellite reflections

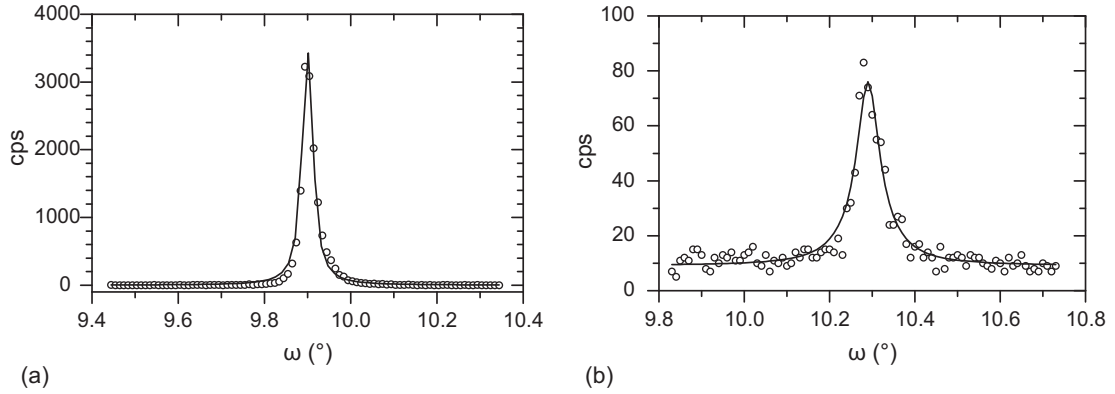


Figure A.2: Comparison of intensities of main and satellite reflections. Reflection profiles for (a) the main reflections $(hklm) = (1\ 2\ \bar{2}\ 0)$ and (b) the satellite reflection $(hklm) = (\bar{2}\ 0\ \bar{4}\ 1)$ of SmNiC_2 , measured in ω scans at 60 K. The main reflection has an average intensity compared with other main reflections of this compound. In contrast the satellite reflection is one of the strongest observed satellite reflections. For both reflections the observed counts are scaled to counts per second in the drawing. The analysis led to intensities after absorption correction of 12716.8 (14.4) and 37.5 (0.5) for $m = 0$ and 1, respectively. This comparison shows that the intensities of the strongest satellite reflections are only some thousandth of the intensities of main reflections. The lines are drawn to guide the eyes.

A.3 Determination of the incidence limit for background radiation caused by use of the closed-cycle cryostat

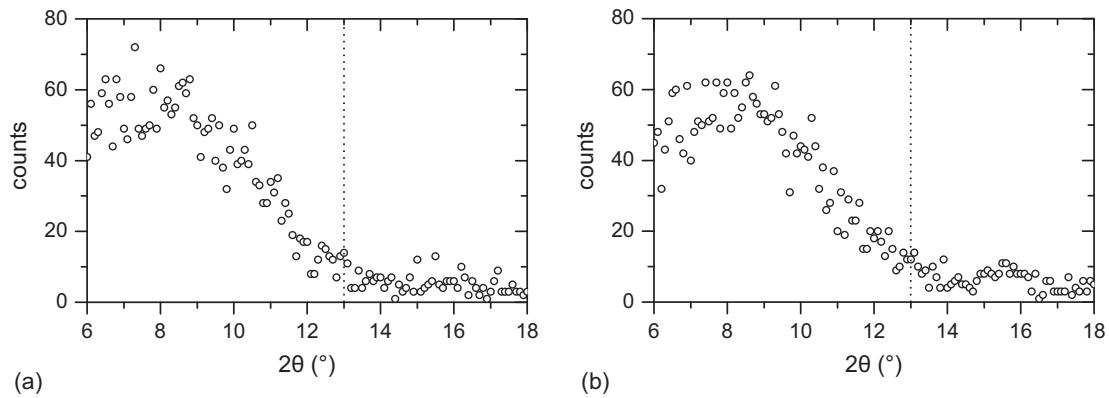


Figure A.3: Step scan along the direction of 2θ for the determination of the angular limit for the incidence of scattered X-rays from the beryllium domes by use of the detector collimator. By the use of the closed-cycle cryostat the background is mainly defined by the scattering of the beryllium domes. A detector collimator prevents the detection of X-rays, diffracted at positions other than the crystal position, for diffraction angles larger than $2\theta_{DC}$ 3.1.2. The measurement was done for SmNiC_2 at 60 K. Both scans are centered in regions away from reflections at positions (a) $(hkl) = (-0.416 -1.520 -1.849)$ and (b) $(hkl) = (-0.186 -1.287 1.986)$. They result in the same value of $2\theta_{DC} = 13^\circ$. For larger diffraction angles than this the measured intensities of Bragg reflections are not influenced by scattering from the beryllium domes.

Appendix B

Appendix $\text{La}_n(\text{Ti}_{1-x}\text{Fe}_x)_n\text{O}_{3n+2}$

$n = 5$ and 6

B.1 Crystallographic details of the structures of $La_5(Ti_{0.80}Fe_{0.20})_5O_{17}$ and $La_6(Ti_{0.67}Fe_{0.33})_6O_{20}$

In the following tables the site occupancies, coordinates and harmonic atomic displacement parameters of the atoms in the supercells are listed for both compounds at temperature $T = 320$ K. The refinement of both structures applied the superspace formalism (van Smaalen, 2007) and the structures were subsequently transformed into the equivalent supercells by use of JANA2006 (Petricek et al., 2006). For the $n = 5$ compound this transformation results in the non-standard centrosymmetric space group $C112_1/d$ with lattice parameter $a = 7.8394(15)$, $b = 62.693(16)$, $c = 5.5468(11)$ Å and $\gamma = 89.997(16)^\circ$ at $T = 320$ K. For the $n = 6$ compound it is the non-centrosymmetric space group $C112_1$ with lattice parameter $a = 7.8339(19)$, $b = 73.853(18)$, $c = 5.5520(16)$ Å and $\gamma = 89.990(16)^\circ$. The standard uncertainties of the refinement can be obtained in electronic forms from the crystal information files (CIFs) of the superspace description for both compounds. The thermal evolution of these structural parameters result only in small changes. Therefore, they are presented here only for one temperature, while structural details at the superspace and supercell description at the other temperatures (Chap. 7) are available as CIFs.

Table B.1: Site occupancy, relative atomic coordinates and equivalent isotropic atomic displacement parameter of the atoms of the superstructure of $La_5(Ti_{0.80}Fe_{0.20})_5O_{17}$ ($n = 5$) at $T = 320$ K.

Atom	occupancy	x	y	z	U_{iso}^{eq} (Å ²)
La1-1	1	0.000000	0.998685	0.001209	0.005333
La1-9	1	0.250054	0.703391	0.000632	0.004444
La1-10	1	0.249030	0.793376	0.005303	0.006042
La2-2	1	0.998875	0.107757	0.910853	0.005821
La3-12	1	0.996845	0.897880	0.044765	0.004313
Ti11-1	0.540774	0.25	0	0.5	0.003485
Fe11-1	0.459226	0.25	0	0.5	0.003485
Ti12-10	0.806845	0.499398	0.796433	0.508289	0.003485
Fe12-10	0.193155	0.499398	0.796433	0.508289	0.003485
Ti13-2	0.993245	0.247191	0.088693	0.460064	0.003485

Continued on next page ...

Table B.1: Continued from previous page

Atom	occupancy	x	y	z	U_{iso}^{eq} (\AA^2)
Fe13-2	0.006755	0.247191	0.088693	0.460064	0.003485
Ti21-1	0.522212	0.75	0	0.5	0.003390
Fe21-1	0.477788	0.75	0	0.5	0.003390
Ti22-10	0.817870	0.997505	0.796696	0.506964	0.003390
Fe22-10	0.182130	0.997505	0.796696	0.506964	0.003390
Ti23-2	0.947986	0.750668	0.089336	0.456412	0.003390
Fe23-2	0.052014	0.750668	0.089336	0.456412	0.003390
01-1	1	0.000240	0.000000	0.557084	0.007328
01-2	1	0.000489	0.084604	0.531750	0.007328
01-9	1	0.249647	0.709045	0.554009	0.007328
01-10	1	0.249319	0.794018	0.554307	0.007328
01-12	1	0.998955	0.914188	0.575775	0.007328
02-1	1	0.216510	0.018959	0.221320	0.006937
02-2	1	0.235272	0.106195	0.197263	0.006937
02-8	1	0.486708	0.639355	0.182293	0.006937
02-9	1	0.476717	0.725365	0.222401	0.006937
02-10	1	0.484820	0.810663	0.206254	0.006937
02-12	1	0.206129	0.931907	0.221208	0.006937
03-1	1	0.782802	0.018703	0.218682	0.006760
03-2	1	0.766447	0.104433	0.186125	0.006760
03-8	1	0.011821	0.637699	0.173661	0.006760
03-9	1	0.023677	0.724820	0.222081	0.006760
03-10	1	0.013495	0.810333	0.202963	0.006760
03-12	1	0.794422	0.931331	0.214669	0.006760

Table B.2: Anisotropic atomic displacement parameters of the atoms of the superstructure of $La_5(Ti_{0.80}Fe_{0.20})_5O_{17}$ ($n = 5$) at temperature $T = 320$ K.

Atom	U_{11} (\AA^2)	U_{22} (\AA^2)	U_{33} (\AA^2)	U_{12} (\AA^2)	U_{13} (\AA^2)	U_{23} (\AA^2)
La1-1	0.005122	0.005973	0.004904	-0.001046	-0.000068	-0.000969
La1-9	0.002920	0.005575	0.004838	0.001120	-0.000465	-0.001550
La1-10	0.003745	0.008164	0.006218	0.000299	-0.000119	-0.002308
La2-2	0.002930	0.009757	0.004777	-0.000871	0.000458	-0.002537
La3-12	0.002565	0.019513	0.010220	0.000896	-0.000350	-0.006642
Ti11-1	0.003886	0.003783	0.002785	-0.000324	-0.000846	-0.000405
Fe11-1	0.003886	0.003783	0.002785	-0.000324	-0.000846	-0.000405
Ti12-10	0.003886	0.003783	0.002785	-0.000324	-0.000846	-0.000405
Fe12-10	0.003886	0.003783	0.002785	-0.000324	-0.000846	-0.000405
Ti13-2	0.003886	0.003783	0.002785	-0.000324	-0.000846	-0.000405
Fe13-2	0.003886	0.003783	0.002785	-0.000324	-0.000846	-0.000405
Ti21-1	0.003829	0.003783	0.002559	-0.000050	-0.000531	0.000000
Fe21-1	0.003829	0.003783	0.002559	-0.000050	-0.000531	0.000000
Ti22-10	0.003829	0.003783	0.002559	-0.000050	-0.000531	0.000000
Fe22-10	0.003829	0.003783	0.002559	-0.000050	-0.000531	0.000000
Ti23-2	0.003829	0.003783	0.002559	-0.000050	-0.000531	0.000000
Fe23-2	0.003829	0.003783	0.002559	-0.000050	-0.000531	0.000000
01-1	0.003780	0.008164	0.010041	-0.001145	0.000308	-0.000511
01-2	0.003780	0.008164	0.010041	-0.001145	0.000308	-0.000511
01-9	0.003780	0.008164	0.010041	-0.001145	0.000308	-0.000511
01-10	0.003780	0.008164	0.010041	-0.001145	0.000308	-0.000511
01-12	0.003780	0.008164	0.010041	-0.001145	0.000308	-0.000511
02-1	0.007407	0.007168	0.006236	-0.000274	-0.000128	0.001180
02-2	0.007407	0.007168	0.006236	-0.000274	-0.000128	0.001180
02-8	0.007407	0.007168	0.006236	-0.000274	-0.000128	0.001180
02-9	0.007407	0.007168	0.006236	-0.000274	-0.000128	0.001180
02-10	0.007407	0.007168	0.006236	-0.000274	-0.000128	0.001180

Continued on next page ...

Table B.2: Continued from previous page

Atom	U_{11} (\AA^2)	U_{22} (\AA^2)	U_{33} (\AA^2)	U_{12} (\AA^2)	U_{13} (\AA^2)	U_{23} (\AA^2)
02-12	0.007407	0.007168	0.006236	-0.000274	-0.000128	0.001180
03-1	0.008702	0.006969	0.004609	-0.000199	0.000797	0.002872
03-2	0.008702	0.006969	0.004609	-0.000199	0.000797	0.002872
03-8	0.008702	0.006969	0.004609	-0.000199	0.000797	0.002872
03-9	0.008702	0.006969	0.004609	-0.000199	0.000797	0.002872
03-10	0.008702	0.006969	0.004609	-0.000199	0.000797	0.002872
03-12	0.008702	0.006969	0.004609	-0.000199	0.000797	0.002872

Table B.3: Site occupancy, relative atomic coordinates and equivalent isotropic atomic displacement parameter of the atoms of the superstructure of $La_6(Ti_{0.67}Fe_{0.33})_6O_{20}$ ($n = 6$) at temperature $T = 320$ K.

Atom	occupancy	x	y	z	U_{iso}^{eq} (\AA^2)
La1-1a	1	0.000000	0.767706	0.003230	0.008367
La1-1b	1	0.750000	0.017706	0.003230	0.008367
La1-7a	1	0.000243	0.194150	0.997302	0.008703
La1-7b	1	0.750243	0.444150	0.997302	0.008703
La1-8a	1	0.000108	0.270412	0.997206	0.007599
La1-8b	1	0.750108	0.520412	0.997206	0.007599
La1-14a	1	0.999541	0.691611	0.001437	0.006999
La1-14b	1	0.749541	0.941611	0.001437	0.006999
La2-2a	1	0.998359	0.860418	0.910388	0.008458
La2-2b	1	0.748359	0.110418	0.910388	0.008458
La3-9a	1	0.002370	0.355966	0.949990	0.014731
La3-9b	1	0.752370	0.605966	0.949990	0.014731
Ti11-1a	0.326490	0.250439	0.768953	0.495543	0.005524
Fe11-1a	0.673510	0.250439	0.768953	0.495543	0.005524
Ti11-1b	0.326490	0.000439	0.018953	0.495543	0.005524
Fe11-1b	0.673510	0.000439	0.018953	0.495543	0.005524

Continued on next page ...

Table B.3: Continued from previous page

Atom	occupancy	x	y	z	U_{iso}^{eq} (\AA^2)
Ti12-7a	0.790130	0.752255	0.191869	0.490742	0.005524
Fe12-7a	0.209870	0.752255	0.191869	0.490742	0.005524
Ti12-7b	0.790130	0.502255	0.401869	0.490742	0.005524
Fe12-7b	0.209870	0.502255	0.401869	0.490742	0.005524
Ti13-2a	0.986394	0.246719	0.844318	0.457535	0.005524
Fe13-2a	0.013606	0.246719	0.844318	0.457535	0.005524
Ti13-2b	0.986394	0.996719	0.094318	0.457535	0.005524
Fe13-2b	0.013606	0.996719	0.094318	0.457535	0.005524
Ti21-1a	0.333042	0.751698	0.768928	0.495201	0.005223
Fe21-1a	0.666958	0.751698	0.768928	0.495201	0.005223
Ti21-1b	0.333042	0.501698	0.018928	0.495201	0.005223
Fe21-1b	0.666958	0.501698	0.018928	0.495201	0.005223
Ti22-7a	0.785568	0.253844	0.191618	0.492255	0.005223
Fe22-7a	0.214432	0.253844	0.191618	0.492255	0.005223
Ti22-7a	0.785568	0.253844	0.191618	0.492255	0.005223
Fe22-7b	0.214432	0.253844	0.191618	0.492255	0.005223
Ti23-2a	0.960321	0.500841	0.094806	0.455650	0.005223
Fe23-2a	0.039679	0.500841	0.094806	0.455650	0.005223
Ti23-2b	0.960321	0.500841	0.094806	0.455650	0.005223
Fe23-2b	0.039679	0.500841	0.094806	0.455650	0.005223
01-1a	1	0.000226	0.769448	0.565185	0.010182
01-1b	1	0.750226	0.019448	0.565185	0.010182
01-2a	1	0.999299	0.841037	0.529709	0.010182
01-2b	1	0.749299	0.091037	0.529709	0.010182
01-7a	1	0.000431	0.194392	0.447539	0.010182
01-7b	1	0.750431	0.444392	0.447539	0.010182
01-8a	1	0.999693	0.268035	0.444580	0.010182
01-8b	1	0.749693	0.518035	0.444580	0.010182
01-9a	1	0.001163	0.341860	0.430487	0.010182

Continued on next page ...

Table B.3: Continued from previous page

Atom	occupancy	x	y	z	U_{iso}^{eq} (\AA^2)
01-9b	1	0.751163	0.591860	0.430487	0.010182
01-14a	1	0.999170	0.696578	0.561768	0.010182
01-14b	1	0.749170	0.946578	0.561768	0.010182
02-1a	1	0.217485	0.784564	0.218523	0.009525
02-1b	1	0.967485	0.034564	0.218523	0.009525
02-2a	1	0.236132	0.859210	0.195897	0.009525
02-2b	1	0.986132	0.109210	0.195897	0.009525
02-7a	1	0.765123	0.179823	0.792714	0.009525
02-7b	1	0.505123	0.429823	0.792714	0.009525
02-8a	1	0.780648	0.252052	0.778173	0.009525
02-8b	1	0.530648	0.502052	0.778173	0.009525
02-9a	1	0.790552	0.326547	0.779093	0.009525
02-9b	1	0.540552	0.576547	0.779093	0.009525
02-13a	1	0.236747	0.637035	0.184967	0.009525
02-13b	1	0.986747	0.887035	0.184967	0.009525
02-14a	1	0.220639	0.710214	0.224094	0.009525
02-14b	1	0.970639	0.960214	0.224094	0.009525
03-1a	1	0.781927	0.784482	0.216853	0.009187
03-1b	1	0.531927	0.034482	0.216853	0.009187
03-2a	1	0.766353	0.857878	0.189535	0.009187
03-2b	1	0.516353	0.107878	0.189535	0.009187
03-7a	1	0.234815	0.179711	0.795257	0.009187
03-7b	1	0.984815	0.429711	0.795257	0.009187
03-8a	1	0.219097	0.252437	0.779501	0.009187
03-8b	1	0.969097	0.502437	0.779501	0.009187
03-9a	1	0.210154	0.327066	0.783683	0.009187
03-9b	1	0.960154	0.577066	0.783683	0.009187
03-13a	1	0.763554	0.635611	0.172558	0.009187
03-13b	1	0.513554	0.885611	0.172558	0.009187

Continued on next page ...

Table B.3: Continued from previous page

Atom	occupancy	x	y	z	U_{iso}^{eq} (\AA^2)
03-14a	1	0.780393	0.709935	0.222909	0.009187
03-14b	1	0.530393	0.959935	0.222909	0.009187

Table B.4: Anisotropic atomic displacement parameters of the atoms of the superstructure of $La_6(Ti_{0.67}Fe_{0.33})_6O_{20}$ ($n = 6$) at temperature $T = 320$ K.

Atom	U_{11} (\AA^2)	U_{22} (\AA^2)	U_{33} (\AA^2)	U_{12} (\AA^2)	U_{13} (\AA^2)	U_{23} (\AA^2)
La1-1a	0.004943	0.014368	0.005790	-0.000147	0.000042	-0.001641
La1-1b	0.004943	0.014368	0.005790	-0.000147	0.000042	-0.001641
La1-7a	0.004378	0.013263	0.008467	0.000322	-0.000097	-0.002306
La1-7b	0.004378	0.013263	0.008467	0.000322	-0.000097	-0.002306
La1-8a	0.005155	0.012158	0.005483	0.000117	0.000229	-0.000872
La1-8b	0.005155	0.012158	0.005483	0.000117	0.000229	-0.000872
La1-14a	0.003212	0.011882	0.005903	0.000059	-0.000427	-0.001724
La1-14b	0.003212	0.011882	0.005903	0.000059	-0.000427	-0.001724
La2-2a	0.003159	0.016855	0.005359	-0.000205	-0.000798	-0.002036
La2-2b	0.003159	0.016855	0.005359	-0.000205	-0.000798	-0.002036
La3-9a	0.003308	0.027613	0.013253	-0.000147	-0.000097	-0.007125
La3-9b	0.003308	0.027613	0.013253	-0.000147	-0.000097	-0.007125
Ti11-1a	0.004552	0.009118	0.002903	-0.002462	-0.001710	0.000000
Fe11-1a	0.004552	0.009118	0.002903	-0.002462	-0.001710	0.000000
Ti11-1b	0.004552	0.009118	0.002903	-0.002462	-0.001710	0.000000
Fe11-1b	0.004552	0.009118	0.002903	-0.002462	-0.001710	0.000000
Ti12-7a	0.004552	0.009118	0.002903	-0.002462	-0.001710	0.000000
Fe12-7a	0.004552	0.009118	0.002903	-0.002462	-0.001710	0.000000
Ti12-7b	0.004552	0.009118	0.002903	-0.002462	-0.001710	0.000000
Fe12-7b	0.004552	0.009118	0.002903	-0.002462	-0.001710	0.000000
Ti13-1a	0.004552	0.009118	0.002903	-0.002462	-0.001710	0.000000

Continued on next page ...

Table B.4: Continued from previous page

Atom	U_{11} (\AA^2)	U_{22} (\AA^2)	U_{33} (\AA^2)	U_{12} (\AA^2)	U_{13} (\AA^2)	U_{23} (\AA^2)
Fe13-1a	0.004552	0.009118	0.002903	-0.002462	-0.001710	0.000000
Ti13-1b	0.004552	0.009118	0.002903	-0.002462	-0.001710	0.000000
Fe13-1b	0.004552	0.009118	0.002903	-0.002462	-0.001710	0.000000
Ti21-1a	0.004151	0.008842	0.002677	-0.002579	-0.001514	0.000519
Fe21-1a	0.004151	0.008842	0.002677	-0.002579	-0.001514	0.000519
Ti21-1b	0.004151	0.008842	0.002677	-0.002579	-0.001514	0.000519
Fe21-1b	0.004151	0.008842	0.002677	-0.002579	-0.001514	0.000519
Ti22-7a	0.004151	0.008842	0.002677	-0.002579	-0.001514	0.000519
Fe22-7a	0.004151	0.008842	0.002677	-0.002579	-0.001514	0.000519
Ti22-7b	0.004151	0.008842	0.002677	-0.002579	-0.001514	0.000519
Fe22-7b	0.004151	0.008842	0.002677	-0.002579	-0.001514	0.000519
Ti23-1a	0.004151	0.008842	0.002677	-0.002579	-0.001514	0.000519
Fe23-1a	0.004151	0.008842	0.002677	-0.002579	-0.001514	0.000519
Ti23-1b	0.004151	0.008842	0.002677	-0.002579	-0.001514	0.000519
Fe23-1b	0.004151	0.008842	0.002677	-0.002579	-0.001514	0.000519
01-1a	0.001377	0.017684	0.011484	0.000498	-0.000238	0.000395
01-1b	0.001377	0.017684	0.011484	0.000498	-0.000238	0.000395
01-2a	0.001377	0.017684	0.011484	0.000498	-0.000238	0.000395
01-2b	0.001377	0.017684	0.011484	0.000498	-0.000238	0.000395
01-7a	0.001377	0.017684	0.011484	0.000498	-0.000238	0.000395
01-7b	0.001377	0.017684	0.011484	0.000498	-0.000238	0.000395
01-8a	0.001377	0.017684	0.011484	0.000498	-0.000238	0.000395
01-8b	0.001377	0.017684	0.011484	0.000498	-0.000238	0.000395
01-9a	0.001377	0.017684	0.011484	0.000498	-0.000238	0.000395
01-9b	0.001377	0.017684	0.011484	0.000498	-0.000238	0.000395
01-14a	0.001377	0.017684	0.011484	0.000498	-0.000238	0.000395
01-14b	0.001377	0.017684	0.011484	0.000498	-0.000238	0.000395
02-1a	0.009206	0.015474	0.003896	-0.001436	-0.000046	0.002804
02-1b	0.009206	0.015474	0.003896	-0.001436	-0.000046	0.002804

Continued on next page ...

Table B.4: Continued from previous page

Atom	U_{11} (\AA^2)	U_{22} (\AA^2)	U_{33} (\AA^2)	U_{12} (\AA^2)	U_{13} (\AA^2)	U_{23} (\AA^2)
02-2a	0.009206	0.015474	0.003896	-0.001436	-0.000046	0.002804
02-2b	0.009206	0.015474	0.003896	-0.001436	-0.000046	0.002804
02-7a	0.009206	0.015474	0.003896	-0.001436	-0.000046	0.002804
02-7b	0.009206	0.015474	0.003896	-0.001436	-0.000046	0.002804
02-8a	0.009206	0.015474	0.003896	-0.001436	-0.000046	0.002804
02-8b	0.009206	0.015474	0.003896	-0.001436	-0.000046	0.002804
02-9a	0.009206	0.015474	0.003896	-0.001436	-0.000046	0.002804
02-9b	0.009206	0.015474	0.003896	-0.001436	-0.000046	0.002804
02-13a	0.009206	0.015474	0.003896	-0.001436	-0.000046	0.002804
02-13b	0.009206	0.015474	0.003896	-0.001436	-0.000046	0.002804
02-14a	0.009206	0.015474	0.003896	-0.001436	-0.000046	0.002804
02-14b	0.009206	0.015474	0.003896	-0.001436	-0.000046	0.002804
03-1a	0.008152	0.014092	0.005316	-0.000557	0.000833	0.002638
03-1b	0.008152	0.014092	0.005316	-0.000557	0.000833	0.002638
03-2a	0.008152	0.014092	0.005316	-0.000557	0.000833	0.002638
03-2b	0.008152	0.014092	0.005316	-0.000557	0.000833	0.002638
03-7a	0.008152	0.014092	0.005316	-0.000557	0.000833	0.002638
03-7b	0.008152	0.014092	0.005316	-0.000557	0.000833	0.002638
03-8a	0.008152	0.014092	0.005316	-0.000557	0.000833	0.002638
03-8b	0.008152	0.014092	0.005316	-0.000557	0.000833	0.002638
03-9a	0.008152	0.014092	0.005316	-0.000557	0.000833	0.002638
03-9b	0.008152	0.014092	0.005316	-0.000557	0.000833	0.002638
03-13a	0.008152	0.014092	0.005316	-0.000557	0.000833	0.002638
03-13b	0.008152	0.014092	0.005316	-0.000557	0.000833	0.002638
03-14a	0.008152	0.014092	0.005316	-0.000557	0.000833	0.002638
03-14a	0.008152	0.014092	0.005316	-0.000557	0.000833	0.002638

B.2 Site occupancy factors of Fe^{3+}

The Ti/Fe ratios on all six crystallographically independent B sites were refined without any further restrictions than the fixing of the sum of occupancies at each site to 1.

Fe^{3+} occupancies in $La_5(Ti_{0.80}Fe_{0.20})_5O_{17}$

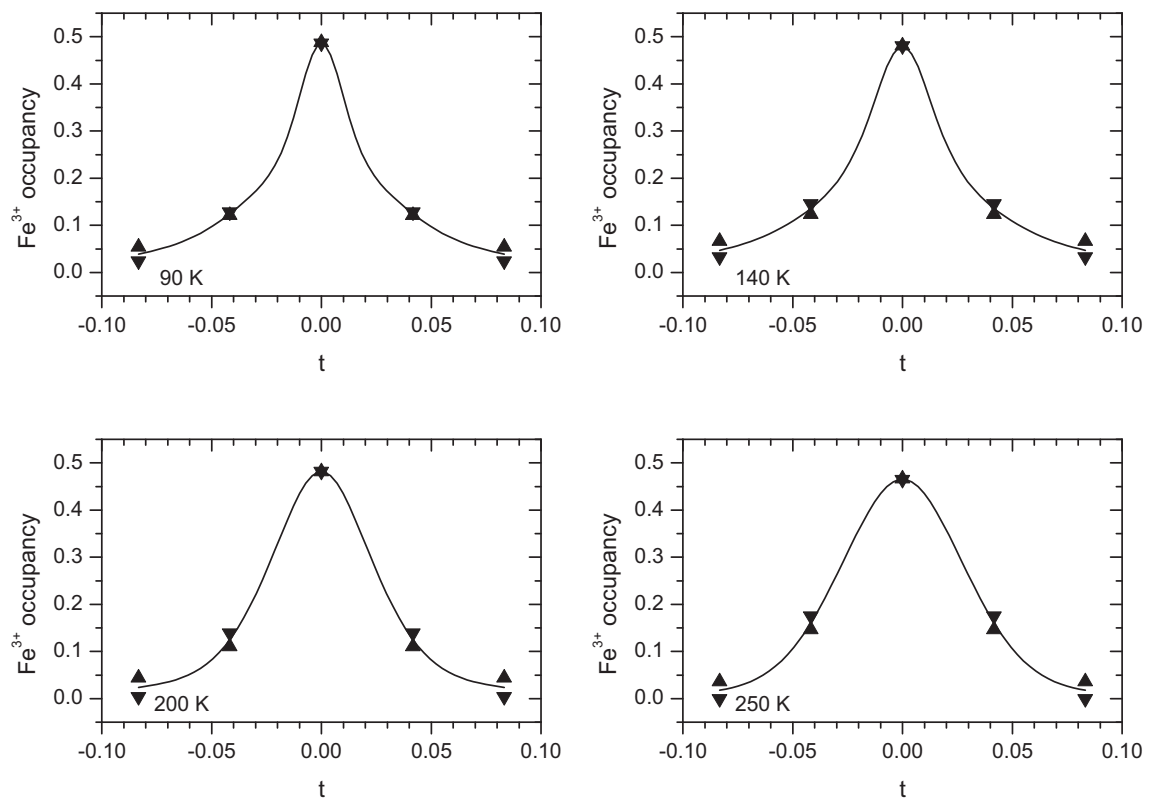


Figure B.1: Site occupancy factors of Fe^{3+} as function of t . The curves are obtained by fits of Pseudo-Voigt functions centered at $t = 0$ to the data points. Triangles pointing up represent occupancies in one row along the \mathbf{b} -axis, while the triangles pointing down refer to those of a second row displaced by $\mathbf{a}/2$. Shown are occupancies at the temperatures 90, 150, 200 and 250 K.

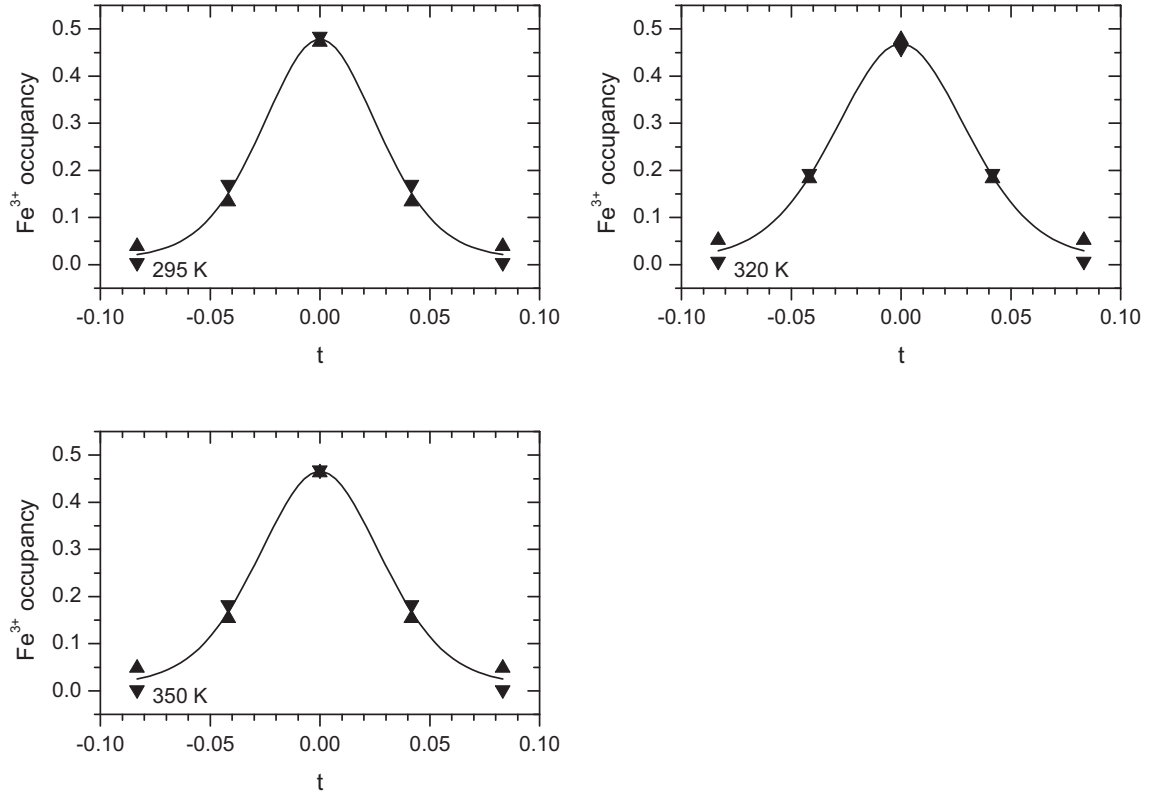


Figure B.2: Site occupancy factors of Fe^{3+} as function of t . The curves are obtained by fits of Pseudo-Voigt functions centered at $t = 0$ to the data points. Triangles pointing up represent occupancies in one row along the \mathbf{b} -axis, while the triangles pointing down refer to those of a second row displaced by $\mathbf{a}/2$. Shown are occupancies at the temperatures 295, 320 and 350 K.

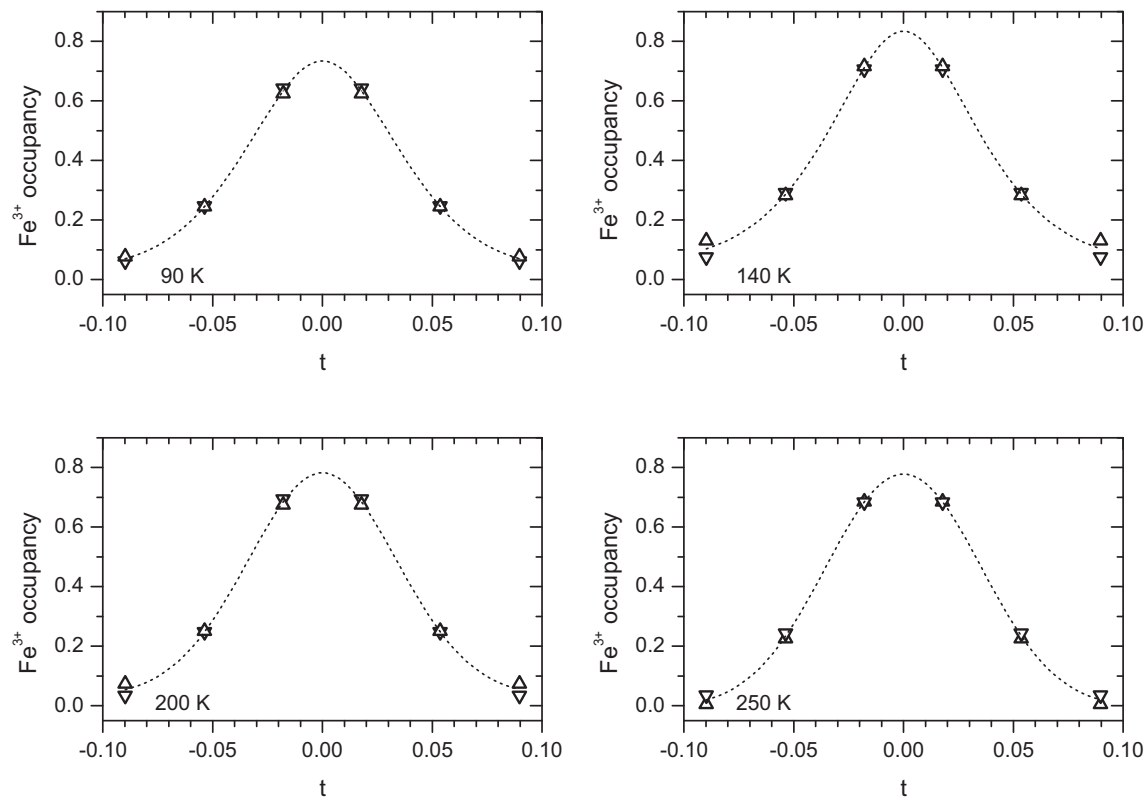
Fe^{3+} occupancies in $La_6(Ti_{0.67}Fe_{0.33})_6O_{20}$ 

Figure B.3: Site occupancy factors of Fe^{3+} as function of t . The curves are obtained by fits of Pseudo-Voigt functions centered at $t = 0$ to the data points. Triangles pointing up represent occupancies in one row along the \mathbf{b} -axis, while the triangles pointing down refer to those of a second row displaced by $\mathbf{a}/2$. Shown are occupancies at the temperatures 90, 140, 200 and 250 K.

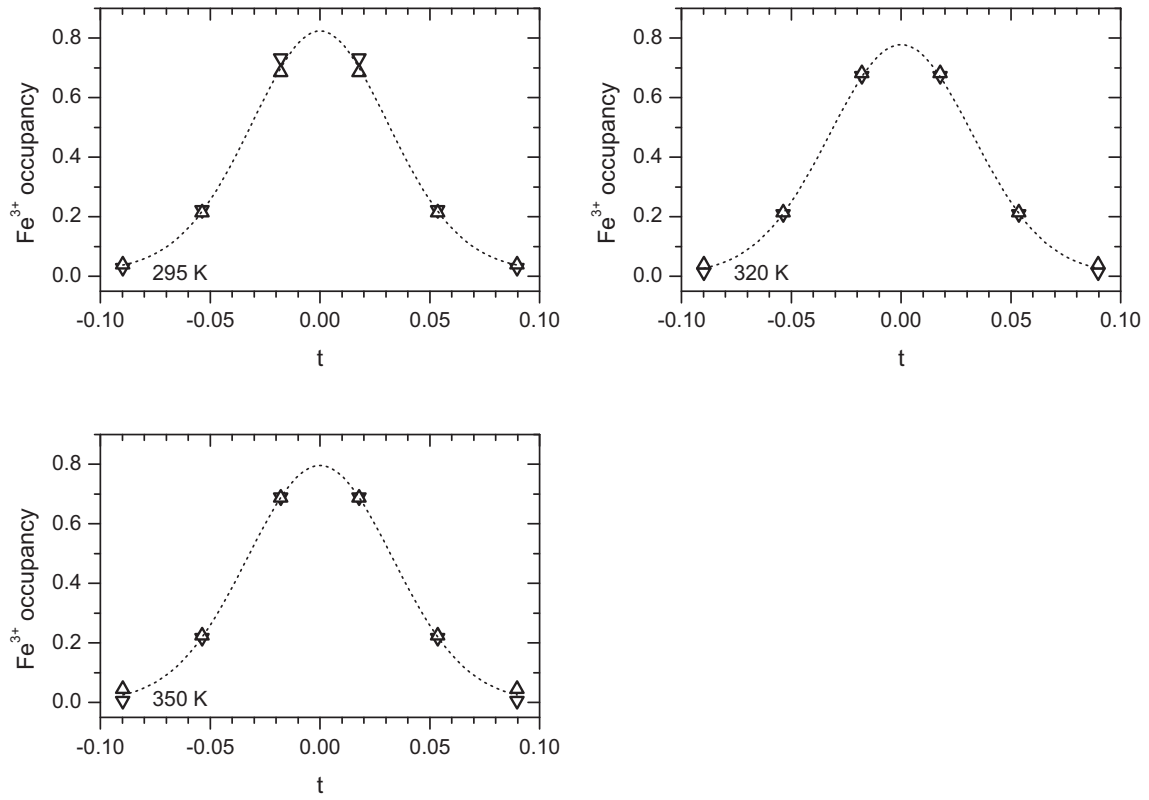


Figure B.4: Site occupancy factors of Fe^{3+} as function of t . The curves are obtained by fits of Pseudo-Voigt functions centered at $t = 0$ to the data points. Triangles pointing up represent occupancies in one row along the \mathbf{b} -axis, while the triangles pointing down refer to those of a second row displaced by $\mathbf{a}/2$. Shown are occupancies at the temperatures 90, 150, 200 and 250 K.

B.3 Distortion of the (Ti,Fe)O₆ octahedra

The distortion of the (Ti,Fe)O₆ octahedra can be visualized by help of the distortion index as defined in Lichtenberg et al. (2008) and used in chapter 7.

Distortions in La₅(Ti_{0.80}Fe_{0.20})₅O₁₇

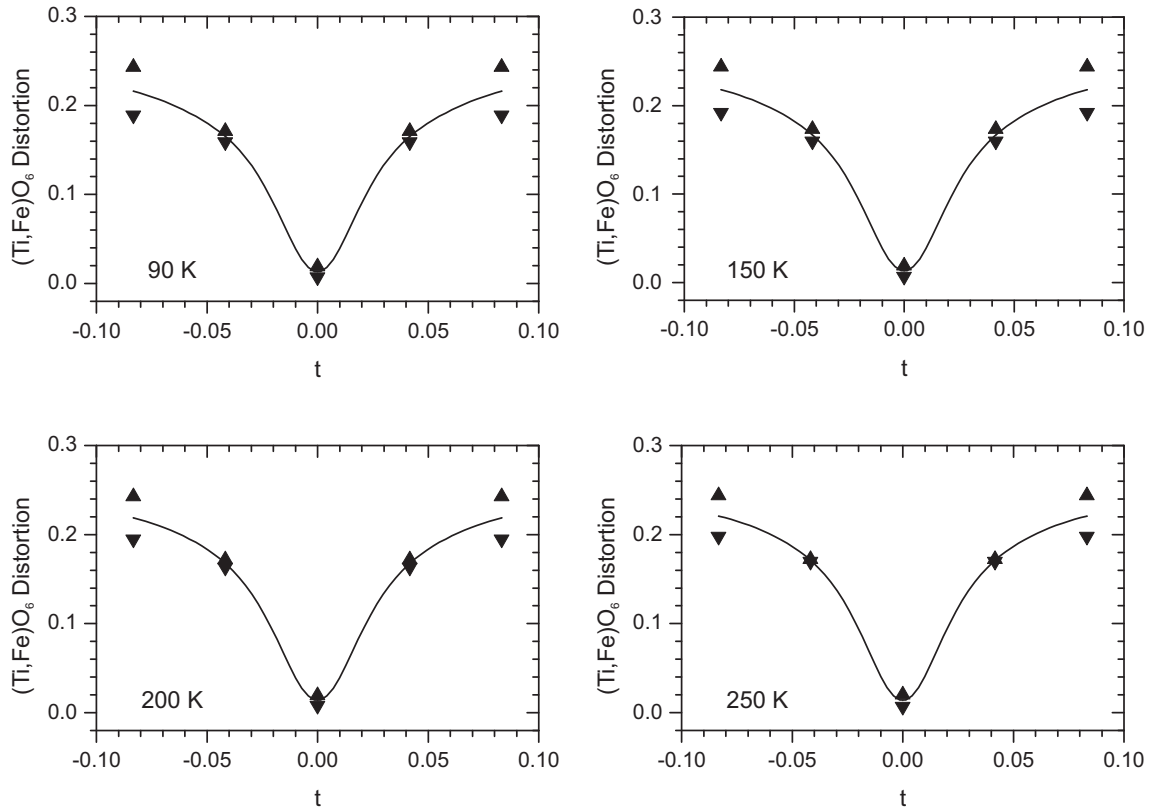


Figure B.5: (Ti,Fe)O₆ octahedra distortions as function of t . Triangles pointing up represent distortions in one row along the \mathbf{b} -axis, while the triangles pointing down refer to those of a second row displaced by $\mathbf{a}/2$. Shown are the distortion indices at the temperatures 90, 150, 200 and 250 K. Outlined curves are obtained by fits to the data of Pseudo-Voigt functions centered at $t = 0$.

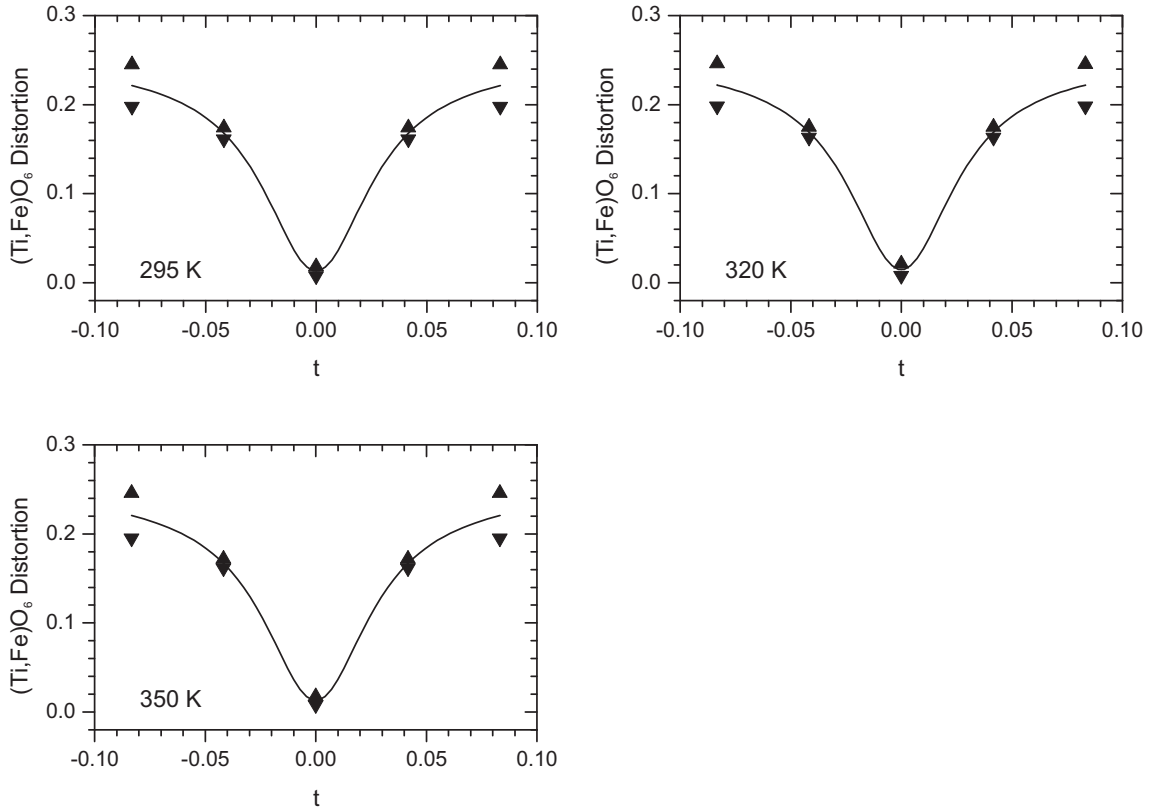


Figure B.6: $(\text{Ti,Fe})\text{O}_6$ octahedra distortions as function of t . Triangles pointing up represent distortions in one row along the \mathbf{b} -axis, while the triangles pointing down refer to those of a second row displaced by $\mathbf{a}/2$. Shown are the distortion indices at the temperatures 295, 320 and 350 K. Outlined curves are obtained by fits to the data of Pseudo-Voigt functions centered at $t = 0$.

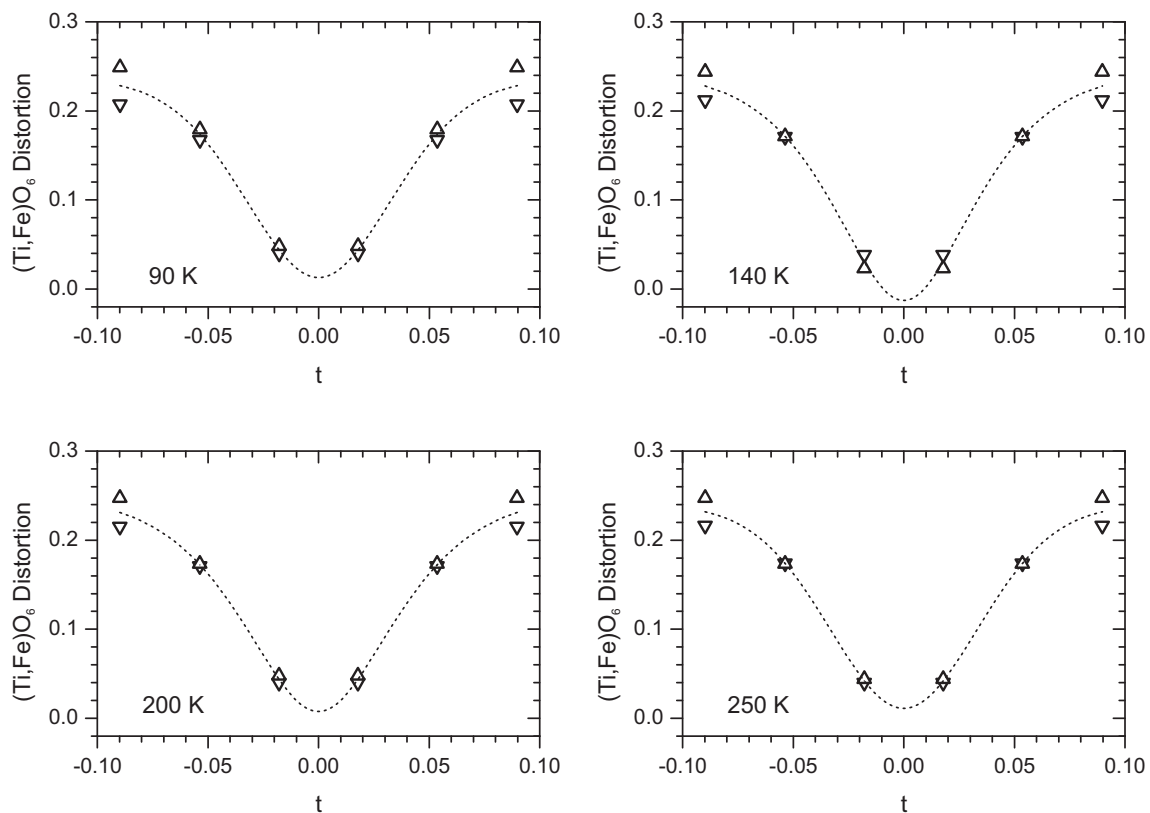
Distortions in La₆(Ti_{0.67}Fe_{0.33})₆O₂₀

Figure B.7: (Ti,Fe)O₆ octahedra distortions as function of t . Triangles pointing up represent distortions in one row along the \mathbf{b} -axis, while the triangles pointing down refer to those of a second row displaced by $\mathbf{a}/2$. Shown are the distortion indices at the temperatures 90, 140, 200 and 250 K. Outlined curves are obtained by fits to the data of Pseudo-Voigt functions centered at $t = 0$.

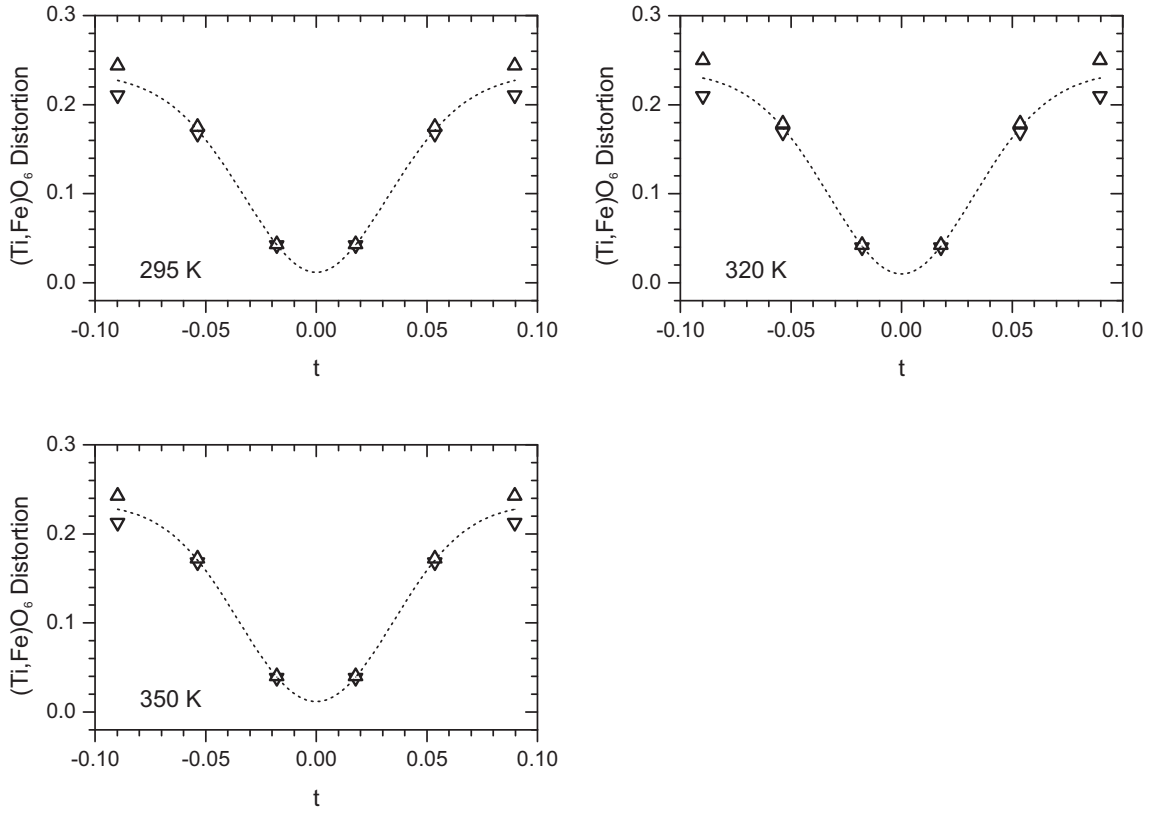


Figure B.8: $(\text{Ti,Fe})\text{O}_6$ octahedra distortions as function of t . Triangles pointing up represent distortions in one row along the \mathbf{b} -axis, while the triangles pointing down refer to those of a second row displaced by $\mathbf{a}/2$. Shown are the distortion indices at the temperatures 295, 320 and 350 K. Dotted curves are obtained by fits to the data of Pseudo-Voigt functions centered at $t = 0$.

B.4 Variation of the (Ti,Fe)–O distances

The increasing distortion of the (Ti,Fe)O₆ octahedra in the direction from the centers to the borders of the slabs is also visible in the increasing spread of the six (Ti,Fe)–O distances in each of the five octahedra in a slab.

Distances in octahedra of La₅(Ti_{0.80}Fe_{0.20})₅O₁₇

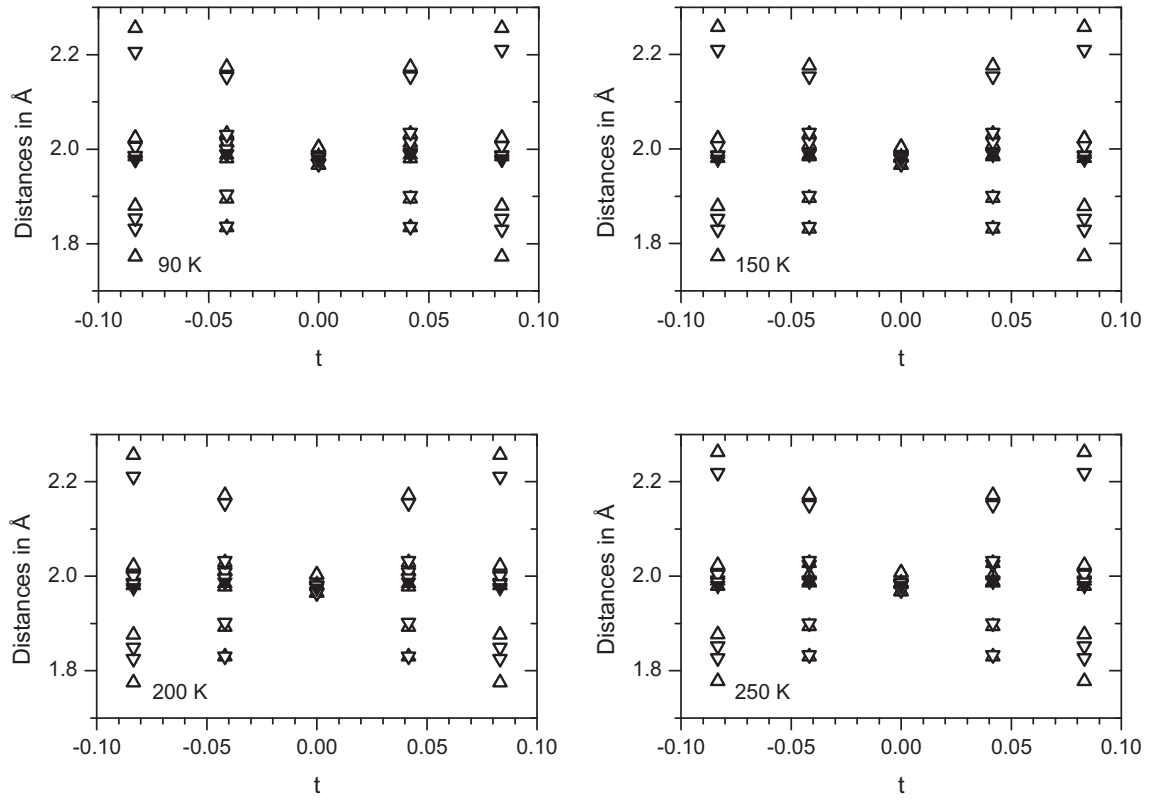


Figure B.9: Distances between (Ti,Fe) and O in the octahedra as function of t . Open symbols denote individual distances, while filled symbols represent the average (Ti,Fe)–O distance in each of the octahedra. Triangles pointing up represent distances in octahedra in one row along the \mathbf{b} -axis, while the triangles pointing down refer to those of a second row displaced by $\mathbf{a}/2$. Shown are distances at the temperatures 90, 150, 200 and 250 K.

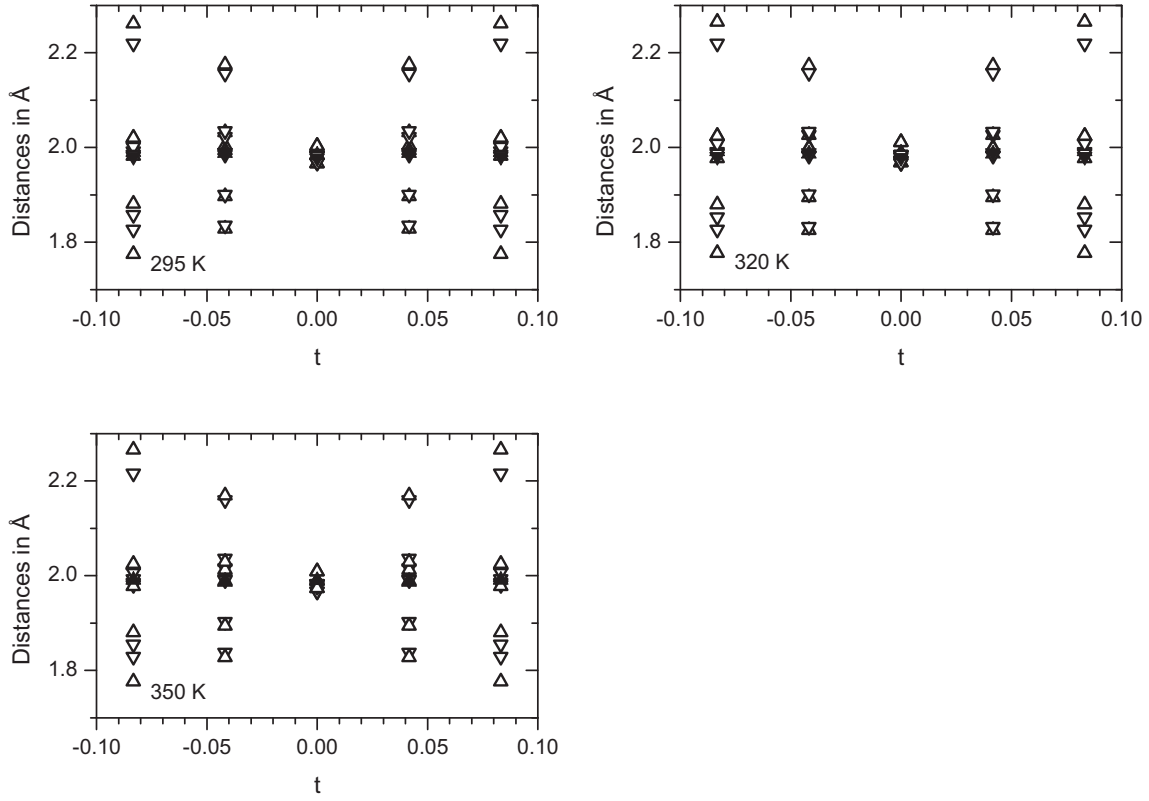


Figure B.10: Distances between (Ti,Fe) and O in the octahedra as function of t . Open symbols denote individual distances, while filled symbols represent the average (Ti,Fe)–O distance in each of the octahedra. Triangles pointing up represent distances in octahedra in one row along the \mathbf{b} -axis, while the triangles pointing down refer to those of a second row displaced by $\mathbf{a}/2$. Shown are distances at the temperatures 295, 320 and 350 K.

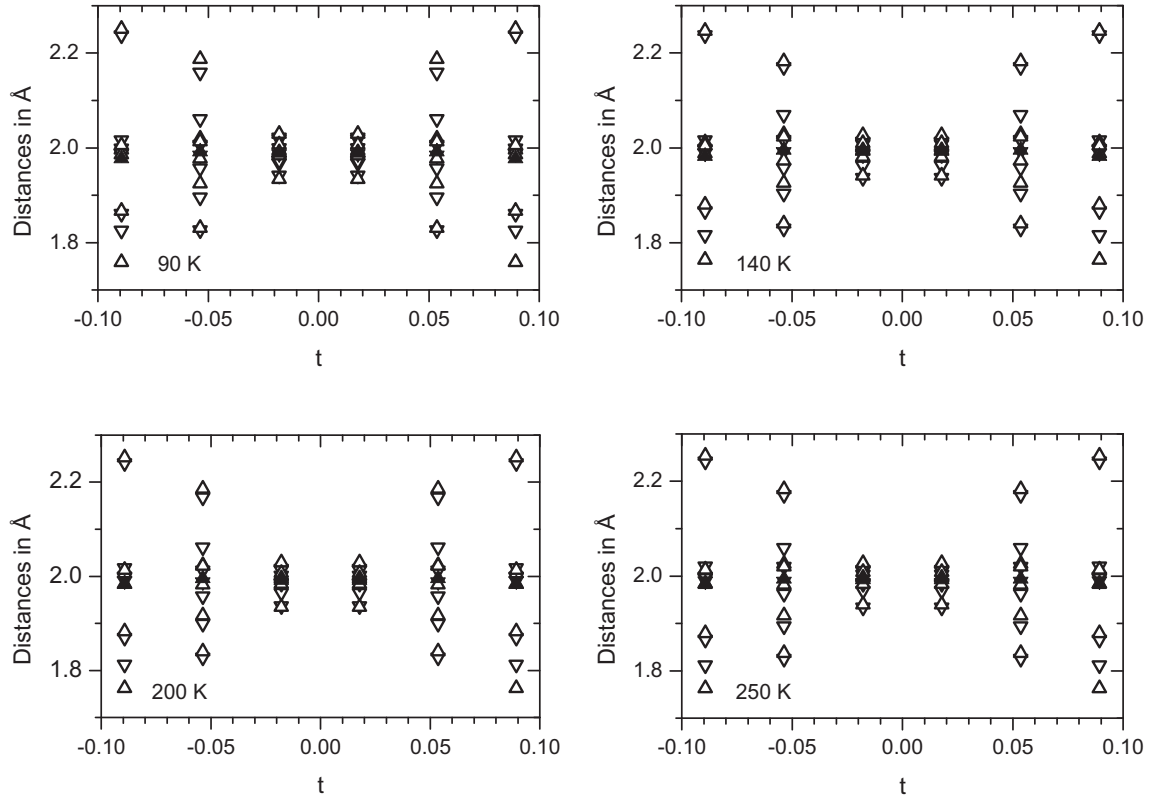
Distances in octahedra of $\text{La}_6(\text{Ti}_{0.67}\text{Fe}_{0.33})_6\text{O}_{20}$ 

Figure B.11: Distances between (Ti,Fe) and O in the octahedra as function of t . Open symbols denote individual distances, while filled symbols represent the average (Ti,Fe)–O distance in each of the octahedra. Triangles pointing up represent distances in octahedra in one row along the \mathbf{b} -axis, while the triangles pointing down refer to those of a second row displaced by $\mathbf{a}/2$. Shown are distances at the temperatures 90, 140, 200 and 250 K.

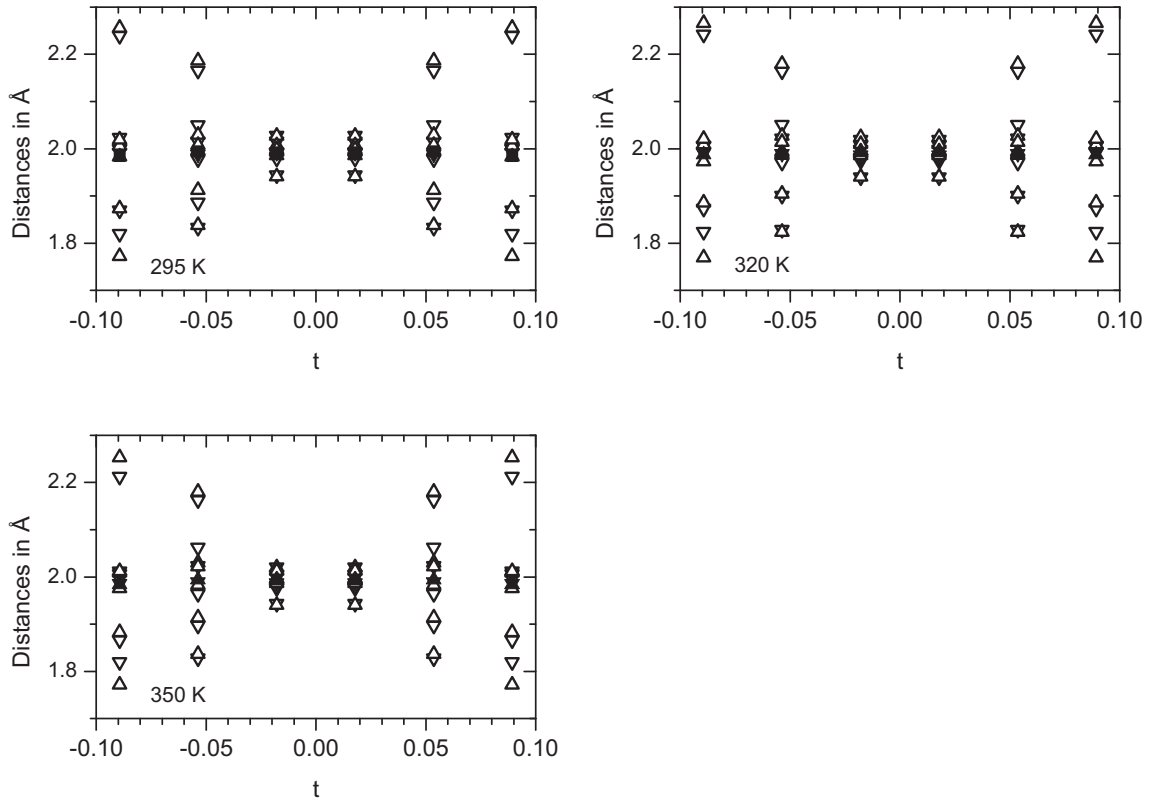


Figure B.12: Distances between (Ti,Fe) and O in the octahedra as function of t . Open symbols denote individual distances, while filled symbols represent the average (Ti,Fe)–O distance in each of the octahedra. Triangles pointing up represent distances in octahedra in one row along the \mathbf{b} -axis, while the triangles pointing down refer to those of a second row displaced by $\mathbf{a}/2$. Shown are distances at the temperatures 295, 320 and 350 K.

B.5 Bond valences sums (BVS) of Ti and Fe

The BVS parameters have been obtained from Brese and O'Keeffe (1991). BVS were calculated based on the atomic distances of the superstructures obtained by transforming the refined superspace model to the corresponding superstructure. BVS parameters used in the calculations are: $R_{Ti,O} = 1.815$ and $R_{Fe,O} = 1.759$.

Valences in $\text{La}_5(\text{Ti}_{0.80}\text{Fe}_{0.20})_5\text{O}_{17}$

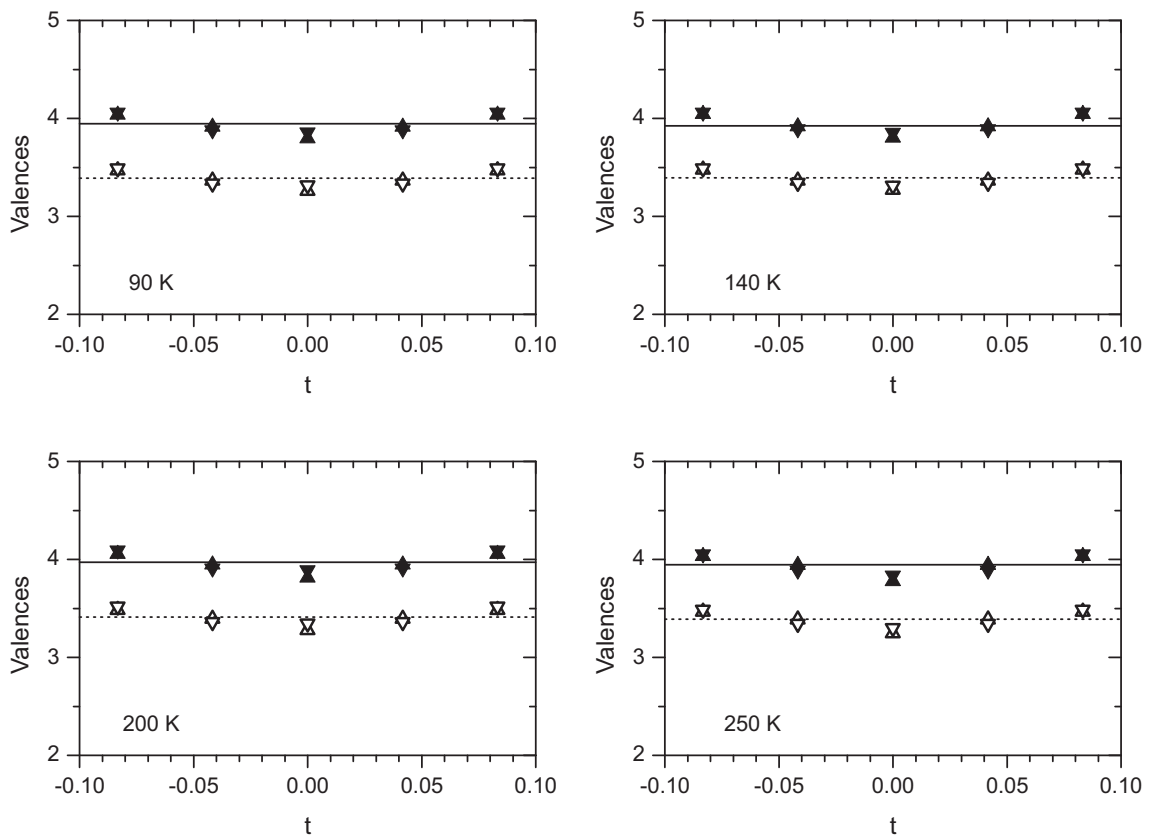


Figure B.13: Calculated valences for Ti (filled) and Fe (open symbol) as function of t . Triangles pointing up represent occupancies in one row along the \mathbf{b} -axis, while the triangles pointing down refer to those of a second row displaced by $\mathbf{a}/2$. The solid and dashed lines represent the average valences at each temperature for Ti and Fe: 3.94 (4), 3.39 (4) (90 K); 3.95 (4), 3.40 (4) (150 K); 3.97 (4), 3.41 (4) (200 K); 3.94 (5), 3.39 (4) (250 K).

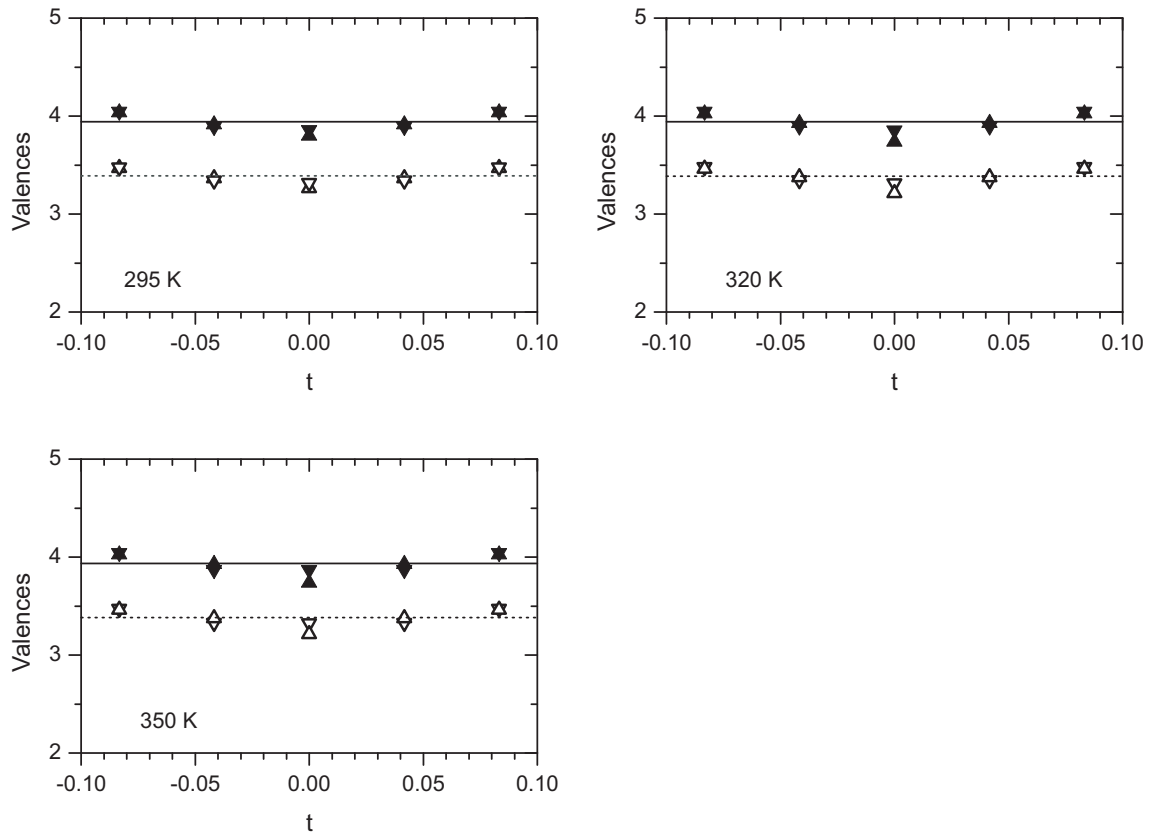


Figure B.14: Calculated valences for Ti (filled) and Fe (open symbol) as function of t . Triangles pointing up represent occupancies in one row along the \mathbf{b} -axis, while the triangles pointing down refer to those of a second row displaced by $\mathbf{a}/2$. The solid and dashed lines represent the average valences at each temperature for Ti and Fe: 3.94 (4), 3.39 (4) (295 K); 3.94 (4), 3.39 (4) (320 K); 3.93 (4), 3.38 (4) (350 K).

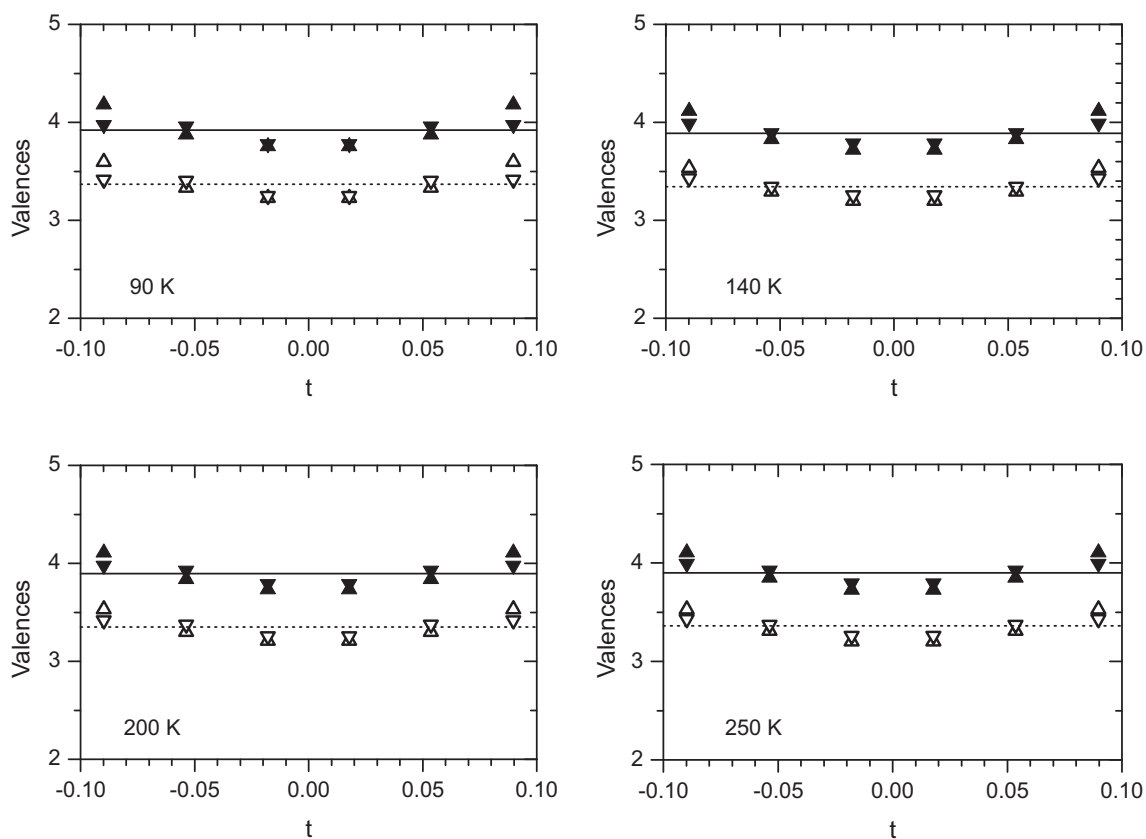
Valences in $\text{La}_6(\text{Ti}_{0.67}\text{Fe}_{0.33})_6\text{O}_{20}$ 

Figure B.15: Calculated valences for Ti (filled) and Fe (open symbol) as function of t . Triangles pointing up represent occupancies in one row along the \mathbf{b} -axis, while the triangles pointing down refer to those of a second row displaced by $\mathbf{a}/2$. The solid and dashed lines represent the average valences at each temperature for Ti and Fe: 3.92 (6), 3.37 (5) (90 K); 3.89 (6), 3.34 (5) (140 K); 3.90 (5), 3.35 (4) (200 K); 3.90 (5), 3.35 (5) (250 K).

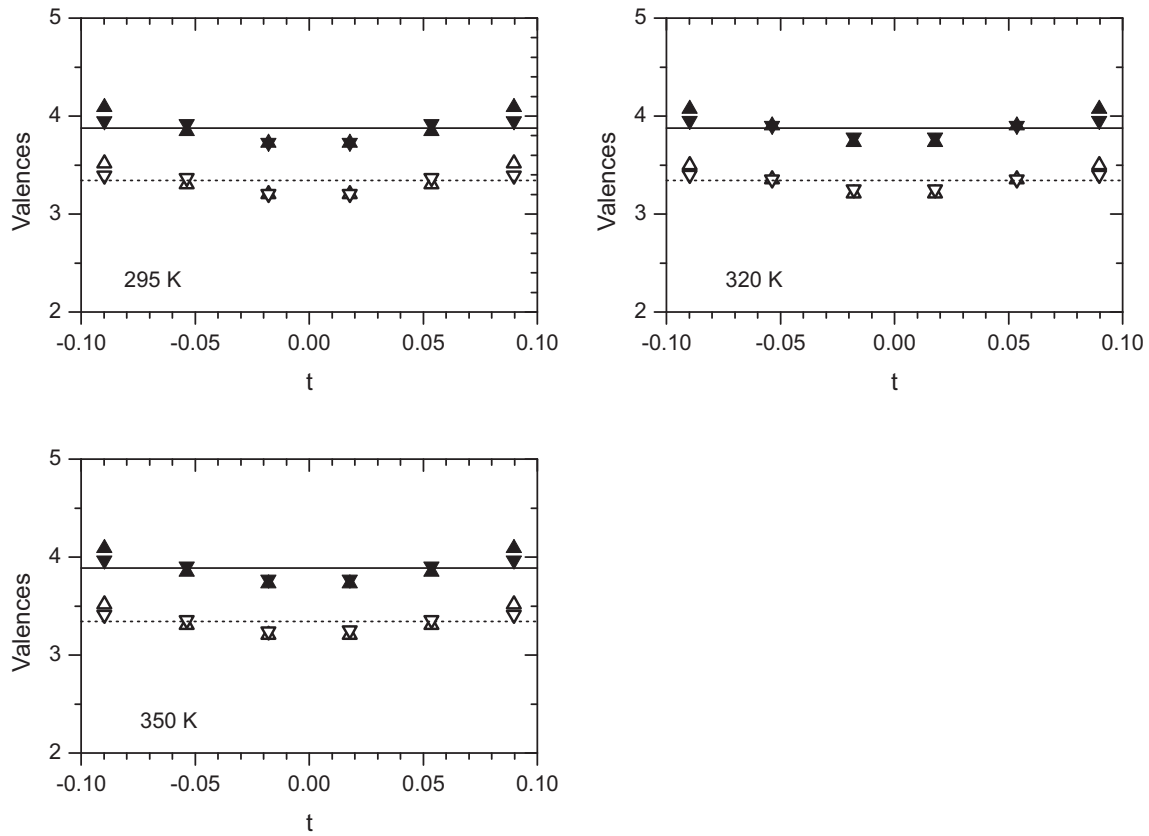


Figure B.16: Calculated valences for Ti (filled) and Fe (open symbol) as function of t . Triangles pointing up represent occupancies in one row along the \mathbf{b} -axis, while the triangles pointing down refer to those of a second row displaced by $\mathbf{a}/2$. The solid and dashed lines represent the average valences at each temperature for Ti and Fe: 3.88 (5), 3.33 (5) (295 K); 3.89 (5), 3.34 (4) (320 K); 3.89 (5), 3.34 (4) (350 K).

Bibliography

- Abrahams, S. C., Schmalke, H. W., Williams, T., Reller, A., Lichtenberg, F., Widmer, D., Bednorz, J. G., Spreiter, R., Bosshard, C. and Gunter, P. (1998). Centrosymmetric or noncentrosymmetric? Case study, generalization and structural redetermination of $\text{Sr}_5\text{Nb}_5\text{O}_{17}$, *Acta Crystallogr. B* **54**: 399–416.
- Angelkort, J., Woelfel, A., Schoenleber, A., van Smaalen, S. and Kremer, R. K. (2009). Observation of strong magnetoelastic coupling in a first-order phase transition of CrOCl , *Phys. Rev. B* **80**(14): 144416.
- Bailey, A. C. and Yates, B. (1970). Anisotropic thermal expansion of pyrolytic graphite at low temperatures, *J. Appl. Phys.* **41**(13): 5088–5091.
- Becker, B., Patil, N. G., Ramakrishnan, S., Menovsky, A. A., Nieuwenhuys, G. J. and Mydosh, J. A. (1999). Strongly coupled charge-density wave transition in single-crystal $\text{Lu}_5\text{Ir}_4\text{Si}_{10}$, *Phys. Rev. B* **59**: 7266–7269.
- Blundell, S. (2001). *Magnetism in Condensed Matter*, Oxford Master Series in Condensed Matter Physics, Oxford University Press, Oxford.
- Bodak, O. I. and Marusin, E. P. (1979). The crystal structure of $R\text{NiC}_2$ compounds ($R = \text{Ce}, \text{La}, \text{Pr}$), *Dokl. Akad. Nauk Ukr. S. S. R. Ser. A* **12**: 1048.
- Bodak, O. I., Marusin, E. P. and Bruskov, V. A. (1980). Crystal structure of the compound $R\text{CoC}_2$ ($R = \text{Ce}, \text{La}, \text{Pr}$), *Kristallogr.* **25**(3): 617–619.
- Brandon, J. K. and Megaw, H. D. (1970). On the crystal structure and properties of $\text{Ca}_2\text{Nb}_2\text{O}_7$ “calcium pyroniobate”, *Phil. Mag.* **21**: 189–194.
- Brese, N. and O’Keeffe, M. (1991). Bond-valence parameters for solids, *Acta Cryst. B* **47**(Part 2): 192–197.

- Brown, I. D. (2002). *The Chemical Bond in Inorganic Chemistry, The Bond Valence Method*, Oxford University Press, Oxford.
- Canales-Vazquez, J., Irvine, J. T. and Zhou, W. (2004). Synthesis and characterization of n=5, 6 members of the $\text{La}_4\text{Sr}_{n-4}\text{Ti}_n\text{O}_{3n+2}$ series with layered structure based upon perovskite, *J Solid State Chem* **177**(6): 2039 – 2043.
- Cava, R. J. and Roth, R. (1981). The structure of LaTaO_4 at 300° C by neutron powder profile analysis, *J. Solid State Chem.* **36**(2): 139–147.
- Cowley, R. A., Birgeneau, R. J., Shirane, G., Guggenheim, H. J. and Ikeda, H. (1980). Spin fluctuations in random magnetic nonmagnetic two-dimensional anti-ferromagnets .3. an ising system, *Phys. Rev. B* **21**(9): 4038–4048.
- Cwik, M., Lorenz, T., Baier, J., Müller, R., André, G., Bourée, F., Lichtenberg, F., Freimuth, A., Schmitz, R., Müller-Hartmann, E. and Braden, M. (2003). Crystal and magnetic structure of LaTiO_3 : Evidence for nondegenerate t_{2g} orbitals, *Phys. Rev. B* **68**: 060401.
- Daniels, P., Lichtenberg, F. and van Smaalen, S. (2003). Perovskite-related $\text{LaTiO}_{3.41}$, *Acta. Cryst. C* **59**: I15–I17.
- Daniels, P., Tamazyan, R., Kuntscher, C. A., Dressel, M., Lichtenberg, F. and van Smaalen, S. (2002). The incommensurate modulation of the structure of $\text{Sr}_2\text{Nb}_2\text{O}_7$, *Acta Cryst. B* **58**: 970–976.
- Drews, A. R., Wong-Ng, W., Roth, R. S. and Vanderah, T. A. (1996). Preparation and crystal structure of $\text{Sr}_5\text{TiNb}_4\text{O}_{17}$, *Mater. Res. Bull.* **31**: 153–162.
- Duisenberg, A. J. M. (1992). Indexing in single-crystal diffractometry with an obstinate list of reflections, *J. Appl. Crystallogr.* **25**(Part 2): 92–96.
- Eichhorn, K. D. (1993). *DIF4 4-Circle Diffractometer (HASYLAB Beamline D3) Users Guide Version 2.1*, Institut für Kristallographie, Karlsruhe.
- Ekin, J. W. (2006). *Experimental techniques for low-temperature measurements: cryostat design, material properties, and superconductor critical-current testing*, Oxford University Press, Oxford.

- Elcoro, L., Zuniga, F. J. and Perez-Mato, J. M. (2004). Superspace description of $\text{NaCa}_4\text{Nb}_5\text{O}_{17}$ (a perovskite-related compound of the type $A_n\text{B}_n\text{O}_{3n+2}$ as a modulated layered structure, *Acta Cryst. B* **60**: 21–31.
- Galli, F., Feyerherm, R., Hendrikx, R. W. A., Dudzik, E., Nieuwenhuys, G. J., Ramakrishnan, S., Brown, S. D., van Smaalen, S. and Mydosh, J. A. (2002). Coexistence of charge density wave and antiferromagnetism in $\text{Er}_5\text{Ir}_4\text{Si}_{10}$, *J. Phys.: Condens. Matter* **14**: 5067–5075.
- Galli, F., Ramakrishnan, S., Taniguchi, T., Nieuwenhuys, G. J., Mydosh, J. A., Geupel, S., Ludecke, J. and van Smaalen, S. (2000). Charge-density-wave transitions in the local-moment magnet $\text{Er}_5\text{Ir}_4\text{Si}_{10}$, *Phys. Rev. Lett.* **85**: 158–161.
- Giacovazzo, C., Monaco, H. L., Artioli, G., Ferraris, D. V. G., Gilli, G., Zanotti, G. and Catti, M. (2002). *Fundamentals of Crystallography*, International Union of Crystallography Texts on Crystallography, Oxford University Press, Oxford.
- Glusker, J. and Trueblood, K. (2010). *Crystal Structure Analysis: A Primer*, International Union of Crystallography Texts on Crystallography, Oxford University Press, Oxford.
- Gollwitzer, J. (2004). *Untersuchung des thermischen Verhaltens von Vanadyl-Pyrophosphat durch Röntgenbeugung*, Diplomarbeit, Universität Bayreuth.
- Gruener, G. (1994). *Density waves in solids*, Addison–Wesley, Reading, Massachusetts.
- Grüner, G. (1988). The dynamics of charge-density waves, *Rev. Mod. Phys.* **60**: 1129–1181.
- Guevarra, J., Schönleber, A., van Smaalen, S. and Lichtenberg, F. (2007). Superspace description of the crystal structures of $\text{Ca}_n(\text{Nb,Ti})_n\text{O}_{3n+2}$ ($n = 5$ and 6), *Acta Cryst. B* **63**: 183–189.
- Guevarra, J., van Smaalen, S., Daniels, P., Rotiroti, N. and Lichtenberg, F. (2005a). Perovskite-related $\text{Ca}(\text{Nb,Ti})\text{O}_{3.33}$, *Z. Kristallogr.* **220**: 19–24.
- Guevarra, J., van Smaalen, S., Rotiroti, N., Paulmann, C. and Lichtenberg, F. (2005b). Crystal structure of $\text{Ca}_5\text{Nb}_5\text{O}_{17}$, *J. Solid State Chem.* **178**: 2934–2941.

- Hase, I. and Yanagisawa, T. (2009). Electronic structure of RNiC_2 ($\text{R} = \text{La}, \text{Y},$ and Th), *J. Phys. Soc. Jpn.* **78**(8): 084724.
- Herrendorf, W. (1993). *HABITUS, ein Programm zur Optimierung der Kristallbeschreibung für die numerische Absorptionskorrektur anhand geeigneter ψ - abgetasteter Reflexe*, Universität Karlsruhe, Karlsruhe.
- Ishizawa, N., Marumo, F. and Iwai, S. (1981). Compounds with perovskite-type slabs. 4. ferroelectric phase-transitions in $\text{Sr}_2(\text{Ta}_{1-x}\text{Nb}_x)_2\text{O}_7$ ($x \lesssim 0.12$) and $\text{Sr}_2\text{Ta}_2\text{O}_7$, *Acta Cryst. B* **37**: 26–31.
- Ishizawa, N., Marumo, F., Iwai, S., Kimura, M. and Kawamura, T. (1980). Compounds with perovskite-type slabs. 3. the structure of a monoclinic modification of $\text{Ca}_2\text{Nb}_2\text{O}_7$, *Acta Cryst. B* **36**: 763–766.
- Ishizawa, N., Marumo, F., Iwai, S., Kimura, N. and Kawamura, T. (1982). Compounds with perovskite-type slabs. 5. a high-temperature modification of $\text{La}_2\text{Ti}_2\text{O}_7$, *Acta Cryst. B* **38**: 368–372.
- Ishizawa, N., Marumo, F., Kawamura, T. and Kimura, M. (1975). Crystal-structure of $\text{Sr}_2\text{Nb}_2\text{O}_7$, a compound with perovskite-type slabs, *Acta Cryst. B* **31**: 1912–1915.
- Ishizawa, N., Marumo, F., Kawamura, T. and Kimura, M. (1976). Compounds with perovskite-type slabs. 2. crystal-structure of $\text{Sr}_2\text{Ta}_2\text{O}_7$, *Acta Cryst. B* **32**: 2564–2566.
- Ispov, V. A. (1999). Crystal chemical aspects of the layered perovskite-like oxide ferroelectrics of the $\text{A}_n\text{M}_n\text{O}_{3n+2}$ type, *Ferroelectrics* **220**(1-2): 79–103.
- Janssen, T., Janner, A., Looijenga-Vos, A. and de Wolff, P. M. (2006). *International Tables for Crystallography Vol. C*, Kluwer Academic Publishers, pp. 907–955.
- Jawahar, I. N., Santha, N. I., Sebastian, M. T. and Mohanan, P. (2002). Microwave dielectric properties of $\text{MO-La}_2\text{O}_3\text{-TiO}_2$ ($M = \text{Ca}, \text{Sr}, \text{Ba}$), *J. Mater. Res.* **17**: 3084–3089.
- Jeitschko, W. and Gerss, M. (1986). Ternary carbides of the rare-earth and iron group-metals with CeCoC_2 -type and CeNiC_2 -type structure, *J. Less-Common Met.* **116**: 147–157.

- Jenkins, R., Gloud, R. W. and Gedcke, D. (1995). *Quantitative X-ray Spectrometry*, Practical spectroscopy, 2 edn, Marcel Dekker, Inc., New York.
- Jona, F., Shirane, G. and Pepinsky, R. (1955). Dielectric, x-ray, and optical study of ferroelectric $\text{Cd}_2\text{Nb}_2\text{O}_7$ and related compounds, *Phys. Rev.* **98**: 903–909.
- Klein, C. (2012). *The Mar345dtb User's Guide Version 5.5*, Marresearch GmbH, Norderstedt, Germany.
- Koshikawa, Y., Onodera, H., Kosaka, M., Yamauchi, H., Ohashi, M. and Yamaguchi, Y. (1997). Crystalline electric fields and magnetic properties of single-crystalline RNiC_2 compounds ($R=\text{Ho}$, Er and Tm), *J. Magn. Magn. Mater.* **173**(1-2): 72–82.
- Kotsanidis, P., Yagnithos, J. and Gamariseale, E. (1989). Magnetic-properties of the ternary carbides of the rare-earth and nickel group-metals, *J. Less-Common Met.* **152**(2): 287–294.
- Koval, Y., Chowdhury, F., Jin, X., Simsek, Y., Lichtenberg, F., Pentcheva, R. and Muller, P. (2011). Resistive memory switching in layered oxides: $\text{A}_n\text{B}_n\text{O}_{3n+2}$ perovskite derivatives and $\text{Bi}_2\text{Sr}_2\text{CaCu}_2\text{O}_{8+\delta}$ high- T_c superconductor, *Phys. Stat. Sol.* **208**: 284–299.
- Kuntscher, C. A., Schuppler, S., Haas, P., Gorshunov, B., Dressel, M., Grioni, M., Lichtenberg, F., Herrnberger, A., Mayr, F. and Mannhart, J. (2002). Extremely small energy gap in the quasi-one-dimensional conducting chain compound $\text{SrNbO}_{3.41}$, *Phys. Rev. Lett.* **89**: 236403.
- Kuntscher, C., Schuppler, S., Haas, P., Gorshunov, B., Dressel, M., Grioni, M. and Lichtenberg, F. (2004). Electronic and vibrational properties of the low-dimensional perovskites $\text{Sr}_{1-y}\text{La}_y\text{NbO}_{3.5-x}$, *Phys. Rev. B* **70**(24): 245123.
- Kuntscher, C., van der Marel, D., Dressel, M., Lichtenberg, F. and Mannhart, J. (2003). Signatures of polaronic excitations in quasi-one-dimensional $\text{LaTiO}_{3.41}$, *Phys. Rev. B* **67**(3): 035105.
- Laverock, J., Haynes, T. D., Utfeld, C. and Dugdale, S. B. (2009). Electronic structure of RNiC_2 ($R = \text{Sm}$, Gd , and Nd) intermetallic compounds, *Phys. Rev. B* **80**: 125111.

- Levin, I. and Bendersky, L. (1999). Symmetry classification of the layered perovskite-derived $A_nB_nX_{3n+2}$ structures, *Acta Cryst. B* **55**: 853–866.
- Levin, I., Bendersky, L., Vanderah, T., Roth, R. and Stafsudd, O. (1998). A series of incommensurately modulated $A_nB_nO_{3n+2}$ phases in the $SrTiO_3$ - $Sr_2Nb_2O_7$ quasibinary system, *M. Mat. Res. Bull.* **33**(3): 501–517.
- Li, L. (2010). *Modulation of Incommensurately Modulated Structures Studied by the Maximum Entropy Method*, PHD-Thesis, Universität Bayreuth.
- Lichtenberg, F., Herrnberger, A. and Wiedenmann, K. (2008). Synthesis, structural, magnetic and transport properties of layered perovskite-related titanates, niobates and tantalates of the type $A_nB_nO_{3n+2}$, $A'A_{k-1}B_kO_{3k+1}$ and $A_mB_{m-1}O_{3m}$, *Progr. Solid State Chem.* **36**: 253–387.
- Lichtenberg, F., Herrnberger, A., Wiedenmann, K. and Mannhart, J. (2001). Synthesis of perovskite-related layered $A_nB_nO_{3n+2} = ABO_x$ type niobates and titanates and study of their structural, electric and magnetic properties, *Progr. Solid State Chem.* **29**: 1–70.
- Loa, I., Syassen, K., Wang, X., Lichtenberg, F., Hanfland, M. and Kuntscher, C. A. (2004). Crystal structure of $LaTiO_{3.41}$ under pressure, *Phys. Rev. B* **69**: 224105.
- Lovesey, S. and Collins, S. (1996). *X-Ray Scattering and Absorption by Magnetic Materials*, Oxford Series on Synchrotron Radiation, Clarendon Press.
- Manan, A., Iqbal, Y. and Qazi, I. (2011). Phase, microstructural characterization and dielectric properties of Ca-substituted $Sr_5Nb_4TiO_{17}$ ceramics, *J. Mater. Sci.* **46**: 3415–3423.
- Matsuo, S., Onodera, H., Kosaka, M., Kobayashi, H., Ohashi, M., Yamauchi, H. and Yamaguchi, Y. (1996). Antiferromagnetism of $GdCoC_2$ and $GdNiC_2$ intermetallics studied by magnetization measurement and ^{155}Gd mössbauer spectroscopy, *J. Magn. Magn. Mater.* **161**(0): 255 – 264.
- Mills, D. M. (2002). *Third generation hard x-ray synchrotron radiation sources*, John Wiley and Sons, New York.
- Murase, M., Tobo, A., Onodera, H., Hirano, Y., Hosaka, T., Shimomura, S. and Wakabayashi, N. (2004). Lattice constants, electrical resistivity and specific heat of $RNiC_2$, *J. Phys. Soc. Jpn.* **73**: 2790–2794.

- Murray, R. and Evans, B. L. (1979). The thermal expansion of 2H-MoS₂ and 2H-WSe₂ between 10 and 320 K, *J. Appl. Crystallogr.* **12**: 312–315.
- Nanamatsu, S. and Kimura, M. (1974). Ferroelectric properties of Ca₂Nb₂O₇ single crystal, *J. Phys. Soc, Jpn.* **36**: 1495.
- Nanamatsu, S., Kimura, M., Doi, K., Matsushita, S. and Yamada, N. (1974). A new ferroelectric: La₂Ti₂O₇, *Ferroelectrics* **8**: 511–513.
- Nanamatsu, S., Kimura, M. and Kawamura, T. (1975). Crystallographic and dielectric properties of ferroelectric A₂B₂O₇ (A=Sr, B=Ta, Nb) crystals and their solid solutions, *J. Phys. Soc, Jpn.* **38**: 817–824.
- Nanot, M., Queyroux, F. and Gilles, J. (1979). Crystallographic study on the terms n=4,5 and 6 of the series (La,Ca)_nTi_nO_{3n+2}, (Nd,Ca)_nTi_nO_{3n+2} and Ca_n(Ti,Nb)_nO_{3n+2}, *J. Solid State Chem.* **28**: 137–147.
- Nanot, M., Queyroux, F., Gilles, J.-C., Carpy, A. and Galy, J. (1974). Phases multiples dans les systèmes Ca₂Nb₂O₇-NaNbO₃ et La₂Ti₂O₇-CaTiO₃: Les séries homologues de formule A_nB_nO_{3n+2}, *J. Solid State Chem.* **11**(4): 272 – 284.
- Nanot, M., Queyroux, F., Gilles, J. C. and Chevalier, R. (1976). Crystal-structure of Nd₄Ca₂Ti₆O₂₀, *Acta Cryst. B* **32**(APR15): 1115–1120.
- Nanot, M., Queyroux, F., Gilles, J.-C. and Portier, R. (1981). Phases A_nB_nO_{3n+2} des systèmes La₂Ti₂O₇-CaTiO₃, Nd₂Ti₂O₇-CaTiO₃ et Ca₂Nb₂O₇-CaTiO₃. ii. nouvelles caractéristiques cristallographiques et interprétation du maillage relevé par microscopie électronique, *J. Solid State Chem.* **38**(1): 74 – 81.
- Nanot, M., Queyroux, F., Gilles, J. and Capponi, J. (1986). Study of the incommensurability of (La₄Ca₂)Ti₆O₂₀ and (Nd₄Ca₂)Ti₆O₂₀, members n = 6 of the A_nB_nO_{3n+2} family: Interpretation of the lattice modulation using a four-dimensional space, *J. Solid State Chem.* **61**(3): 315 – 323.
- Onodera, H., Koshikawa, Y., Kosaka, M., Ohashi, M., Yamauchi, H. and Yamaguchi, Y. (1998). Magnetic properties of single-crystalline RNiC₂ compounds (R = Ce, Pr, Nd and Sm), *J. Magn. Magn. Mater.* **182**: 161–171.
- Onodera, H., Uchida, N., Ohashi, M., Yamauchi, H., Yamaguchi, Y. and Sato, N. (1994). Magnetic properties of single-crystalline TbCoC₂ and TbNiC₂ compounds, *J. Magn. Magn. Mater.* **137**: 35 – 43.

- Oxford Diffraction (2006). *CrysAlis Pro software*, Oxford Diffraction Ltd, Abingdon.
- Perez-Mato, J., Zakhour-Nakhl, M., Weill, F. and Darriet, J. (1999). Structure of composites $a_{1+x}(a'_{1-x})O_3$ related to the 2H hexagonal perovskite: relation between composition and modulation, *J. Mater. Chem.* **9**: 2795–2808.
- Petricek, V., Dusek, M. and Palatinus, L. (2006). *The crystallographic computing system JANA2006*, Institute of Physics, Praha, Czech Republic.
- Rowland, R. D., Bright, N. F. H. and Jongejan, A. (1958). Advances in X-ray analysis, *Advances in X-ray Analysis*, Vol. 2, Denver Research Institute, Denver Research Institute, Virginia, p. 97.
- Schäfer, J., Rotenberg, E., Kevan, S. D., Blaha, P., Claessen, R. and Thorne, R. E. (2001). High-temperature symmetry breaking in the electronic band structure of the quasi-one-dimensional solid NbSe₃, *Phys. Rev. Lett.* **87**: 196403.
- Scheunemann, K. and Müller-Buschbaum, H. (1975). Crystal-structure of Nd₂Ti₂O₇, *J. Inorg. Nucl. Chem.* **37**(11): 2261–2263.
- Schmalle, H., Williams, T., Reller, A. and Linden, A. nad Bednorz, J. (1993). The twin structure of La₂Ti₂O₇ - X-ray and transmission electron-microscopy studies, *Acta Cryst. B* **49**(Part 2): 235–244.
- Schönleber, A., Angelkort, J., van Smaalen, S., Palatinus, L., Senyshyn, A. and Morgenroth, W. (2009). Phase transition, crystal structure, and magnetic order in VOCl, *Phys. Rev. B* **80**(6): 064426.
- Schreurs, A. M. M., Xian, X. and Kroon-Batenburg, L. M. J. (2010). Eval15: a diffraction data integration method based on ab initio predicted profiles, *J. Appl. Crystallogr.* **43**: 70–82.
- Sebastian, M. T. and Jantunen, H. (2008). Low loss dielectric materials for LTCC applications: a review, *Int. Mater. Rev.* **53**: 57–90.
- Semenenko, K. N., Putyatin, A. A. Nikolskaya, I. V. and Burnasheva, V. V. (1983). Synthesis of RNIC₂ (R = ree) compounds at high-pressures and temperatures, *Russ. J. Inorg. Chem.* **28**: 1673–1676.
- Shannon, R. D. (1976). Revised effective ionic-radii and systematic studies of interatomic distances in halides and chalcogenides, *Acta Crystallogr. A* **32**: 751–767.

- Sheldrick, G. M. (2008). *SADABS, Version 2008/1*, University of Göttingen, Göttingen, Germany.
- Shelton, R. N., Hausermann-Berg, L. S., Klavins, P., Yang, H. D., Anderson, M. S. and Swenson, C. A. (1986). Electronic phase-transition and partially gapped fermi-surface in superconducting $\text{Lu}_5\text{Ir}_4\text{Si}_{10}$, *Phys. Rev. B* **34**: 4590–4594.
- Shimomura, S., Hayashi, C., Asaka, G., Wakabayashi, N., Mizumaki, M. and Onodera, H. (2009). Charge-density-wave destruction and ferromagnetic order in SmNiC_2 , *Phys. Rev. Lett.* **102**: 076404.
- Stokes, H. T., Campbell, B. J. and van Smaalen, S. (2011). Generation of $(3 + d)$ -dimensional superspace groups for describing the symmetry of modulated crystalline structures, *Acta Crystallogr. A* **67**(1): 45–55.
- Subedi, A. and Singh, D. J. (2009). Electron-phonon superconductivity in noncentrosymmetric LaNiC_2 : First-principles calculations, *Phys. Rev. B* **80**: 092506.
- Titov, Y. A., Belyavina, N. M., Markiv, V. Y., Slobodyanik, M. S. and Chumak, V. V. (2005b). Crystal structure of $\text{Ca}_5\text{TiNb}_4\text{O}_{17}$, *J. Alloys Compounds* **387**: 82–85.
- Titov, Y. A., Belyavina, N. M., Markiv, V. Y., Slobodyanik, M. S., Chumak, V. V. and Yaschuk, V. P. (2005a). Crystal structure of $\text{Ln}_5\text{Ti}_4\text{FeO}_{17}$ (Ln - La, Pr, Nd), *Rep. Natl. Akad. Sci. Ukraine* **12**: 149.
- van Smaalen, S. (2007). *Incommensurate Crystallography*, International Union of Crystallography Monographs on Crystallography, Oxford University Press, Oxford.
- Wendschuh-Josties, M. and Wulf, R. (1989). A measuring procedure for single-crystal diffraction using synchrotron radiation, *J. Appl. Crystallogr.* **22**(Part 4): 382–383.
- Willmott, P. (2011). *An introduction to synchrotron radiation*, John Wiley and Sons, New York.
- Wölfel, A., Lichtenberg, F. and van Smaalen, S. (2012). Two-dimensional magnetic clusters in $\text{La}_n\text{Ti}_{1-x}\text{Fe}_x\text{O}_{3n+2}$ ($n = 5$ with $x = 0.2$ and $n = 6$ with $x = 0.33$), submitted to *J. Phys. Condens. Matter*.

- Yakinthos, J. K., Kotsanidis, P. A., Schäfer, W., Kockelmann, W., Will, G. and Reimers, W. (1994). The 2-component noncollinear antiferromagnetic structures of DyNiC_2 and HoNiC_2 , *J. Magn. Magn. Mater.* **136**(3): 327–334.
- Yakinthos, J. K., Kotsanidis, P. A., Schäfer, W. and Will, G. (1990). Magnetic-structure determination of NdNiC_2 and TmNiC_2 by neutron-diffraction, *J. Magn. Magn. Mater.* **89**: 299–303.
- Yakinthos, J. K., Kotsanidis, P. A., Schäfer, W. and Will, G. (1991). The antiferromagnetic structure of ErNiC_2 ternary carbide, *J. Magn. Magn. Mater.* **102**(1-2): 71–73.
- Ziff, R. M. (1992). Spanning probability in 2d percolation, *Phys. Rev. Lett.* **69**: 2670–2673.
- Zuniga, F. J. and Darriet, J. (2003). $\text{NaCa}_4\text{Nb}_5\text{O}_{17}$: a layered perovskite $A_nB_n\text{O}_{3n+2}$ compound, *Acta. Cryst. C* **59**(2): i18–i20.

Publications

Parts of this thesis have been published or have been submitted for publication:

Chapter 6 has been published as:

Wölfel, A., Li, L., Shimomura, S., Onodera, H. and van Smaalen, S.:
Commensurate charge-density wave with frustrated interchain coupling in SmNiC_2
published in: *Phys. Rev. B*, **82**: 054120 (2010)

Chapter 7 has been submitted for publication:

Wölfel, A., Dorscht, P., Lichtenberg, F. and van Smaalen, S.:
Anisotropic thermal expansion of $\text{La}_n(\text{Ti,Fe})_n\text{O}_{3n+2}$ ($n = 5$ and $n = 6$)
submitted to: *Acta Crystallogr. B*

Chapter 8 has been published as:

Wölfel, A., Lichtenberg, F. and van Smaalen, S.:
Two-dimensional magnetic clusters in $\text{La}_n(\text{Ti}_{1-x}\text{Fe}_x)_n\text{O}_{3n+2}$ ($n = 5$ with $x = 0.2$
and $n = 6$ with $x = 0.33$)
published in: *J. Phys. : Condens. Matter*, **25**: 076003 (2013)

List of Figures

2.1	Crystal structure of the CeNiC ₂ -type	6
3.1	Schematic drawings of helium closed-cycle cryostat and crystal preparation	16
3.2	Peak profile measured without and with filters	19
3.3	Setup of the Nonius Mach3 diffractometer	26
3.4	ψ Scans for crystal shape determination	27
4.1	Idealized, non-distorted perovskite-related structures	33
5.1	Setup of the Mar345dtb Image-Plate diffractometer	38
5.2	Low temperature measurements on the Mar345dtb diffractometer	40
5.3	Program windows of VIEW	42
5.4	Program window of EVAL15	43
5.5	Setup of a Huber four-circle diffractometer	44
6.1	Crystal structure of SmNiC ₂ and one layer of Sm/Ni atoms with atomic displacements due to the modulation	49
6.2	Diffracted intensity as a function of scattering angle and crystal orientation for three reflections at 60 and 9 K	51
6.3	Schematic drawing of the variations of interatomic distances as a function of the phase of the modulation wave	54
7.1	Crystal structures of La ₅ (Ti _{0.8} Fe _{0.2}) ₅ O ₁₇ and La ₆ (Ti _{0.67} Fe _{0.33}) ₆ O ₂₀	58
7.2	Polyhedron distortions of (Ti,Fe)O ₆ octahedra as a function of t in La ₅ (Ti _{0.8} Fe _{0.2}) ₅ O ₁₇ and La ₆ (Ti _{0.67} Fe _{0.33}) ₆ O ₂₀	66
7.3	Occupancy of (Ti,Fe) sites by Fe ³⁺ as a function of t in La ₅ (Ti _{0.8} Fe _{0.2}) ₅ O ₁₇ and La ₆ (Ti _{0.67} Fe _{0.33}) ₆ O ₂₀	68

7.4	Atomic valences of Ti and Fe as a function of t and of the site occupancy by Fe ions in $\text{La}_5(\text{Ti}_{0.8}\text{Fe}_{0.2})_5\text{O}_{17}$ and $\text{La}_6(\text{Ti}_{0.67}\text{Fe}_{0.33})_6\text{O}_{20}$	69
7.5	Temperature dependence of the lattice parameters of $\text{La}_5(\text{Ti}_{0.8}\text{Fe}_{0.2})_5\text{O}_{17}$ and $\text{La}_6(\text{Ti}_{0.67}\text{Fe}_{0.33})_6\text{O}_{20}$	71
7.6	Tiltings of $(\text{Ti},\text{Fe})\text{O}_6$ octahedral groups at 90 K in $\text{La}_5(\text{Ti}_{0.8}\text{Fe}_{0.2})_5\text{O}_{17}$ and $\text{La}_6(\text{Ti}_{0.67}\text{Fe}_{0.33})_6\text{O}_{20}$	73
7.7	Temperature dependence of the tilting angles of $\text{La}_5(\text{Ti}_{0.8}\text{Fe}_{0.2})_5\text{O}_{17}$ and $\text{La}_6(\text{Ti}_{0.67}\text{Fe}_{0.33})_6\text{O}_{20}$	74
7.8	Temperature dependence of the thicknesses of the slabs and the inter-slab regions in $\text{La}_5(\text{Ti}_{0.8}\text{Fe}_{0.2})_5\text{O}_{17}$ and $\text{La}_6(\text{Ti}_{0.67}\text{Fe}_{0.33})_6\text{O}_{20}$	75
8.1	Monoclinic unit cells of $\text{La}_5(\text{Ti}_{0.8}\text{Fe}_{0.2})_5\text{O}_{17}$ and $\text{La}_6(\text{Ti}_{0.67}\text{Fe}_{0.33})_6\text{O}_{20}$	80
8.2	Temperature dependence of selected structural features of $\text{La}_5(\text{Ti}_{0.8}\text{Fe}_{0.2})_5\text{O}_{17}$ and $\text{La}_6(\text{Ti}_{0.67}\text{Fe}_{0.33})_6\text{O}_{20}$	82
8.3	Inverse magnetic susceptibility χ^{-1} as a function of temperature for $\text{La}_5(\text{Ti}_{0.8}\text{Fe}_{0.2})_5\text{O}_{17}$ and $\text{La}_6(\text{Ti}_{0.67}\text{Fe}_{0.33})_6\text{O}_{20}$	84
A.1	Step scans along \mathbf{b}^* for SmNiC_2	98
A.2	Comparison of intensities of main and satellite reflections	99
A.3	Step scans for the determination of the detector collimator's incidence limit	100
B.1	Fe^{3+} occupancies in $\text{La}_5(\text{Ti}_{0.80}\text{Fe}_{0.20})_5\text{O}_{17}$ in the temperature range 90–250 K	111
B.2	Fe^{3+} occupancies in $\text{La}_5(\text{Ti}_{0.80}\text{Fe}_{0.20})_5\text{O}_{17}$ in the temperature range 295–350 K	112
B.3	Fe^{3+} occupancies in $\text{La}_6(\text{Ti}_{0.67}\text{Fe}_{0.33})_6\text{O}_{20}$ in the temperature range 90–250 K	113
B.4	Fe^{3+} occupancies in $\text{La}_6(\text{Ti}_{0.67}\text{Fe}_{0.33})_6\text{O}_{20}$ in the temperature range 295–350 K	114
B.5	Octahedra distortions in $\text{La}_5(\text{Ti}_{0.80}\text{Fe}_{0.20})_5\text{O}_{17}$ in the temperature range 90–250 K	115
B.6	Octahedra distortions in $\text{La}_5(\text{Ti}_{0.80}\text{Fe}_{0.20})_5\text{O}_{17}$ in the temperature range 295–350 K	116
B.7	Octahedra distortions in $\text{La}_6(\text{Ti}_{0.67}\text{Fe}_{0.33})_6\text{O}_{20}$ in the temperature range 90–250 K	117

B.8	Octahedra distortions in $\text{La}_6(\text{Ti}_{0.67}\text{Fe}_{0.33})_6\text{O}_{20}$ in the temperature range 295–350 K	118
B.9	(Ti,Fe)–O distances in $\text{La}_5(\text{Ti}_{0.80}\text{Fe}_{0.20})_5\text{O}_{17}$ in the temperature range 90–250 K	119
B.10	(Ti,Fe)–O distances in $\text{La}_5(\text{Ti}_{0.80}\text{Fe}_{0.20})_5\text{O}_{17}$ in the temperature range 295–350 K	120
B.11	(Ti,Fe)–O distances of $\text{La}_6(\text{Ti}_{0.67}\text{Fe}_{0.33})_6\text{O}_{20}$ in the temperature range 90–250 K	121
B.12	(Ti,Fe)–O distances of $\text{La}_6(\text{Ti}_{0.67}\text{Fe}_{0.33})_6\text{O}_{20}$ in the temperature range 295–350 K	122
B.13	Calculated valences of $\text{La}_5(\text{Ti}_{0.80}\text{Fe}_{0.20})_5\text{O}_{17}$ in the temperature range 90–250 K	123
B.14	Calculated valences of $\text{La}_5(\text{Ti}_{0.80}\text{Fe}_{0.20})_5\text{O}_{17}$ in the temperature range 90–250 K	124
B.15	Calculated valences of $\text{La}_6(\text{Ti}_{0.67}\text{Fe}_{0.33})_6\text{O}_{20}$ in the temperature range 90–250 K	125
B.16	Calculated valences of $\text{La}_6(\text{Ti}_{0.67}\text{Fe}_{0.33})_6\text{O}_{20}$ in the temperature range 295–350 K	126

List of Tables

2.1	Relative atomic coordinates and atomic displacement parameters of DyNiC ₂	6
2.2	Magnetic properties of known RNiC ₂ compounds	9
3.1	Manual measurement of attenuation factors at beamline D3	21
3.2	Automatic procedure for the measurement of attenuation factors at beamline D3	22
3.3	Shells in $\frac{\sin\theta}{\lambda}$ with the numbers of main and first order satellite reflections measured for SmNiC ₂	25
3.4	Crystal data of the room temperature structure of SmNiC ₂	29
3.5	Relative atomic coordinates and atomic displacement parameters of SmNiC ₂ at room temperature.	30
5.1	List of the angular values of the four equivalent positions of a reflection in Euler geometry	45
6.1	Structural parameters of SmNiC ₂ at $T = 60$ K	52
7.1	Crystal data of La ₅ (Ti _{0.8} Fe _{0.2}) ₅ O ₁₇ and La ₆ (Ti _{0.67} Fe _{0.33}) ₆ O ₂₀ at seven temperatures between 90 and 350 K	61
7.2	Thermal expansion coefficients in the range 90–370 K of La ₅ (Ti _{0.8} Fe _{0.2}) ₅ O ₁₇ and La ₆ (Ti _{0.67} Fe _{0.33}) ₆ O ₂₀	70
B.1	Occupancy, coordinates and isotropic ADP of La ₅ (Ti _{0.80} Fe _{0.20}) ₅ O ₁₇	102
B.2	Anisotropic ADPs of La ₅ (Ti _{0.80} Fe _{0.20}) ₅ O ₁₇	104
B.3	Occupancy, coordinates and isotropic ADP of La ₆ (Ti _{0.67} Fe _{0.33}) ₆ O ₂₀	105
B.4	Anisotropic ADPs of La ₆ (Ti _{0.67} Fe _{0.33}) ₆ O ₂₀	108

Erklärung

Ich versichere hiermit eidesstattlich, dass ich diese Dissertation selbstständig und nur unter Verwendung angegebener Quellen und zulässiger Hilfsmittel erstellt habe. Ich habe bisher keine Promotionsversuche unternommen. Ich habe bisher weder die Hilfe von gewerblichen Promotionsberatern bzw. -vermittlern in Anspruch genommen, noch werde ich sie künftig in Anspruch nehmen.

Alexander Wölfel

Bayreuth, den 31.01.2013